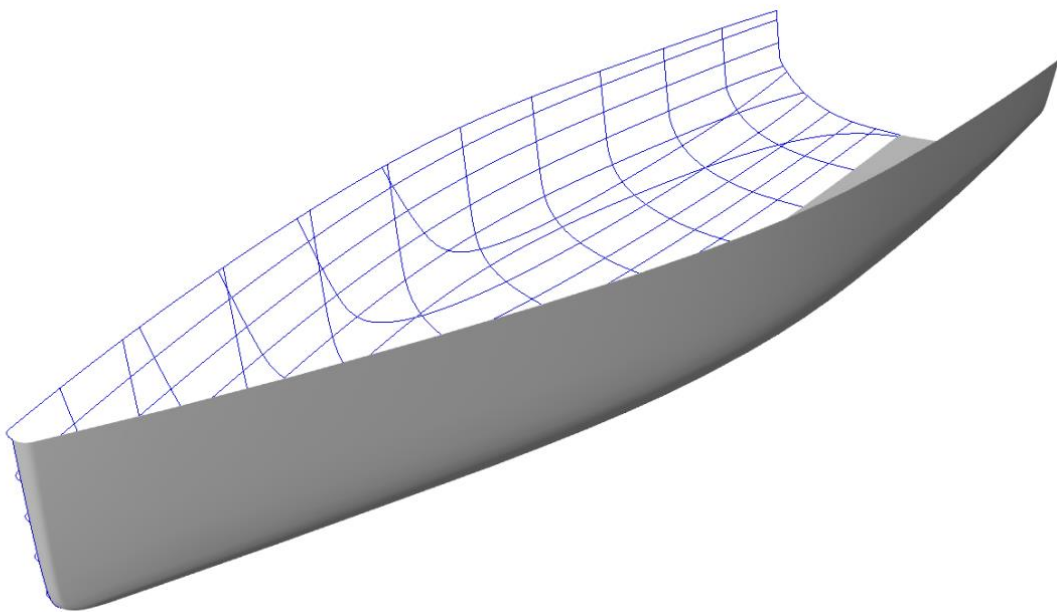


CHALMERS



A CFD Investigation of Sailing Yacht Transom Sterns

*Master's Thesis in the International Master's Programme Naval Architecture and
Ocean Engineering*

JENS ALLROTH & TING-HUA WU

Department of Shipping and Marine Technology
Division of Marine Design, Research Group Hydrodynamics
CHALMERS UNIVERSITY OF TECHNOLOGY
Göteborg, Sweden 2013
Master's thesis 2013: X-13/296

MASTER'S THESIS IN THE INTERNATIONAL MASTER'S PROGRAMME IN
NAVAL ARCHITECTURE AND OCEAN ENGINEERING

A CFD Investigation of Sailing Yacht Transom Sterns

JENS ALLROTH & TING-HUA WU

Department of Shipping and Marine Technology
Division of Marine Design
Research Group Hydrodynamics
CHALMERS UNIVERSITY OF TECHNOLOGY
Göteborg, Sweden 2013

A CFD Investigation of Sailing Yacht Transom Sterns

JENS ALLROTH & TING-HUA WU

© JENS ALLROTH & TING-HUA WU, 2013

Master's Thesis 2013: X-13/296

ISSN 1652-8557

Department of Shipping and Marine Technology

Division of Marine Design

Research Group Hydrodynamics

Chalmers University of Technology

SE-412 96 Göteborg

Sweden

Telephone: + 46 (0)31-772 1000

Cover:

Rendering of the New Design 41-40r.

Chalmers Reproservice/ Department of Shipping and Marine Technology
Göteborg, Sweden 2013

A CFD Investigation of Sailing Yacht Transom Sterns
Master's Thesis in the International Master's Programme in Naval Architecture and
Ocean Engineering
JENS ALLROTH & TING-HUA WU
Department of Shipping and Marine Technology
Division of Marine Design
Research Group Hydrodynamics
Chalmers University of Technology

Abstract

The objective of this thesis was to investigate whether the hydrodynamic performance of the wide, box-shaped transoms that have become very popular on modern performance cruisers is better than the performance of the more conventional, less wide, rounder transoms.

The investigation of the hydrodynamic performance was evaluated with the aid of computational fluid dynamics using the Reynolds Average Navier-Stokes (RANS) viscous solver SHIPFLOW 5.0 with Volume of Fluids method surface capturing (VOF). First part of the study was to conduct verification of the software using the Least Square Root method. Second part was to make a validation of the software where Computational Fluid Dynamics (CFD) results were compared to experimental data from towing tank tests of Delft Systematic Yacht Hull Series (DSYHS) hulls. In the third part an average modern performance cruiser was designed to later be used as a base line for a systematic transom geometry variation study. Twelve hulls were created with varying transom size and shape. Each hull was tested in four conditions; upright and heeled condition at Froude numbers 0.35 and 0.60. Finally the results from the CFD computations were used to set up a simple upwind-downwind race to distinguish which hull that had the best overall performance.

In the upwind-downwind race the round transoms performed best for the three fastest transom sizes. The fastest hull around the course has an immersed transom ratio (A_t/A_x) of 0.16 and it is 1.9 % faster with round transom than with boxy.

The study has led to better understanding of the relation between hydrostatic and hydrodynamic resistance at high Froude numbers where the gain from a big immersed transom area is larger than the loss from increased transom resistance. Also, the influence on wave resistance from the curvature of the water and buttock lines has been clearly illustrated. For low Froude numbers, where the transom is wetted, the effect from viscous pressure resistance, base drag, has been pinpointed.

Key words: Sailing, Yacht Design, Transom, CFD, V&V, LSR method, Optimization, RANS, VOF

Contents

ABSTRACT	I
CONTENTS	II
PREFACE	V
NOTATIONS	VI
1 INTRODUCTION	1
1.1 Background	1
1.2 Objective of the investigation	2
1.3 Methodology	2
1.4 Limitations	3
2 THEORY	4
2.1 The resistance of a hull	4
2.1.1 Viscous resistance	5
2.1.2 Wave resistance	6
2.2 Possible advantages and disadvantages with the box shaped transom	8
2.3 Computational Fluid Dynamics	11
2.3.1 Verification and Validation	11
2.3.2 Governing Equations	15
2.3.3 Free surface capturing - Volume of Fluids (VOF) method	16
2.3.4 SHIPFLOW 5.0	16
3 METHOD	17
3.1 Pre-study of the Delft hull series	17
3.2 Verification	18
3.3 Validation	22
3.4 Optimization	23
3.4.1 Creation of the ND41	23
3.4.2 Hull geometry variations	25
3.4.3 CFD investigations of optimum transom stern	28
4 RESULTS AND DISCUSSION	30
4.1 Verification	30
4.1.1 Upright condition	30
4.1.2 Heeled condition	31
4.1.3 Discussion	33
4.2 Validation	34

4.2.1	Upright condition	34
4.2.2	Heeled condition	37
4.2.3	Discussion	39
4.3	Optimization	41
4.3.1	Upright at Froude number 0.35	43
4.3.2	Upright at Froude number 0.60	48
4.3.3	Heeled 20° at Froude number 0.35	53
4.3.4	Heeled 20° at Froude number 0.60	59
4.3.5	Upwind-Downwind race	65
4.3.6	The waterline effect on the wave creation	66
4.3.7	The rocker curve effect on the hydrodynamic pressure resistance	68
4	SUMMARY	71
5	FUTURE WORK	73
6	REFERENCES	74
APPENDIX I - VERIFICATION		I
I.1	Upright condition	i
I.2	Heeled condition	ii
APPENDIX II – VALIDATION		III
II.1	Hydrostatics Sysser hulls	iii
II.2	Sysser 46 upright measurement data	iii
II.3	Sysser 47 upright measurement data	iv
II.4	Sysser 50 upright measurement data	iv
II.5	Sysser 47 heeled measurement data	v
II.6	Sysser 48 heeled measurement data	v
APPENDIX III - OPTIMIZATION		VI
III.1	Upright, $F_n = 0.35$	vi
III.2	Upright, $F_n = 0.60$	viii
APPENDIX IV – SHIPFLOW CONFIGURATION FILES		X
IV.1	XPAN	x
IV.1.1	Upright	x
IV.1.2	Heeled	x
IV.2	XCHAP	xi
IV.2.1	Upright	xi
IV.2.2	Heeled	xi

Preface

This thesis is a part of the requirements for the master's degree in Naval Architecture and Ocean Engineering at Chalmers University of Technology, Göteborg, and has been carried out at the Division of Marine Design, Department of Shipping and Marine Technology, Chalmers University of Technology between January and June of 2013.

We would like to acknowledge and thank our examiner, Full Professor Lars Larsson, and our supervisor, PhD student Michal Orych, at the Department of Shipping and Marine Technology, for their excellent, enthusiastic, guidance and support throughout the work with this thesis. Despite being two very busy men, they always had a moment to spare when we needed their attention.

Göteborg, June 2013

Jens Allroth & Ting-Hua Wu

Notations

Roman upper case letters

AP	After perpendicular
A_t	Immersed transom area
A_{tr}	Area of submerged part of transom
A_x	Maximum area section
CAD	Computer aided design
CFD	Computational fluid dynamics
Cb	Block coefficient
C_f	Frictional resistance coefficient
Cp	Prismatic area coefficient
C_p	Pressure resistance coefficient
C_t	Total resistance coefficient
C_{tr}	Transom pressure resistance coefficient
C_w	Wave resistance coefficient
D	Experimental data
DSYHS	Delft systematic yacht hull series
E	Validation comparison error
F_i	Force
Fn	Froude number
F_S	Factor of safety for numerical uncertainty
Fx_f	Frictional force in x-direction
Fx_p	Pressure force in x-direction
ITTC	International Towing Tank Conference
L	Length of hull
Lcb	Longitudinal centre of buoyancy
Lcf	Longitudinal centre of flotation
LOA	Length over all
L_{WL}	Length of water line
LSR	Least Square Root method
P	Ratio between the observed and theoretical order of accuracy
RANS	Reynolds Average Navier-Stokes
RE	Richardson Extrapolation
Re	Reynolds number

R_{ji}	Reynolds stress
R_t	Total resistance
R_w	Wave resistance
S	Numerical estimated solution
S	Wetted surface
S_0	Estimated exact solution
S_1	Numerical solution of the finest grid
S_i	Numerical solution of i^{th} grid
SST	Shear stress transport
Std	Standard deviation
Sw	Wetted surface
TCB	Transversal centre of buoyancy
T_v	True value
U_I	Iterative uncertainty
U_G	Grid discretization uncertainty
U_{SD}	Standard deviation
U_{SD}^{02}	Standard deviation
U_{SD}^{12}	Standard deviation
U_{SN}	Numerical uncertainty
U_{val}	Validation uncertainty
V	Velocity
VOF	Volume of fluid method

Roman lower case letters

g	Gravity
h_1	Step size of the finest grid
h_i	Step size of i^{th} grid
h_{ng}	Step size of the n_g^{th} grid
n_{ch}	Number of triplets
n_g	Number of grid
p	Order of accuracy for Richardson Extrapolation
p_{th}	Theoretical order of accuracy for Richardson Extrapolation
u_i	Flow velocity
\bar{z}_{tr}	Z-coordinate of centroid of submerged part of transom

Greek upper case letters

Δh_d	Reduced hydrodynamic resistance
Δh_s	Increased hydrostatic resistance
ΔM	Data range

Greek lower case letters

α	A constant for estimating the grid discretization error
α_{11}	A constant for estimating the grid discretization error
α_{12}	A constant for estimating the grid discretization error
δ_D	Error in the experimental data
δ_{input}	Input parameter error
δ_{model}	Modelling error
δ_{num}	Numerical error
δ_{RE}	Grid discretization error
δ_{RE}^{02}	Grid discretization error
δ_S	Error in the numerical solution
$\delta_{\Delta M}$	Grid discretization error
ε_{RE}	Discretization error
λ	Wavelength
μ	Dynamic viscosity
μ_T	Turbulent dynamic viscosity
ν	Kinematic viscosity, μ/ρ
ν_T	Turbulent kinematic viscosity, μ_T/ρ
ν_E	Total kinematic viscosity, $\nu + \nu_T$
ρ	Density
σ_{ji}	Viscous stress

1 Introduction

1.1 Background

Since human learnt how to build boats, there has been an interest in having the fastest vessel. In the early days the incentive might have been to escape your enemies, or to arrive first to the dock and sell your cargo at the best price. In those days sails were the best option to propel the ships. Today, there are other more practical ways to power the commercial vessels. However, to many sailors, sailing is still about getting from point A to B as fast as possible. There are, of course, many ways to achieve this, but one very crucial factor is that the tool, the sailing yacht, is in fact designed and optimized for the conditions it is being used at. The problem, which is also the charm, is that the conditions are constantly changing at sea. Thus, finding one optimum design for all conditions is impossible. That has not kept designers away from trying to, though.

There are numerous parameters to keep in mind and account for in the design process. The first, a very basic parameter, is the environment in which the boat is intended to be used. A boat sailing in the Bay of Biscay is very likely to encounter more rough weather than one sailing in the Swedish archipelago and different attributes might be desired. The purpose of the sailing yacht will definitely impact the design. A pure racing yacht will not be very well suited for a family going out for the club races and their boat certainly will not be attractive to the hard core racer.

The development of modern lightweight materials and building techniques have allowed designers to move the limits of what is possible to achieve with wind being the only power source. Lighter, stronger and stiffer materials allow for more powerful boats today than when wood practically was the only option when it came to hull and rig construction materials.

Development of the design rules under which the yachts must comply when competing in yacht races has influenced the appearance of performance yachts. Numerous different rules have passed over the centuries, some more influential than others, and they have usually affected not only the top end racing yachts but also the segment of more performance oriented cruising yachts, often called performance cruisers.

These are some of the parameters that have contributed to the development of the looks of what has been considered a modern sailing yacht over the years. On top of them, there is usually a rather large component of aesthetics and fashion.

Today one can see a trend of convergence in design amongst the producers of performance cruisers around the world. Over the last thirty years or so the designers has moved from round hull lines and narrow transoms, towards straighter hull lines and very wide, box-shaped transoms.

The hull shape evolution can, to some extent, be coupled with the development of the racing rules. But that is the only factor of the ones mentioned above that has really changed a lot during the same time span. These performance cruisers still have hulls built with glass fibre reinforced polyester and rigs with aluminium mast and stainless steel rigging. The building techniques have of course improved, but looking at the sail area to weight ratio (Figure 1.1.1), the improvement is marginal.

For high-end race yachts the development is different. Here, new materials such as aramid fibre, and today carbon fibre reinforced epoxy and titanium has made its entry into both hull and rig construction. So has new advanced manufacturing techniques, and the result is a significantly improved product. This is also where the development of the modern hull lines now seen on performance cruisers has its origin.

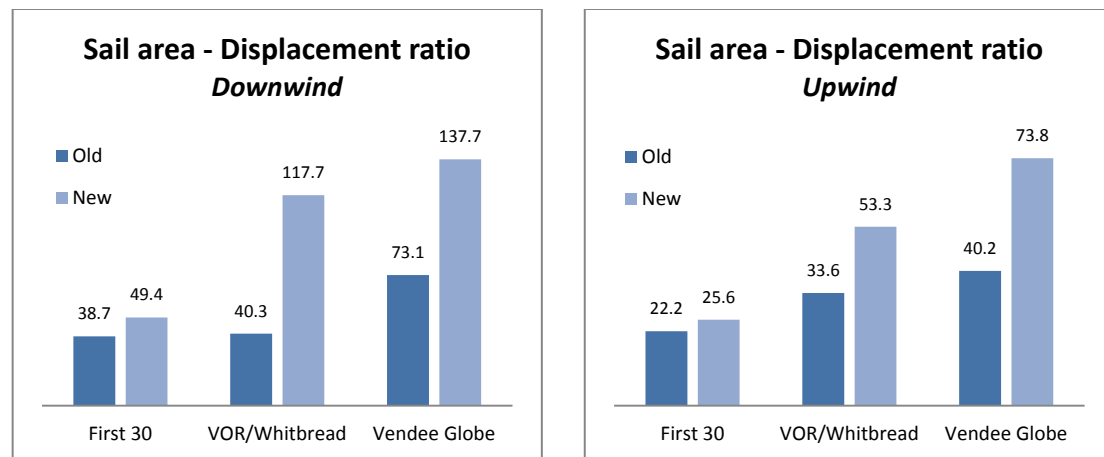


Figure 1.1.1. Graphs showing the development in sail area to displacement ratio $\left[\frac{\text{Sail area}}{\text{Displacement}^{\frac{2}{3}}} \right]$, upwind and downwind, comparing sailing yachts of the late 1980's with the most modern ones. The trend towards more powerful boats is not very significant for the performance cruiser, when compared to the racing yachts.

1.2 Objective of the investigation

The question studied in this thesis is whether the modern hull lines with wide, box-shaped transoms that seem to origin from extreme racing machines also are beneficial for modern performance cruisers, from a hydrodynamic performance point of view. Parameters that primarily are considered and evaluated are total, frictional and pressure resistance, longitudinal center of buoyancy, prismatic coefficient, and transom size, shape and immersion.

1.3 Methodology

The methodology in the thesis consists of three phases, plus a pre-study. The CFD software used in the study is SHIPFLOW 5.0 which is a Reynolds averaged Navier-Stokes (RANS) SST $k-\omega$ solver with (Volume of Fluid) VOF treatment of the free surface for incompressible flows at steady state.

In the pre-study other similar investigations are studied. Deeper knowledge is gained in the field of viscous and potential flow CFD software. Methods for verification and validation of computational hydrodynamics are learnt and evaluated.

The first phase after the pre-study is the verification. This is done to estimate the numerical error or uncertainty in the iteration and discretization process of the CFD computations. A hull from the Delft Systematic Yacht Hull Series (DSYHS) is used in two conditions, one high Froude number upright and one low Froude number heeled,

and different grid configurations and densities are investigated. In this study the Least Square Root method is used for verification.

The second phase is the validation which is a process of determining the degree to which the calculation model is an accurate representation of the real world. The configuration that has been found to work satisfactory in the verification phase is used when numerous calculations are run and the results are validated against experimental data. In this study, data from towing tank tests of DSYHS hulls are compared with the calculated resistance of the same hulls. For the upright condition, validation is performed for five hulls at Froude numbers ranging from 0.25 to 0.70. For the heeled condition, validation is performed on two hulls at Froude numbers ranging from 0.25 to 0.45.

The last phase in the study is the optimization. A new hull is designed which is intended to be an average of modern performance cruisers in the same size range. This hull, called ND41, is the basis for a transom geometry variation study. Seven different box shaped transom sizes are tested in upright condition. Later, four of those are altered in two steps towards a more round shaped transom resulting in a total of twelve hulls with varying transom sizes and shapes. These twelve hulls are run at Froude numbers 0.35 and 0.6 in both upright and 20° heeled condition.

From the results, tendencies can be shown regarding optimum transom size and shape, longitudinal center of buoyancy, prismatic coefficient, and transom immersion.

Finally, a simple upwind-downwind race case is set up to evaluate which transom geometry that would be the most beneficial around a race course.

1.4 Limitations

The main limitation of this study is the time, which is limited to 20 weeks, in combination with the limited amount of computer power. Therefore the number of cases that can be run is rather limited. Each hull is tested in four conditions; one upright case and one heeled, and both cases are run at two different speeds. A total of 18 hull variations are used. Further, the added resistance from encountering waves is not investigated. Nor is any leeway angle applied in the CFD computations, and no appendages are accounted for.

The accuracy of the computations is limited by the number of cells in the domain of the fluid calculations, and that in turn is again limited by available computer power.

The validation cannot be done to its full extent since the uncertainty of the input data from the towing tank experiments on the DSYHS hulls is not known.

The ND 41 that is designed as a baseline hull for the optimization is intended to be an average of similar performance cruisers on the market. This is by nature very hard to achieve, and it is also doubtful how trustworthy the data and line plans used in the design process from each respective yacht is. For example, no cross sections have been found from any of the designs used for input. The effects of the transom variations, however, should be reliable.

In the results, discussion and conclusion parts only hydrodynamic aspects are taken into account. Variables such as righting moment, trim and balance are thus not considered.

2 Theory

2.1 The resistance of a hull

The flow around a hull moving through the water is a rather complex process with many different components interacting (see Figure 2.1.1). How much the different components contribute depends on many different factors such as sea state, hull geometry and velocity. To be able to comprehend the content of this study some basic knowledge about the resistance components and the different flow regions around the hull is a prerequisite.

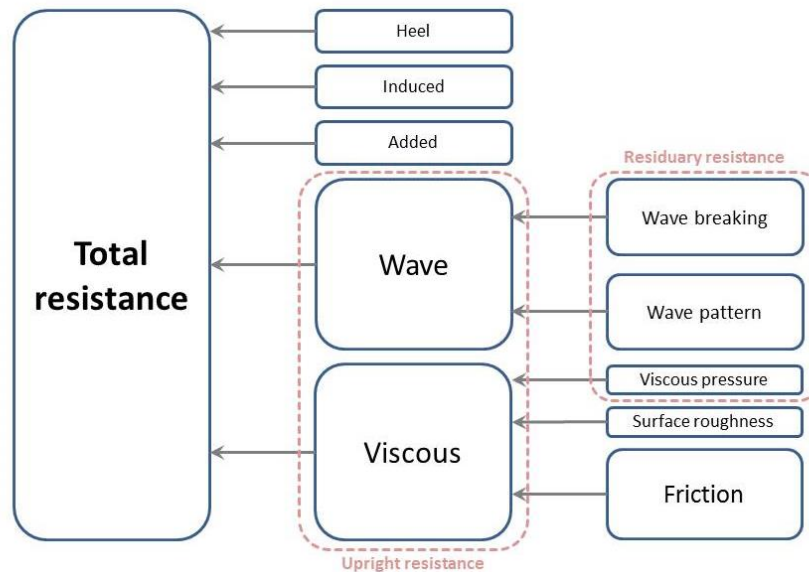


Figure 2.1.1. Schematic picture of the different resistance components contributing to the total resistance of a sailing yacht.

Starting off very basic, the resistance of an upright hull in calm water can be divided into wave resistance and viscous resistance. The wave resistance is created because of the pressure differences that occur along the hull surface as it moves through the water, cause waves containing energy to be transmitted away from the hull. The viscous resistance is caused by friction between the hull surface and the water. This friction creates small eddies which grow larger while moving downstream along the hull surface. These eddies contains energy which is left behind in the wake of the yacht.

Now, if the yacht was to be sailing upwind, with an angle of heel and encountering waves created by the wind, there would be three more components to take into account.

The first one has its origin in the waves encountered which increases the upright condition resistance components due to the unsteady movement of the yacht. This first component is therefore called added resistance.

Secondly, the heel angle of the yacht causes the flow to encounter a hull geometry that is different from the one in the upright condition. Usually the resistance is increased due to this geometry change and an addition to the total resistance due to heel must be made.

The third additional component is the induced resistance. It is caused by the fact that the yacht is not moving strictly straight through the water but with a leeway angle creating a high pressure region on the leeward side and a low pressure region on the windward side of the keel, rudder and hull. When water flows from the high pressure to the low pressure sides, vortices containing energy are left behind in the wake which adds to the total resistance of the yacht.

2.1.1 Viscous resistance

Viscous resistance can be further divided into three sub components. To understand those better one must be introduced to the different flow regions (Figure 2.1.2) around a hull.

At the hull surface, the molecular forces between the hull and water cause the water particles to have virtually no speed relative to the hull surface, usually called the no-slip condition. One layer further out from the surface the speed is non-zero, and the further away from the hull surface, the closer the flow velocity will get to the yacht's speed through the water. Close to the bow, the flow will remain smooth and without disturbances. This type of flow is called laminar. At a distance from the bow disturbances occur in the laminar flow, fluctuations and small eddies will form, and a transition take place. The flow turns from laminar to more chaotic and a turbulent boundary layer is formed with a mix of small and larger eddies. The boundary layer in the bow is very thin, but grows thicker downstream and for a 40 feet yacht the boundary layer near the stern is in the range of 0.1 m, Larsson & Eliasson (2000). Inside the turbulent boundary layer, next to the hull surface, a very thin sublayer is present. It is in the range of 0.1 mm thickness and is mainly laminar even if short bursts of fluctuations can occur here as well. If the stern of the yacht is blunt and the flow experiences relatively rapid pressure changes, separation can occur. In this case large eddies, much larger than the ones in the turbulent boundary layer, are formed and leave a large wake behind the yacht.

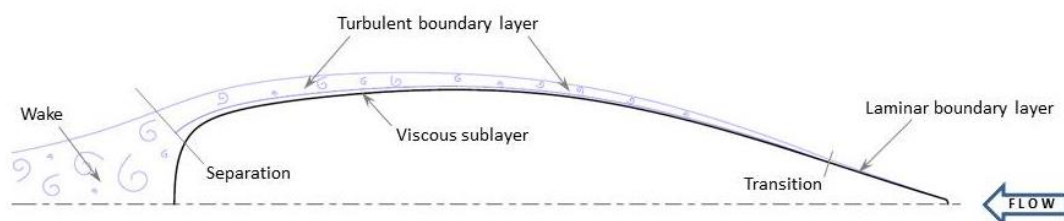


Figure 2.1.2. The different flow regions that occurs around a sailing yacht hull. Note that the thickness of the boundary layers is much exaggerated.

Now, let us look at the viscous resistance. The biggest part of the viscous resistance is the frictional resistance that is caused by the direct friction between the hull and the water as the layers of molecules away from the hull have different velocities relative to each other. While the flow is laminar the frictional forces are dominated by intermolecular forces which are rather weak, but when the flow turns turbulent the friction increases rapidly. Thus, laminar flow is desired for a big part of the hull but it is in reality hard to achieve.

The second part of the viscous resistance is easier to reduce. This is the resistance component caused by surface roughness. The surface roughness resistance can be kept at a minimum if the roughness is less than the thickness of the viscous sublayer. The thickness is governed by the velocity of the flow and how far downstream on the hull one is looking since the thickness increases downstream of the hull. If the roughness is less than the viscous sublayer thickness the surface is considered hydraulically smooth and this resistance component is negligible.

The third component of the viscous resistance is the viscous pressure resistance. As the flow encounters the bow of the yacht it will experience a pressure increase as the water particles are slowed down. Once the particles have passed the bow, they will accelerate along the hull side and thus experience lower pressure. When approaching the stern, the flow will again slow down and the pressure will increase. In an ideal case where there were no boundary layers (and no free surface), the pressure distribution would be perfectly balanced along the hull and no net force would occur. Now, in the real case, with the boundary layers present, this balance is disturbed. This is because the boundary layer, which is much thicker in the stern than in the bow, modifies the pressure distribution along the hull resulting in a pressure drop in the stern which in turn results in a net force acting in the opposite direction of the yacht's velocity. This pressure imbalance is known as the viscous pressure resistance. How large this pressure drop is depends on how thick the boundary layer is. A blunt stern causing separation will have considerably larger resistance than a more slender stern without separation. For a slender stern the viscous pressure resistance is typically in the range of 5-10% of the direct frictional resistance.

2.1.2 Wave resistance

The wave resistance is also possible to split into components of waves that break (spray) and wave pattern, but usually only the total wave resistance is considered.

Waves are created along the hull due to pressure differences caused by the hull geometry as it moves through the water. In theory waves occur at every pressure change, but for sailing yachts the ones that are considered to have significant influence on the resistance are the two waves created at the high pressure regions in the bow and stern. It is of great importance for the magnitude of the wave resistance how these two waves interact with each other and that depends on the velocity of the yacht.

The relation between traveling speed of a wave and wavelength is very simple, Larsson & Eliasson (2000);

$$\text{Wave speed} = \sqrt{\frac{g \cdot \lambda}{2\pi}} = 1.25 \cdot \sqrt{\lambda} \quad (2.1)$$

The waves created by the yacht will always travel with the same speed as the yacht and thus, the wave length will be proportional to the yacht speed squared. For example, if the yacht is traveling with a speed equal to 1.25 times the square root of the waterline length the bow and stern wave length will be the same as the waterline length. The bow wave will have one crest at the bow, a trough amidships, and a new crest at the stern. If the yacht is traveling at $1/\sqrt{2}$ the speed two wave lengths will fit along the length of the waterline, resulting in a new wave crest amidships. If the speed instead is multiplied by $\sqrt{2}$ half a wave length will fit along the waterline and the bow will be in a crest while the stern is in a constant trough. Note that this is only when looking at the bow wave, but the stern wave must also be taken into account. It will

always have a crest near the stern, and here there will be interference with the bow wave system. If the bow wave has a crest at the stern it will add to the stern wave and result in a larger wave and increased wave resistance. If instead the velocity of the yacht is such that the bow wave has a trough it will to some extent cancel the stern wave, leaving a smaller wave pattern and reduced wave resistance behind.

To be able to describe how many waves there are along the hull, a dimensionless unit called the Froude Number (F_n) is used where the velocity in meters per second is divided by the square root of the length of the waterline multiplied by gravity;

$$F_n = \frac{v}{\sqrt{g \cdot L_{WL}}} \quad (2.2)$$

The wave resistance can be plotted against the Froude number in order to see how the wave systems of a yacht interact and effects total wave resistance at different velocities (Figure 2.1.3). The exact appearance of the curve differs between different hull geometries, but in all cases there will be “humps” where the systems interact to amplify the stern wave. At low Froude numbers these humps are usually rather small, but at larger Froude numbers the humps can be very costly to overcome.

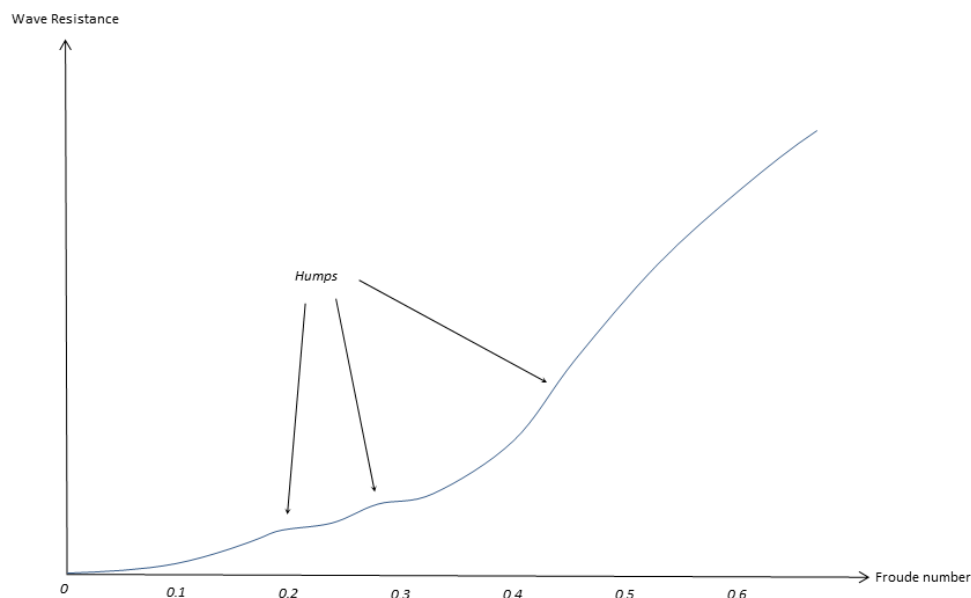


Figure 2.1.3. An example of what the wave resistance of a sailing yacht could look like for various Froude numbers. The humps are where the wave systems from the bow and stern interact to amplify the wave height.

At low Froude numbers the viscous resistance is the dominating component. It is proportional to the speed squared. The wave resistance on the other hand, which is small at low Froude numbers, increases with speed to the sixth power and is dominant at Froude numbers above approximately 0.3 (see Figure 2.1.4).

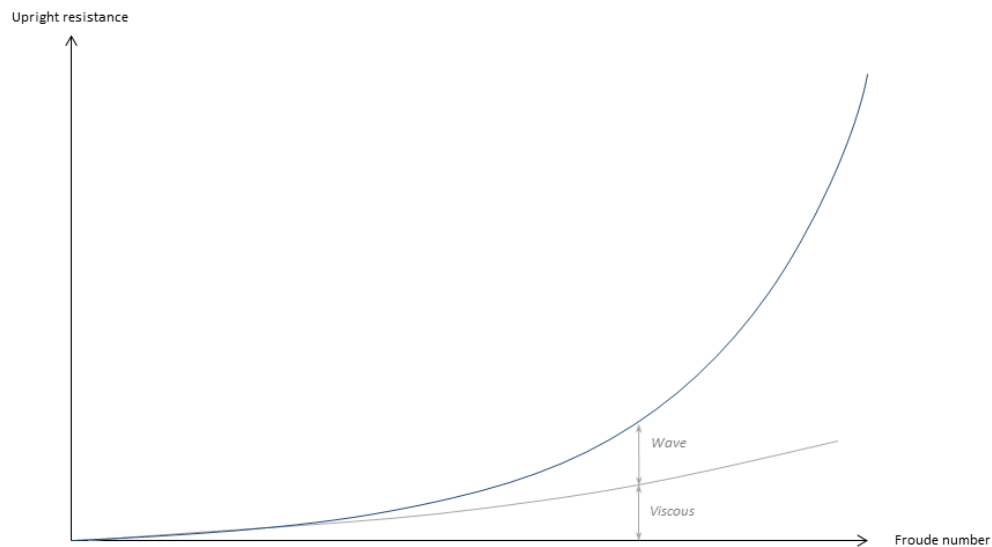


Figure 2.1.4. Principal sketch of the relation between viscous and wave resistance for an upright sailing yacht at increasing Froude number.

2.2 Possible advantages and disadvantages with the box shaped transom

In theory the box shaped transom, and the straight hull lines that comes with it, has both upsides and downsides.

The four main advantages are;

- Larger planing area at small heel angles
- Smaller wetted surface at large heel angles
- Improved righting moment when heeled
- Reduced wave resistance due to submerged transom effect at high Fn

while the main disadvantages are;

- Larger wetted surface at small heel angles
- Large transom resistance at low Froude numbers
- Balance
- Trim
- Rudder

Figure 2.2.1 shows two very different designs; one with a more conventional transom (bottom), and the other with a modern box shaped transom (top). The two pictures in the middle show the hulls in upright condition, while the pictures to the right show the hulls when they are heeled 20 degrees. The blue areas are the submerged part of the hull, at the same displacement in upright and heeled conditions.

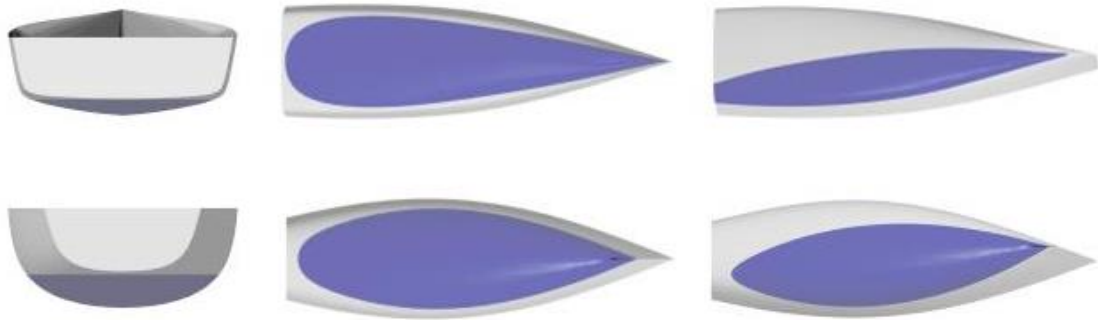


Figure 2.2.1. Designs from different eras illustrating how differently the wetted surface is distributed in upright and heeled condition.

It is easy to see how differently the submerged volume is distributed. The first three bullets of the advantages listed above can be explained by looking at the illustration above. In upright condition the flat and wide aft body of the modern hull allows for easier planing since it will produce more vertical lift when the yacht is moving forward. When heeled the sharper corner at the bilge will minimize the wetted surface to volume ratio and thus the frictional resistance can be reduced. The residual resistance, however, is harder to predict at a first glance. The advantage from better righting moment derives from the fact that the transversal centre of buoyancy (TCB) is moved further out to the side, again due to the box-like geometry. By doing this the lever arm of the buoyant force is extended which has a positive effect on the righting moment. This advantage is not taken into account in this study, nor are the effects on balance and the rudder being lifted out of the water. The change of trim at speed is accounted for, but not further described here.

The possible advantage from reduced wave resistance is not intuitively obvious. This matter can be divided into two parts. First, it depends on whether the transom of the hull is submerged or not, and secondly, if the submerged transom is wetted or cleared from water at desired speed.

There is always hydrostatic pressure acting on the hull that is caused by gravity and the density of the water. For a hull with a wetted transom that is moving through the water, the pressure forces from the water due to gravity has a total horizontal hydrostatic pressure coefficient close to zero. At a submerged transom which is not wetted (the flow leaves the bottom tangentially backwards) the pressure at the transom is only atmospheric (Figure 2.2.2). The loss of hydrostatic pressure at the transom will result in a horizontal hydrostatic pressure force pointing backwards. The transom pressure resistance coefficient, C_{tr} , can be computed by the following formula, Larsson & Raven (2010);

$$C_{tr} = -\frac{A_{tr} \bar{z}_{tr}}{S} \frac{2}{L Fn^2} \quad (2.3)$$

where A_{tr} and \bar{z}_{tr} are the area and the (negative) z-coordinate of the centroid of the submerged part of the transom. S and L are the wetted surface and the length of the hull.

At low Froude numbers, just above the critical speed where the transom is cleared from water, the transom resistance can be much larger than the resistance due to the hydrodynamic pressure. At very low Froude numbers where the transom is wetted, the

resistance increases rapidly when eddies form behind the hull as the boundary layer separates from the hull surface, this is sometimes referred to as a base drag.



Figure 2.2.2. In order for the submerged transom to be efficient, the flow must leave the hull bottom tangentially backwards such that the transom is not wetted by the stern wave.

So, what is then the upside of the submerged transom? At high speeds round buttock lines and waterlines create a low pressure region that increases the trim and sinkage which increases the wave resistance. If, instead, the buttocks are straightened they will cause the aft part of the hull to generate more vertical lift and consequently the wave resistance will decrease. Further, rounded waterlines will generate a low pressure on the sides of the aft body, which will deepen the wave trough found in this region at high speed. The stern wave system is then amplified, and the resulting wave resistance is increased. Straighter buttocks and waterlines will in practice result in a larger transom area, as is the case for newer designs. Note from equation (2.3) that transom resistance is inversely proportional to Froude number squared, and thus a large transom at high speed could be beneficial. Hydrodynamic pressure resistance, however, increases with speed and therefore a small transom is desired when speed decreases as the transom resistance is a relatively big part of the total residual resistance. The graph in Figure 2.2.3 describes this relationship, which makes the design of the aft body and transom a true balancing act.

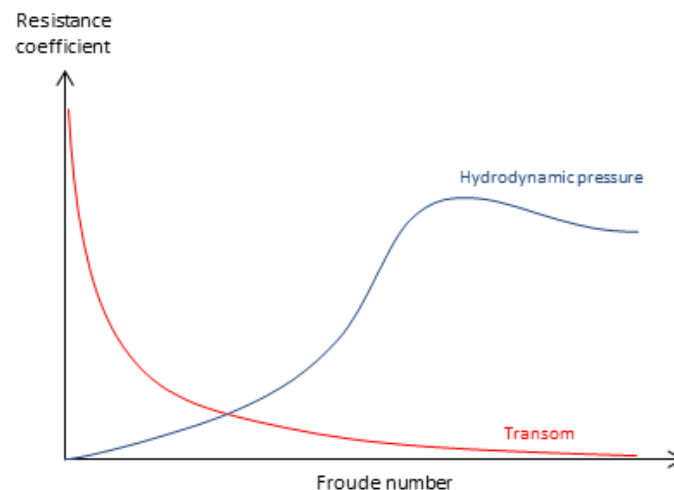


Figure 2.2.3. The relationship between hydrodynamic and transom resistance coefficients at increasing Froude number.

The theory about submerged transoms holds for both the case where a yacht is sailing upright and when it is sailed heeled. Usually a larger transom is more beneficial in upright position (going downwind), than when heeled (going upwind). This is because a larger transom usually becomes more submerged when heeled, and since the speed is slower going upwind than downwind.

2.3 Computational Fluid Dynamics

The ability to model the flow of a fluid around a body with the help of powerful computers is one research area with a lot of attention. Computational fluid dynamic (CFD) techniques are used to solve the fluid flow problem by modelling the physical phenomenon and discretizing the resulting differential equations, which then become algebraic. Naval architects use CFD in areas such as hull design, propeller design, vibration analysis and much more. The data from the computations can be used to choose the correct engine power, prevent cavitating propellers or minimizing noise on a passenger ship. It can also be used to optimize the hull shape of a ship by computing the resistance of hulls with varied geometry, which is what is done in this study.

The alternative to CFD is model testing or calculations with empirical formulas. Both have their downsides. Model testing is usually very accurate, but time consuming and expensive to execute. Therefore extensive testing of different designs is often avoided. Today, model testing is often used as a tool to validate the results from computational hydrodynamics, or in research areas where CFD tools have not yet proved to be sufficiently accurate. Hand calculations with empirical formulas originating from experiments sometimes work fine within certain areas of interest but they are often not applicable in areas outside of what intended for. They are more used for guidance than actually as a tool in the detailed design process.

So, CFD provides a very powerful tool in terms of flexibility and cost efficiency if used properly. Because not all software suits all applications, one can easily be misled by the results. To reduce the risk of obtaining misleading results, validation and verification of the CFD software is conducted.

2.3.1 Verification and Validation

When modelling the physical phenomenon and discretizing the resulting differential equations that are used to solve the fluid flow problem, errors and uncertainties are introduced. Hence, the degree of accuracy is a significant concern for numerical solutions. Verification and validation is a method used to estimate the accuracy of the numerical computation. In general, verification is a method to estimate the numerical error or uncertainty in an iteration and discretization process of CFD computations, and validation is a method used to reveal the total error and uncertainty due to both the numerical and physical modelling errors.

2.3.1.1 Verification

Verification gives a quantified estimation of the numerical error or uncertainty in a CFD computation. The numerical error of a CFD computation has its origin in the round-off, discretization and iterative errors. The round-off errors are usually assumed to be negligible. In this thesis, since the simulations were merely conducted within steady flows, the discretization error is only caused by the limited grid resolution. Therefore, the assumption is made that the numerical uncertainty, U_{SN} , is simply yielded by the iterative uncertainty, U_I , and the grid discretization uncertainty, U_G . The iterative uncertainty is attributed to the incomplete convergence in the iteration progress, while the discretization error is caused by the discretization of the differential equations used in the model.

The numerical uncertainty is introduced as:

$$U_{SN} = \sqrt{U_I^2 + U_G^2} \quad (2.4)$$

If the iterative uncertainty is much smaller than the discretization uncertainty, (e.g. in Least Square Root (LSR) method (Eça & Hoekstra, 2006a), the iterative error must be two orders smaller than the discretization error) the iterative uncertainty can be discarded and the numerical uncertainty is approximated as:

$$U_{SN} = U_G \quad (2.5)$$

A grid convergence study is used to estimate the grid discretization uncertainty, and all the grids are compared to the finest grid. There are several methods and the Least Square Root method is the one used in this thesis for quantifying the uncertainty. The estimated exact solution should lie in the interval which bounds the uncertainty with 95% probability:

$$S - U_{SN} \leq S_0 \leq S + U_{SN} \quad (2.6)$$

where S_0 is the exact solution estimated by the numerical simulation and S is the simulation result with the finest grid. The estimated exact solution is obtained by extrapolating the simulated results to the grid with zero step size.

2.3.1.2 Least Square Root method

The LSR method is a method used for grid convergence studies and is developed by Eça et al (2010b). In the LSR method, the scatter of the numerical solutions is taken into account and the Least Squares Root approach is used to determine the order of accuracy and the numerical error. To apply the method, the solutions from more than three grid densities are required.

In the LSR method, ε_{RE} indicates the discretization error, and it is determined by general Richardson Extrapolation (Roache, 1998):

$$\varepsilon_{RE} \cong \delta_{RE} = S_i - S_0 = \alpha h_i^p \quad (2.7)$$

where δ_{RE} is the grid discretization error, S_i is the numerical solution on the i -th grid, h_i denotes the grid size ratio and $i = 1, 2, \dots, n_g, n_g > 3$ is the grid number; S_0 is the estimated solution by extrapolating to the zero-step grid, and p is the order of accuracy of the numerical method.

From the classical Richardson Extrapolation:

$$\delta_{RE} = S_i - S_0 = \alpha h_i^{p_{th}} \quad (2.8)$$

where p_{th} is the theoretical order of accuracy; α and S_0 may be computed with two known solutions. In ship hydrodynamics, LSR method is designed to be computed with a theoretical second-order-accuracy (Zou, 2012), i.e. $p_{th} = 2$ is assumed.

There are three unknowns (S_0, α, p) in equation (2.8) and therefore more than three solutions are needed.

With the curve fit of the Least Squares Root approach, the order of accuracy, p , can be estimated by minimizing the following function (Eça & Hoekstra, 2006a):

$$f(S_0, \alpha, p) = \sqrt{\sum_{i=1}^{n_g} (S_i - (S_0 + \alpha h_i^p))^2} \quad (2.9)$$

The convergence condition of simulation results are based on the rules as below:

Monotonic convergence: $p > 0$

Oscillation convergence: $n_{ch} > INT\left(\frac{n_g}{3}\right)$

where n_{ch} is the number of triplets with $(S_{i+1} - S_i)(S_i - S_{i-1}) < 0$

Anomalous behaviour: Otherwise

Since the scatter of the numerical solutions is considered in the LSR method, the observed accuracy p depends on the scatter, and therefore the numerical error ϵ_{RE} estimated in this method is not only derived from δ_{RE} which it would be according to the general RE. If $p \leq 0$, the convergence is not monotonic, the numerical error can be estimated by the three other alternative methods, which are stated as below.

$$\delta_{RE}^{02} = S_i - S_0 = \alpha h_i^2 \quad (2.10)$$

$$\delta_{RE}^{12} = S_i - S_0 = \alpha_{11} h_i + \alpha_{12} h_i^2 \quad (2.11)$$

$$\delta_{\Delta M} = \frac{\Delta M}{\left(\frac{h_{n_g}}{h_1}\right)^{-1}} \quad (2.12)$$

where ΔM is the data range, $\Delta M = \max|(S_i - S_j)|, 1 \leq i, j \leq n_g$; h_{n_g} is the step size of the n_g^{th} grid.

The first two estimates are obtained from curve fitting which is same as in Richardson Extrapolation.

The standard deviation of the curve fit for the equations are calculated as follows:

$$U_{SD} = \sqrt{\frac{\sum_{i=1}^{n_g} (S_i - (S_0 + \alpha_i h_i^p))^2}{n_g - 3}} \quad (2.13)$$

$$U_{SD}^{02} = \sqrt{\frac{\sum_{i=1}^{n_g} (S_i - (S_0 + \alpha_i h_i^2))^2}{n_g - 3}} \quad (2.14)$$

$$U_{SD}^{12} = \sqrt{\frac{\sum_{i=1}^{n_g} (S_i - (S_0 + \alpha_{11} h_i + \alpha_{12} h_i^2))^2}{n_g - 3}} \quad (2.15)$$

The numerical uncertainty of LSR follows the form used in Roache (1998):

$$U_{SN} = F_S \cdot |\epsilon_{RE}| \quad (2.16)$$

where F_S is the factor of safety.

The numerical uncertainty is formulated based on the convergence condition, and the standard deviations are introduced into the equations which are stated as below:

Monotonic convergence:

$$0 < p < 0.95 : U_{SN} = \min(1.25\delta_{RE} + U_{SD}, 3\delta_{RE}^{12} + U_{SD}^{12}) \quad (2.17)$$

$$0.95 \leq p \leq 2.05 : U_{SN} = 1.25\delta_{RE} + U_{SD} \quad (2.18)$$

$$2.05 \leq p : U_{SN} = \max(1.25\delta_{RE} + U_{SD}, 3\delta_{RE}^{02} + U_{SD}^{02}) \quad (2.19)$$

Oscillatory convergence:

$$U_{SN} = 3\delta_{\Delta M} \quad (2.20)$$

Anomalous behaviour:

$$U_{SN} = \min(3\delta_{\Delta M}, 3\delta_{RE}^{12} + U_{SD}^{12}) \quad (2.21)$$

2.3.1.3 Validation

Validation reveals the estimated error and uncertainty of both the numerical computing process and the corresponding model by comparing the numerical solution to the experimental data. Rather than simply giving pass or fail statement, the process of the V&V 2009 Standard (ASME, 2009) provides a quantitative assessment for validation.

In the standard, the validation comparison error, E , and the validation uncertainty, U_{val} , are introduced.

The comparison error, E , is defined as below:

$$E = S - D \quad (2.22)$$

where S is the numerical estimated solution and D is the experimental data.

The error in the numerical solution is the difference between the solution, S , and the true value, T_v :

$$\delta_S = S - T_v \quad (2.23)$$

Similarly, the error in the experimental data is:

$$\delta_D = D - T_v \quad (2.24)$$

Therefore, the comparison error can be written as:

$$E = S - D = (T_v + \delta_S) - (T_v + \delta_D) = \delta_S - \delta_D \quad (2.25)$$

The error in the numerical solution S is contributed from:

- the modelling error δ_{model} due to the modelling approximation
- the numerical error δ_{num} due to the numerical solution of mathematical equations
- the input parameter error δ_{input} due to the input parameter to the simulation

Consequently, the error in the numerical solution can be expressed as:

$$\delta_S = \delta_{model} + \delta_{num} + \delta_{input} \quad (2.26)$$

Therefore, the comparison error E is written as:

$$E = \delta_{model} + \delta_{num} + \delta_{input} - \delta_D \quad (2.27)$$

and thus the modelling error δ_{model} is indicated to be:

$$\delta_{model} = E - (\delta_{num} + \delta_{input} - \delta_D) \quad (2.28)$$

Even though the sign and the magnitude of comparison error E can be decided by a known numerical solution and experimental data, the signs and magnitudes of δ_{num} , δ_{input} and δ_D are unknown. Hence, the corresponding standard uncertainties, U_{num} , U_{input} and U_D are introduced.

The validation uncertainty U_{val} is defined as an estimation of the standard deviation of the parent population for the combined errors ($\delta_{num} + \delta_{input} - \delta_D$). If the three errors in Equ 2.28 are effectively independent, the validation uncertainty U_{val} can be noted as follows:

$$U_{val} = \sqrt{U_{num}^2 + U_{input}^2 + U_D^2} \quad (2.29)$$

Then the modelling error δ_{model} falls in an interval expressed as:

$$\delta_{model} \in [E - U_{val}, E + U_{val}]$$

The goal is the estimated interval which the modelling error lies should be bounded within 95% confidence. This means that U_{val} is twice the standard deviation.

If $|E| < U_{val}$, the modelling error lies in the “noise level” caused by the three uncertainties, Eça et al (2010), and therefore the solution could be said to be validated. On the other hand, if $|E| \gg U_{val}$, the model should be improved to reduce the comparison error.

2.3.2 Governing Equations

The following chapters will briefly describe the computational methods used to calculate the viscous flow in the study. The potential flow computations are not handled here since they are not used very extensively. However, for deeper understanding of inviscid flow (also referred to as potential flow) and viscous flow calculation methods further reading in Larsson & Raven (2010) is advised.

2.3.2.1 Reynolds-averaged Navier-Stokes (RANS) equations

The RANS equations are all based on the Navier-Stokes equations, seen in compact, incompressible form below

$$\frac{\partial u_i}{\partial t} + u_j \frac{\partial u_i}{\partial x_j} = -\frac{1}{\rho} \frac{\partial p}{\partial x_i} + F_i + \nu \frac{\partial^2 u_i}{\partial x_j \partial x_j} \quad (2.30)$$

and on the continuity equation for incompressible flows;

$$\frac{\partial u_i}{\partial x_i} = 0 \quad (2.31)$$

Theoretically, the Navier-Stokes equations are possible to solve for the flow around a yacht. But to be able to solve for every turbulent eddy would require much more computer power than practically possible. This is because the smallest eddies according to Larsson & Raven (2010) are about 0.1 mm in size, while the domain is the order of a few boat lengths in all directions. Therefore, in the Reynolds-averaged Navier-Stokes equations, the mean flow of each element is solved instead of computing every turbulent fluctuation in the domain. This is done by time averaging the equations with time steps larger than the largest turbulent scale, but smaller than the scale for mean flow variations. This is a rather complicated operation and it is best followed in Larsson & Raven (2010). The final expression looks like below;

$$\frac{\partial}{\partial t} + \frac{\partial}{\partial x_j} (\bar{u}_i \bar{u}_j) = -\frac{1}{\rho} \frac{\partial \bar{p}}{\partial x_i} + F_i + \frac{1}{\rho} \frac{\partial}{\partial x_j} (R_{ji} + \sigma_{ji}) \quad (2.32)$$

Equation 2.3.2 is the basis for all RANS methods. All turbulent fluctuations have been removed from the equations, but R_{ji} is still left unknown. This term is called the Reynolds stress and it is the correlation between two fluctuating velocity components. It consists of six independent components, and to compute these, a turbulence model is required. Turbulence models contain many empirical constants in order to compute and describe the very complex turbulent flow, and a lot of research is being done in this topic. There are numerous models being used but no model is good enough to

work for all flow conditions. The most common turbulence model in ship flow computations is, again according to Larsson & Raven (2010), a so called two equation model, the $k - \omega$ turbulence model.

2.3.3 Free surface capturing - Volume of Fluids (VOF) method

The VOF method uses a transport equation for the volume fraction in a cell. If the cell is full of water, the volume fraction is 1, and if it is full of air it is 0. If the volume fraction is somewhere in between 1 and 0, there is a mix of air and water in the cell. In this way the free surface is detected. Actually, a band of cells with volume fractions not equal to 1 or 0 is detected. The water surface is set to occur at volume fraction equal to 0.5, and this value is interpolated from volume fractions of the cells in the “surface band”. The surface is then generated by connecting the interpolated points that are equal to 0.5. Both the interpolation and the generation of the surface is a post processing issue, and is not really a part of the VOF method solver process.

2.3.4 SHIPFLOW 5.0

The CFD software used in the study is SHIPFLOW 5.0 developed by FLOWTECH International AB in Gothenburg which is a spinoff company from the research done at the Hydrodynamics group of Chalmers University of Technology. It is primarily being developed for applications within the ship design business and can handle several disciplines within this area covering both viscid and inviscid solutions. It is vastly used in the industry. The software is divided into several modules handling different aspects of the computations;

- XPAN is a free surface potential flow panel solver
- XBOUND calculates the thin boundary layer on the hull based on the potential flow pressure
- XMESH generates the mesh used by XPAN and XBOUND
- XCHAP is a finite volume RANS solver with $k - \omega$ SST and EASM turbulence models for the viscid flow computations
- XVOF is the viscous free surface capturing module that uses the volume of fluids method. The module is utilized by XCHAP.
- XGRID generates the grids used by XCHAP and XVOF

3 Method

The study consists of three major steps, apart from the pre-study. The first step is the verification, the second is validation and the third is optimization. Two sailing conditions have been set up for the computations. One is an upright case, and the other is a case where the hull is heeled 20° to leeward. The first sailing condition is thought to represent a scenario where the yacht is going downwind, while the latter case represents the yacht sailing upwind. In the first two steps, hulls and experiment data from DSYHS is used. For the optimization part a 41 feet sailing yacht is designed and equipped with different systematically varied transoms and tested in both conditions with the ambition to find an indication of what an optimum transom stern should look like.

3.1 Pre-study of the Delft hull series

The Delft Systematic Yacht Hull Series (DSYHS) is a series of hulls with systematically varied geometry that has been developed since 1975 at Delft University of Technology in the Netherlands, Keunig & Katbert (2008). As of today it consists of 55 designs divided into seven sub-series. All hulls are named Sysser NN, with NN representing the design number. For each design there has been produced a scaled down model on which several different towing tank tests have been performed to see what effect various design features have on the resistance of the hull. Tests have been made with and without appendages, at several heel angles, and with varying leeway and trim angles. All data from the tests has been collected throughout the years in the DSYHS database which is today widely spread and used in several important applications.

One such application based on the data is the development of a mathematical formula for the residuary resistance of an untrimmed upright bare hull at different speeds. This formula takes several important design parameters of the hull into consideration and the formula serves as the basis in most Velocity Prediction Programs and yacht handicap racing rules of today.

Another application is the one used in this study, where results from computational fluid dynamic software's can be validated against the experimental data from the DSYHS database. For the study, hulls from DSYHS Series 40 have been chosen to validate the SHIPFLOW software against. The hulls from this series are the ones with hull lines and main parameters most similar to the modern performance cruisers. Especially, a hull with a wide transom and straight buttocks is desired which is found in the Sysser 47 hull (Figure 3.1.1). This hull was later used in the verification part of the study. Data of the DSYHS hulls used in the study is found in Table 3.1.1.

Table 3.1.1. Main data of the DSYHS hulls used in the study. The data is full scale, in the computations model scale was used.

Sysser no	Lwl [m]	Bwl [m]	Tc [m]	Vol [m ³]	Lcb [m]	Aw [m ²]	Lcf [m]	Ax [m ²]	Sw [m ²]	Cb	Cm	Cp	Cw
46	10.00	3.01	0.54	6.42	-0.33	20.13	-0.63	1.16	22.68	0.39	0.71	0.55	0.67
47	10.00	3.00	0.50	6.10	-0.60	20.95	-0.84	1.11	23.14	0.41	0.75	0.55	0.70
48	10.00	3.00	0.52	6.26	-0.06	20.66	-0.50	1.12	23.07	0.40	0.73	0.56	0.69
49	10.00	2.98	0.47	5.94	-0.63	20.85	-0.84	1.05	23.05	0.42	0.74	0.57	0.70
50	10.00	3.00	0.47	5.94	-0.79	20.64	-0.91	1.10	22.92	0.42	0.78	0.54	0.69

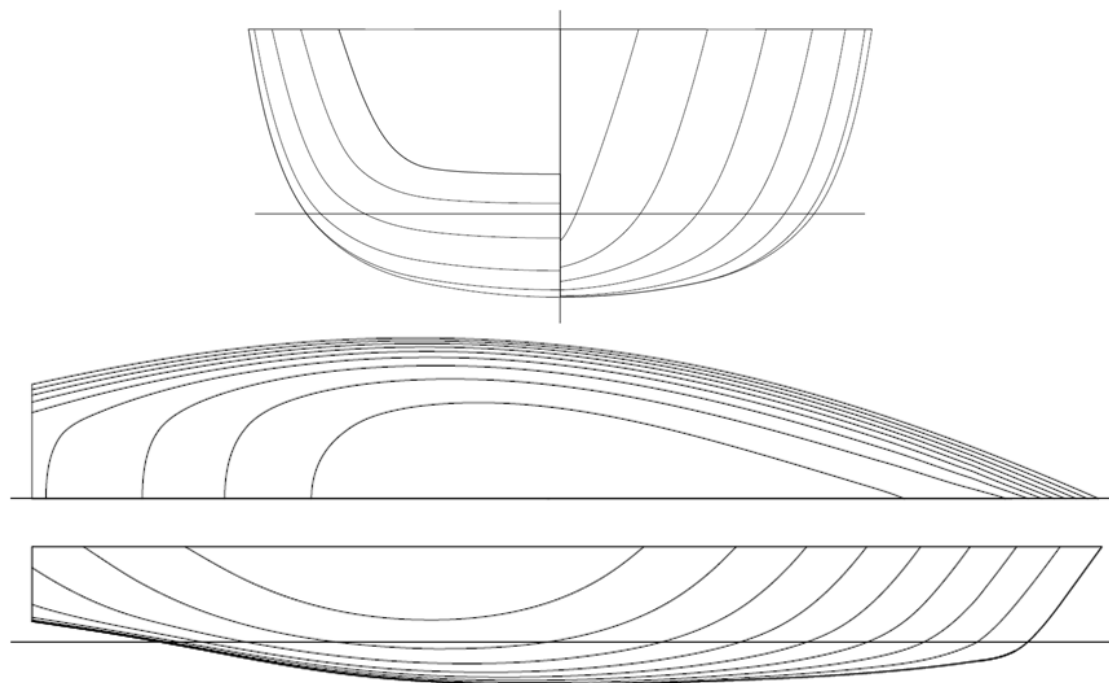


Figure 3.1.1. Lines plan of the Sysser 47.

3.2 Verification

In this part of the study hull Sysser 47 is used. For both upright and heeled cases, the sinkage and trim of the hulls are fixed during the calculations according to the DSYHS measurement data in order to have comparable results.

In the verification phase the objective is to find a grid that is fine enough for the numerical error to be sufficiently small (solution verification). There is also a possibility to check that the computer code performs as expected (code verification). The Least Square Root-method (LSR-method) is used to choose a grid that is sufficiently fine, see Chapter 2.3.1 for more theory about this method. Usually, the finer the grid the better the results, but this comes at the cost of an increased computational effort. One way to save computational time is to distribute the grid

density differently such that smaller cells are used where large gradients in the flow variables are expected, while bigger cells can be used away from these regions.

For this study, verification was first made for the upright case using one hull, namely Sysser 47, at Fn 0.25, 0.40 and 0.60. Six different grid densities were evaluated, with the refinement factor between each grid equal to $2^{1/4}$. The total amount of cells ranges between 550 000 and 6 700 000.

With the knowledge gained from the upright hull case, verification on the heeled case was done at Fn 0.35. Also for this case hull Sysser 47 was used. Four grid densities were tested with a grid refinement factor of $2^{1/8}$ and total amount of cells ranging from 2 900 000 to 6 100 000. The needed number of iterations is governed by how well the solution converges, and in this study the solution is considered to have converged when the standard deviation for the pressure coefficient is below 1%.

Apart from the amount of cells, investigations were also made on other parameters for the grid.

The grid can be modified in several ways (see Figure 3.2.1 and Table 3.2.1). First the domain size is defined upstream, downstream and radially. The domain is extended upwards above the free surface and hull. Radially it covers 3 boat lengths. Longitudinally it is divided into five regions along the hull in which the grid can be modified by changing the amount of cells and the cell distribution. Also, the borders between the regions can be moved.

The volume of fluids method requires some additional settings, which are seen to the right in Figure 3.2.1. Just below and above the still water plane the grid is made a lot denser to allow for more precise surface tracking. The upper (HABO) and lower (HUND) boundaries of this finer grid region have rather large impact on the results.

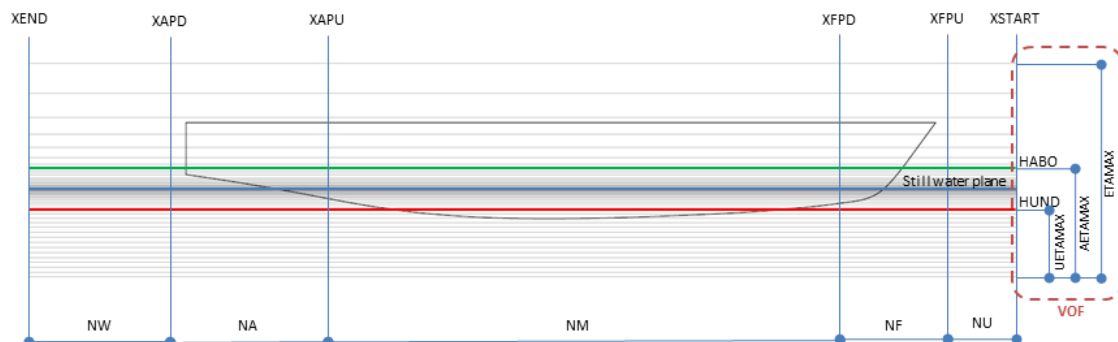


Figure 3.2.1. The different grid regions and its definitions.

The distance at which the free surface attaches to the hull is defined by the LVCDIST command (see Figure 3.2.2). This command is created to prevent a numerical error to occur where air is seemingly sucked down between the hull surface and the water. It will affect the calculated wetted surface of the hull and thus directly influence the total resistance. LVCDIST is desired to be kept at a minimum to mimic reality, but the solver cannot handle too small values. Therefore several values are tested for this function until a value that is sufficiently small, but still allows the solver to be stable, is found.

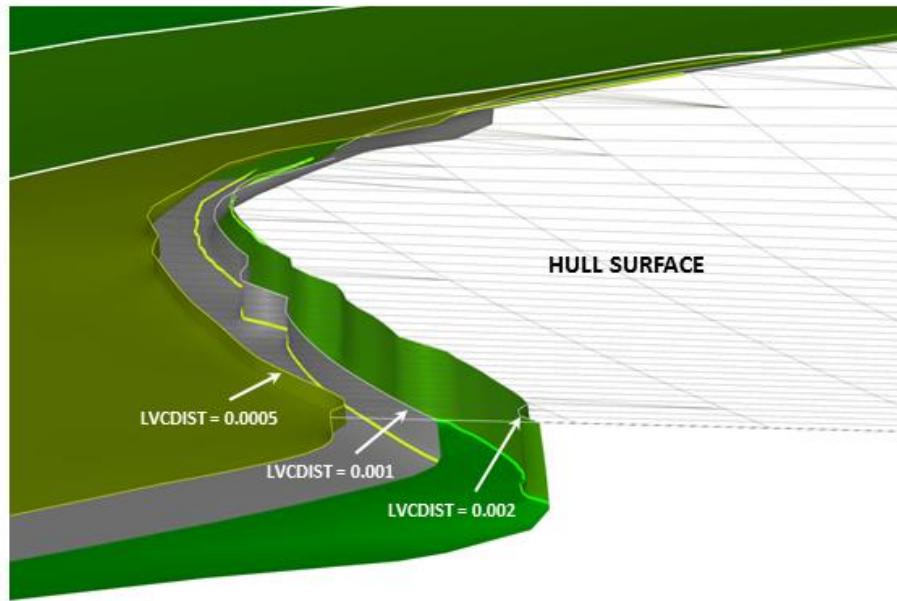


Figure 3.2.2. Plot from SHIPFLOW illustrating where the free surface attaches to the hull in the stern region with variable settings for LVCDIST.

The grid settings found to work best and which was later used in the validation of heeled and upright cases are seen in Table 3.2.1.

Table 3.2.1. Grid settings found in the verification and to be used in the validation.

	<i>Upright</i>	<i>Heeled</i>	
XCHAP	XSTART	-1.000	-1.000
	XFPU	-0.050	-0.050
	XFPD	0.225	0.225
	XAPU	0.880	0.880
	XAPD	0.990	0.990
	XEND	4.000	4.000
	LVCDIST	0.001	0.001
	YTAR	0.987	1.280
	NU	32	25
	NF	77	65
	NM	92	71
	NA	78	59
	NW	53	40
ZETAMAX	71	55	
XVOF	HABO	0.025	0.040
	HUND	-0.006	-0.005
	UEATAMAX	42	71
	AETAMAX	86	87
	ETAMAX	104	107

For an upright hull, there is symmetry along the centre line. The symmetry can be used in the computations since the flow also is approximated to be symmetric and thus, a half model of the yacht is enough to represent reality. But when the yacht is heeled and trimmed there is no symmetry along the centre line. The grid generator is not developed for this purpose and still only grids for half models of the hull can be generated. Problems occur at the negatively inclined surfaces, when the cross sections of the half model turns sharply upwards after having passed the lowest point of the hull, see Figure 3.2.3. Such a region of the hull is near the bow and at the stern for more box shaped transoms. The problem is solved in two steps. The first step is taken care of in a CAD software. The heeled and trimmed hull is cut in two, not at the centreline, but at an angle. The cut is a straight line placed approximately at the line where the hull has its deepest draft when heeled. This will cause the better part of the “negative” areas to be avoided. In the bow, however, there are still sharp curvature and negative surfaces that needs to be avoided. This is done by remodelling the bow area in such a way that the stem is vertical and placed in the cutting plane, see picture 3.2.3. The influence of the remodelling is believed to be small since the bigger modifications are made well above the waterline.

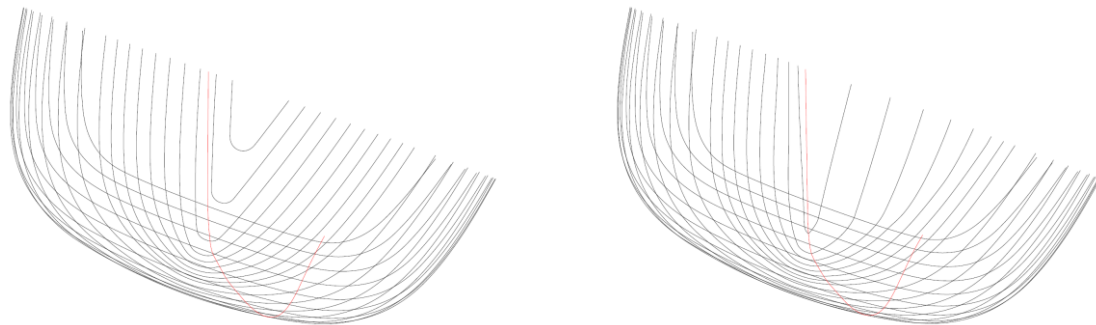


Figure 3.2.3. The Sysser 47 before (left) and after (right) the modification of the bow due to the grid problems. The red line is the line along which the hull is cut into two halves. Note how the bow sections have their deepest point along or close to the cutting plane in the modified bow.

The second step has to be made in SHIPFLOW where one grid for each half is to be generated (Figure 3.2.4) and then imported into the RANS solver module. In this case, when the halves are not cut at the centreline, the flow angle to the hull will be at the angle of the cut. This is since the grid is created with this cutting plane as the centre plane. The software developer has created a feature where the grid region near the hull can be twisted to the desired angle, see Figure 3.2.5. By doing this the correct flow angle to the hull can be achieved.

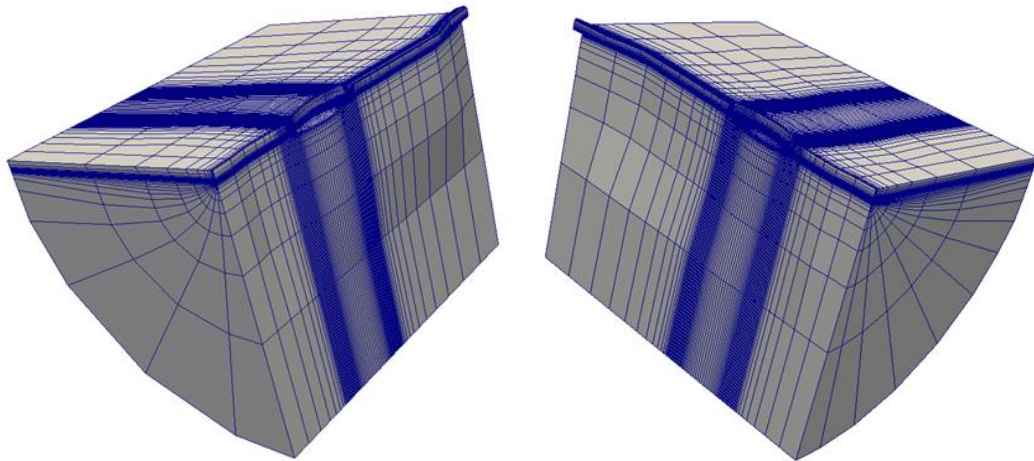


Figure 3.2.4. The windward (left) and leeward (right) domains for a Sysser 46 heeled case. Note how the regions near the hull are twisted. Only every third gridline is displayed in the plot.

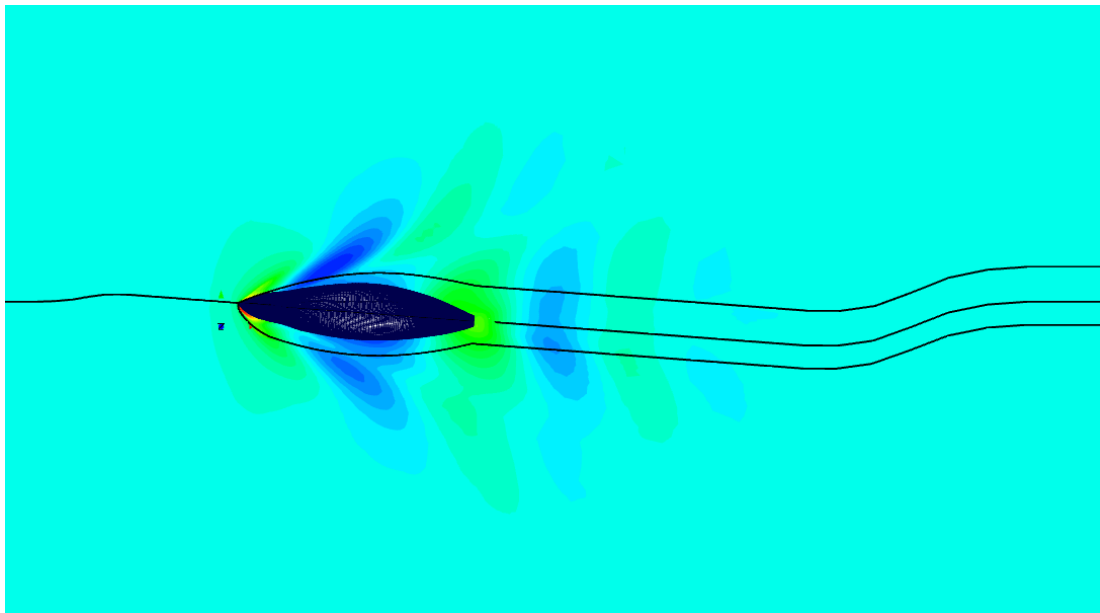


Figure 3.2.5. Top view of the free surface where the black lines are representing the grid boundaries separating the leeward and windward grids. The dark blue contour in the middle is the wetted part of the hull when heeled. The flow direction is aligned with the black lines in the inlet and outlet sides of the grid, while the grid is rotated in the region near the hull to compensate for the angle at which the hull is cut longitudinally.

3.3 Validation

Validation is done on several DHSYS hulls at different speeds to see how well the solver handles different geometries without changing the grid resolution. The results from the SHIPFLOW calculations are compared with the ones from the DHSYS database. For the upright hull verification is made with Sysser 46, 47 and 50 at Fn 0.25, 0.30, 0.40, 0.50, 0.60 and 0.70, and for Sysser 48 and 49 at Fn 0.25, 0.40 and 0.60. The heeled case is validated with Sysser 47 and 48 at Fn 0.25, 0.30, 0.35, 0.40 and 0.45. Since the uncertainties from the towing tank tests (U_D) are not known, the

validation uncertainty (U_{val}) cannot be computed. Therefore, only the difference between the computed and measured values (E) is presented. The residual resistance of the CFD results are also compared to the results that are generated by the Delft formulas for upright hulls, Keuning & Katgert (2008).

3.4 Optimization

3.4.1 Creation of the ND41

The last part of the study is about optimizing the transom and aft body of a modern 41 feet performance cruiser. The hull for this yacht is intended to be somewhat of a mean of current production boat designs in the same segment, thus a short study of seven of those is performed.

Deck lines, rocker lines (Figure 3.4.1.1) and main dimensions (Table 3.4.1.1) are gathered to obtain a basis for the New Design 41 (ND41). The lines are mainly found from renderings from the producers, thus their accuracy can be questioned. Unfortunately, not enough cross sections are found. Main dimensions are from producers homepages. From the data gathered the mean values are calculated and from these, three design ratios are created which will set the main dimensions of the ND41, with the LOA of 41 feet (12.50 m) being the basis. The ratios used are Lwl/Beam, Displacement/Lwl and Loa/Lwl.

Table 3.4.1.1. Main dimensions of some modern 40 feet performance cruisers and the derived dimensions of the ND41.

Model	Loa [m]	Lwl [m]	Beam (deck) [m]	Displ [kg]	Lwl/Beam	Displ/Lwl	Loa/Lwl
X-41	12.35	10.69	3.64	6800	0.34	636.11	1.16
Salona 41	12.50	11.45	3.84	7200	0.34	628.82	1.09
Elan 400	11.95	11.26	3.87	7500	0.34	666.07	1.06
Dehler 41	12.40	11.00	3.90	8195	0.35	745.00	1.13
First 40 CR	12.24	10.67	3.89	7900	0.36	740.39	1.15
Dufour 40 E	12.35	10.76	3.89	7950	0.36	738.85	1.15
Arcona 410	12.20	11.20	3.90	7800	0.35	696.43	1.09
Mean	12.28	11.00	3.85	7620.71	0.35	693.10	1.12

Target dimensions of New Design 41			
Loa [m]	41 ft	12.50	m
Lwl [m]		11.19	m
Beam (deck) [m]		3.91	m
Displacement [kg]		7754	kg

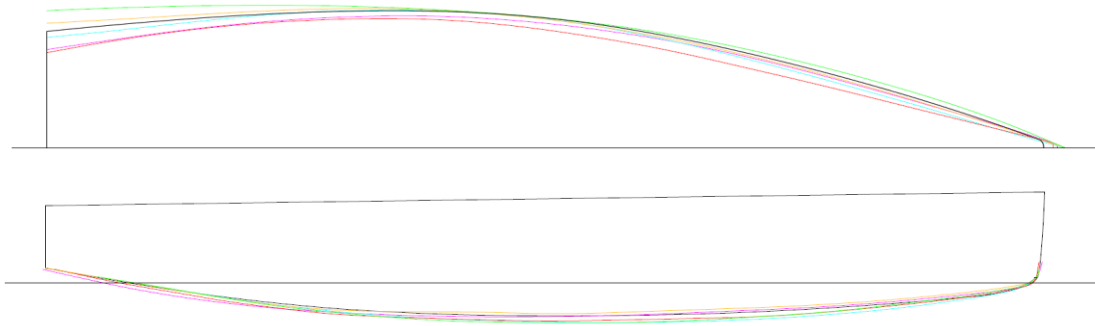


Figure 3.4.1.1. Deck and rocker lines of modern 40 feet performance cruisers (colored) and the black lines are the ones of the ND41.

The new hull design generated from these studies is created in the CAD software Rhinoceros 3D 4.0 (Figure 3.4.1.2 and Table 3.4.1.2). The design is given a rather boxy transom and aft sections to be used as a starting point in the hull variation studies later on. Transom width is however not that extreme, again to allow for more variations later on. The rocker line is fairly straight when compared to many of the studied hulls. The fore ship is a bit wider and with more volume than most other hulls. Mainly because this will make the bow geometry modification for the heeled case easier, but also to obtain less changes in sinkage and trim when the geometry of the aft body is altered and the displacement is to be kept constant.

Table 3.4.1.2. Main dimensions of the ND41.

New Design 41			
<i>Length over all</i>	12.29 m	<i>Displacement</i>	7 742 kg
<i>Length water line</i>	11.10 m	<i>Wetted surface</i>	28.88 m ²
<i>Beam over all</i>	3.90 m	<i>Lcb/Lwl (from AP)</i>	0.457
<i>Beam water line</i>	3.38 m	<i>Lcf/Lwl (from AP)</i>	0.422
<i>Draft of canoe body</i>	0.47 m	<i>Prismatic coefficient</i>	0.562

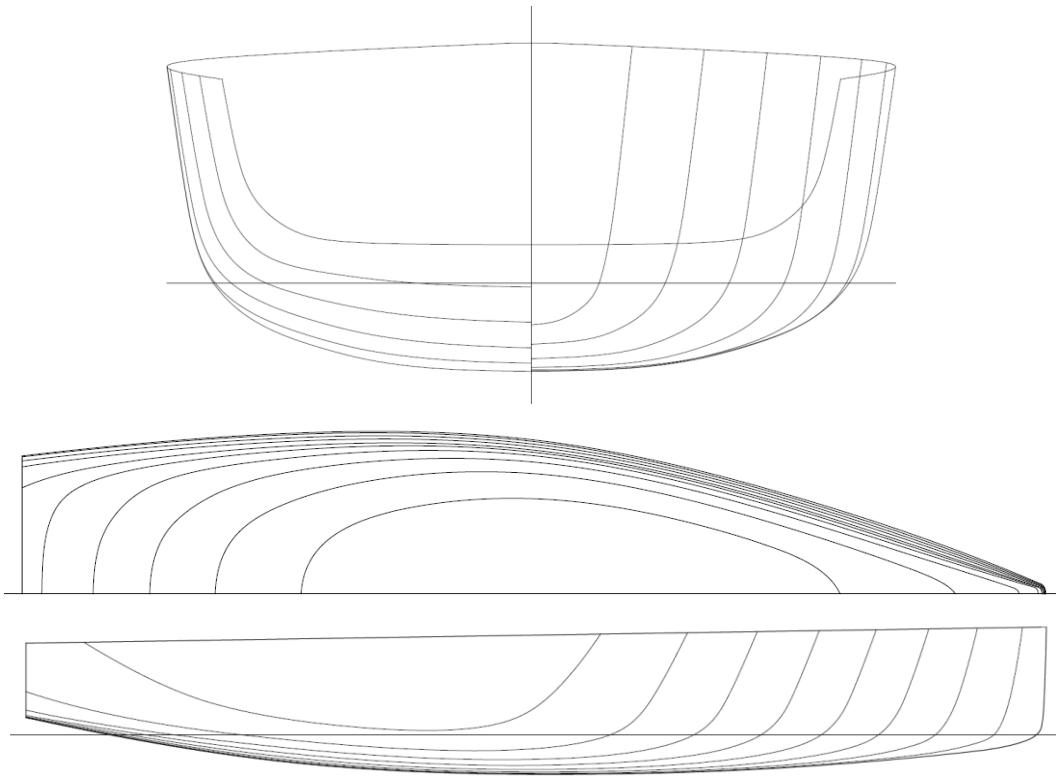


Figure 3.4.1.2. Lines plan of the ND41.

3.4.2 Hull geometry variations

A systematic variation of the transom size and shape is desired in order to obtain useful knowledge. Unfortunately, only changing the transom is not possible without changing the geometry of the aft body. In this study, the hull geometry is kept constant from bow to mid ship and from there it is systematically varied.

First way to vary the aft ship is to stretch it aft wards in steps of 10 percent, starting from the mid-section. The hulls are then cut at the original transom to obtain the same length over all for all hulls. To compensate for the influence of the mid-section on the geometry, which is quite round compared to the transom, the new transoms are modified such that the new transoms look more like the boxy initial transom. Six new hulls are created in this manner, and two additional hulls are created with steps 80 and 100 percent, so a total of nine hulls are now created (see Figure 3.4.2.1). The hulls are named ND41-00b to ND41-100b, where 00-100 indicates the stretching in percent, and b is for the boxy transom. By doing this variation, both transom size and transom submergence can be investigated. The transom submergence is a side effect of the stretching of the aft ships due to the fact that they are cut at the same Loa . The transom area immersion ratio, the immersed transom area (A_t) divided by the immersed area of the maximum area section (A_x), ranges between 0 (not submerged) to 0.67 (see Table 3.4.2.4) which according to Larsson & Raven (2010) should exceed the optimal transom immersion at the two Froude numbers investigated in the study. To have consistency in the experiments all hulls are kept at the same displacement and thus the draft must be slightly adjusted.

Figure 3.4.2.1. The nine different hulls created by stretching the aft ship and modifying the transom geometry where the black line is the original ND41 design. The transoms are seen in the top picture with the varying waterlines in order to keep the displacement constant regardless of hull geometry.

To further investigate the optimum shape of the transom, hulls ND41-00b, -20b, -40b, -60b, -80b and 100b are chosen to be modified with different transom geometries. The boxy transom from the stretched hulls is used as one extreme, while one very round transom is created to serve as the other extreme. Between those extremes, an intermediately rounded transom is created. The submerged transom area is kept as constant as possible for transom shapes of the same transom size. Thus the transom immergence is different between the three transom shape variations. The new hulls are named for instance ND41-00i and ND41-00r, where i is for intermediate transom shape and r is for round transom shape. In total, 18 different hulls are created with different transom size and shape (see Figure 3.4.2.2 .3 .4).

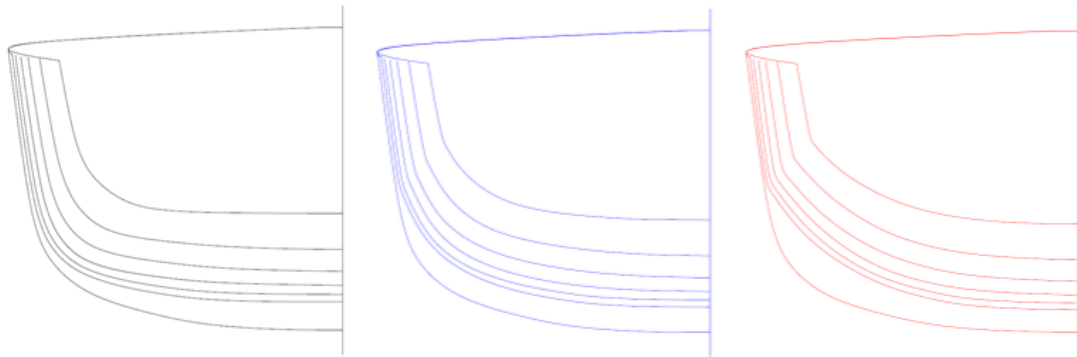


Figure 3.4.2.2. Picture of the 18 different transom variations. The black lines are the original boxy transoms, the blue lines are the intermediately rounded transoms and the red lines are the round transoms.

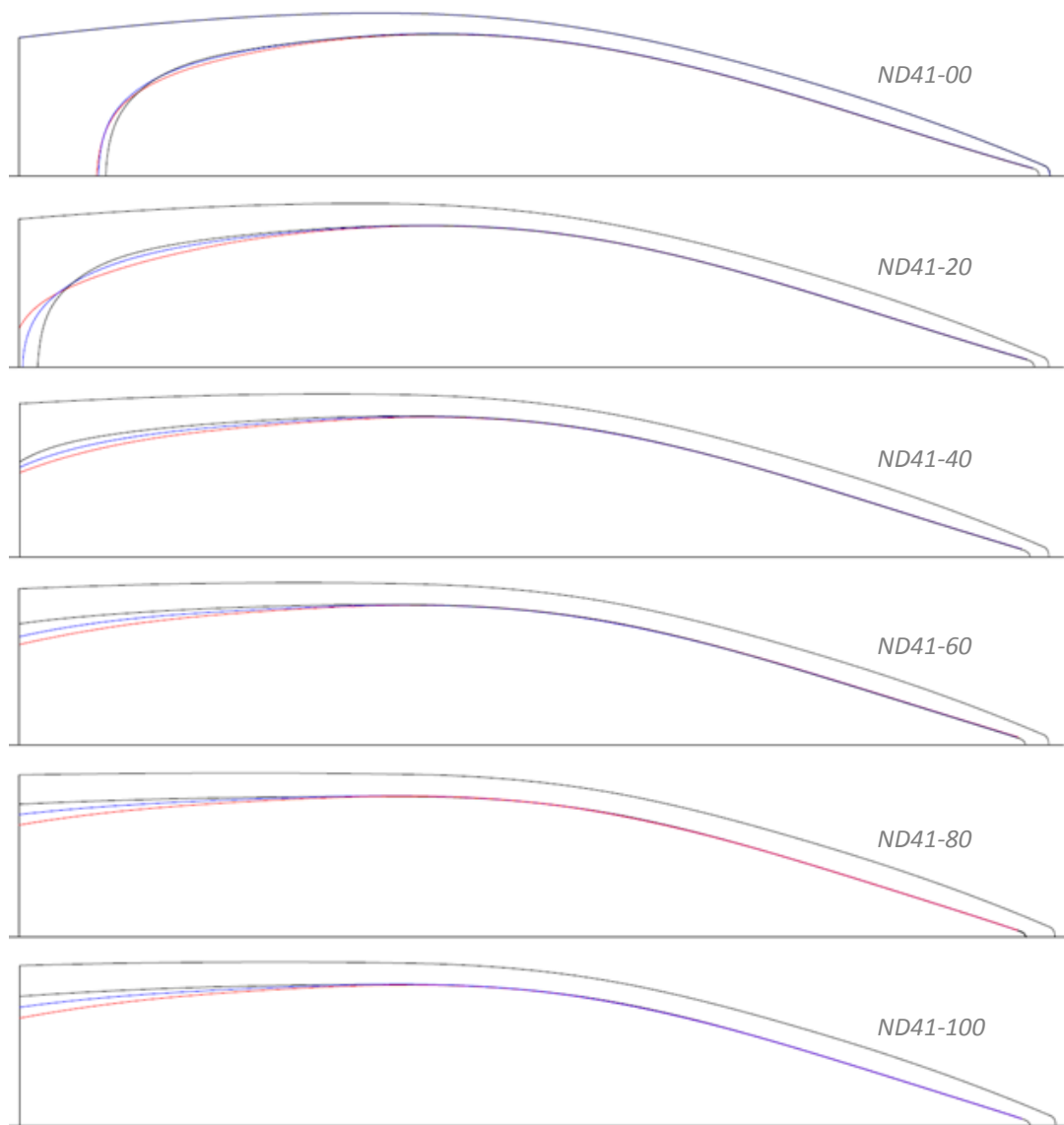


Figure 3.4.2.3. Waterlines of the six hulls (starting with ND41-00) with varied transom shape.

Table 3.4.2.4. Data of the hulls used in the optimization. At/Ax is the submerged transom area divided by the submerged maximum section area. The transom immersion is defined positive when the transom is immersed. All data are at even keel and zero speed.

Hull	Lwl [m]	Sw [m ²]	Cb	Cp	Lcb [% of Lwl]	UPRIGHT CONDITION		20° HEELED CONDITION	
						At/Ax	Trnsm immers. [% of Lwl]	At/Ax	Trnsm immers. [% of Lwl]
ND41-00b	1.715	0.686	0.427	0.562	-4.5	0.00	-1.88	0.03	0.7
ND41-10b	1.771	0.712	0.430	0.566	-3.8	0.00	-0.93		
ND41-20b	1.835	0.737	0.429	0.568	-3.5	0.00	-0.26	0.17	2.0
ND41-30b	1.855	0.757	0.438	0.580	-3.7	0.06	0.22		
ND41-40b	1.858	0.766	0.452	0.598	-5.1	0.10	0.55	0.33	3.0
ND41-50b	1.845	0.770	0.468	0.617	-5.9	0.20	0.90		
ND41-60b	1.849	0.773	0.480	0.631	-7.0	0.30	1.10	0.47	3.4
ND41-80b	1.845	0.773	0.494	0.633	-8.1	0.42	1.46	0.58	3.6
ND41-100b	1.841	0.771	0.509	0.652	-8.9	0.54	1.74	0.67	3.9
ND41-00i	1.724	0.686	0.425	0.551	-4.3	0.00	-1.62	0.01	0.3
ND41-20i	1.859	0.734	0.424	0.553	-2.9	0.00	-0.05	0.15	1.6
ND41-40i	1.858	0.754	0.449	0.592	-5.1	0.13	0.77	0.31	2.4
ND41-60i	1.850	0.761	0.472	0.627	-6.9	0.29	1.28	0.44	2.9
ND41-80i	1.845	0.763	0.486	0.629	-8.0	0.41	1.61	0.55	3.3
ND41-100i	1.841	0.764	0.499	0.644	-8.8	0.51	1.88	0.62	3.5
ND41-00r	1.731	0.686	0.459	0.559	-4.1	0.00	-1.46	0.00	0.0
ND41-20r	1.867	0.730	0.423	0.551	-2.7	0.01	0.16	0.13	1.3
ND41-40r	1.860	0.746	0.450	0.593	-5.1	0.16	0.97	0.28	2.1
ND41-60r	1.853	0.752	0.469	0.616	-6.7	0.32	1.52	0.42	2.6
ND41-80r	1.846	0.754	0.485	0.628	-7.8	0.41	1.79	0.51	2.9
ND41-100r	1.853	0.754	0.502	0.640	-8.4	0.50	2.01	0.58	3.1

3.4.3 CFD investigations of optimum transom stern

To be able to find an optimum transom stern, cases in the optimization phase are run with the SHIPFLOW CFD software with the settings obtained from the work previously performed in the study (see Figure 3.4.3.1). All CFD calculations are carried out at model scale and the waterline length is kept in the same range as the Sysser hulls that were used in the verification and validation phase. The scaling factor is approximately equal to 0.154. The fluid properties correspond to saltwater at 20°C.

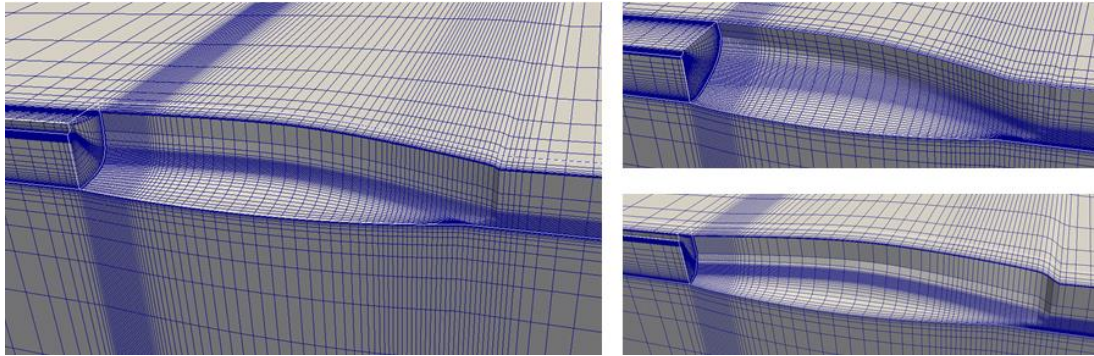


Figure 3.4.3.1. Plots of the grids used in the optimization. Left is the ND41-40i in upright condition and right is the ND41-40b in heeled condition, windward side (top right) and lee ward side (bottom right). Only every third grid line is shown in the plots.

The RANS solver in SHIPFLOW cannot handle free trim and sinkage of the yacht as for now and thus these parameters must be obtained some other way. There are two components to consider here. First, there is the trim and sinkage due to the speed of the yacht. Then there is also a trimming moment from the driving force acting in the centre of effort in the sails. This moment will usually counteract the trim due to speed. The driving force generated by the sails is equal to the resistance force from the hull as it moves through the water. The distance between the driving force from the sails and the centre of buoyancy of the yacht will act as the lever arm resulting in the trimming moment. The resistance force does not necessarily act at the centre of buoyancy, but it is a reasonable approximation. Since the ND41 has no sail plan designed, a lever arm is estimated to 7.6 meters (full scale) based on the YD41 from Larsson, Eliasson & Orych (2014). For the heeled case the lever arm is decreased according to basic trigonometry.

The potential flow module XPAN in SHIPFLOW can handle free trim and sinkage of hulls due to its speed, and it is also possible to account for a trimming moment from the sails or a towing point above the waterline. Since it is a potential flow solver, the missing resistance component due to viscosity must be added to the total resistance that is used in XPAN to obtain reliable trim and sinkage data. The viscous resistance is calculated using ITTC 57 formula from Larsson & Raven (2010). One XPAN run is made for each heel/speed configuration of each hull.

With known trim and sinkage, the cases can be set up in XCHAP to perform the RANS calculations. First the nine hulls with the stretched aft ship and boxy stern are run in upright condition at Froude number 0.6, corresponding to downwind sailing at 12 knots, to see if there is any optimum transom size in this condition.

The eighteen hulls with varying transom size and shape are tested in both upright and heeled conditions, at Froude numbers 0.6 and 0.35, to fill a full 18x4 matrix. Again, the modified grid generator with a twisted grid (see section about verification) is used to compensate for the flow direction and the bow geometry must be reworked. All hulls can be cut at the same angle longitudinally, and since the fore ship is identical for all hulls the same bow can be used for all cases. In this way, the error that might have been introduced by the reworked bow is kept constant for all hulls.

4 Results and Discussion

There are a lot of results produced throughout the study and therefore this chapter is divided into subchapters Verification, Validation and Optimization. Under each subchapter the results are presented first, and they are then followed by a discussion part. When there are several conditions (heeled, upright, different Froude numbers) in each sub chapter, each condition is handled separately. In the last subchapter about optimization there are subsections that further elaborate on the findings in the results of the optimization.

4.1 Verification

4.1.1 Upright condition

Table 4.1.1.1. Results from verification of Sysser 47 at upright condition and $Fn = 0.6$

Grid	Cf	Cp	Ct	Sw [m2]	Std (Cf)	Std (CpV)	Std (Ct)	CPU Time [h]	No of cells	Uncertainty [%]
G5	0.00320	0.00901	0.01220	0.83980	0.05%	0.06%	0.05%	176	900770	11.96
G4	0.00329	0.00910	0.01239	0.84009	0.02%	0.07%	0.06%	288	1480556	8.37
G3	0.00332	0.00913	0.01245	0.83863	0.04%	0.06%	0.05%	472	2457273	5.85
G2	0.00334	0.00918	0.01252	0.83922	0.01%	0.09%	0.07%	784	4078296	4.33
G1	0.00335	0.00923	0.01257	0.84009	0.00%	0.04%	0.03%	1328	6790528	3.06

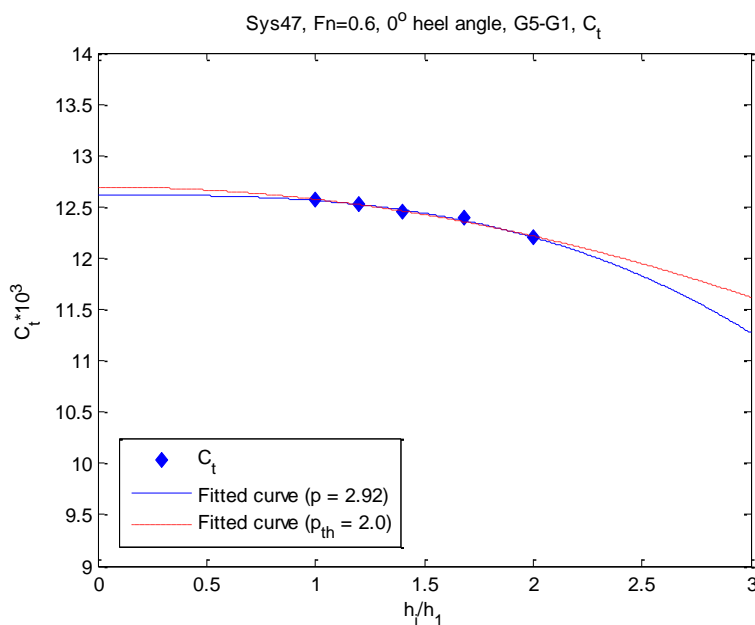


Figure 4.1.1.1. LSR curve fit

Table 4.1.1.2. Results of uncertainty analysis of Sysser 47 at upright condition and $Fn = 0.6$.

	$C_t \times 1000$	R_t	Fx_p	Fx_f
p	2.920	2.540	0.391	2.330
P (p/p_{th})	1.460	1.270	0.196	1.165
δ_{RE}	-5.39E-02	-1.84E-01	-4.64E-05	-1.97E-06
δ_{RE}^{02}	-1.19E-01	-2.98E-01	-4.71E-06	-2.66E-06
δ_{RE}^{12}	4.91E-02	-9.79E-02	-1.82E-05	-6.18E-07
$\delta_{\Delta M}$	3.70E-01	9.48E-01	1.55E-05	7.80E-06
U_{SD}	2.22E-02	8.57E-02	1.49E-06	2.73E-07
U_{SD}^{02}	2.72E-02	8.86E-02	1.88E-06	3.07E-07
U_{SD}^{12}	2.35E-02	8.71E-02	1.52E-06	2.68E-07
U_{SN}	3.85E-01	9.83E-01	5.63E-05	8.28E-06
S₁	12.57	31.819	6.622E-04	2.405E-04
$U_{SN}\%S_1$	3.06	3.09	8.50	3.44

Table 4.1.1.3. Results of comparison between different densities of grid of Sysser 47 at upright condition and $Fn = 0.6$.

Grid	Number of cells [10 ⁶]	CPU time [h]	Uncertainty [%]
G5	0.90	176	11.96
G4	1.48	288	8.37
G3	2.46	472	5.85
G2	4.08	784	4.33
G1	6.79	1238	3.06

4.1.2 Heeled condition

Table 4.1.2.1. Results from verification of Sysser 47 at heeled condition and $Fn = 0.35$.

Grid	Cf	Cp	Ct	Sw [m2]	Std (Cf)	Std (CpV)	Std (Ct)	CPU Time [h]	No of cells	Uncertainty [%]
G4	0.00348	0.00225	0.00573	0.64740	0.25%	1.56%	0.72%	564	2887280	25.80
G3	0.00355	0.00225	0.00579	0.64769	0.17%	0.31%	0.17%	730	3734016	21.62
G2	0.00356	0.00233	0.00589	0.64769	0.10%	0.59%	0.27%	920	4719520	18.10
G1	0.00360	0.00221	0.00581	0.64681	0.27%	0.46%	0.29%	1198	6130024	15.63

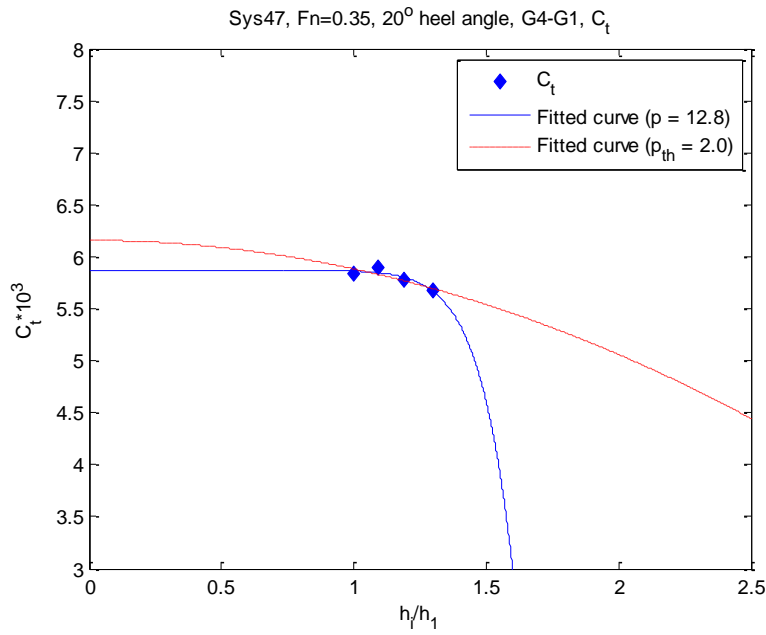


Figure 4.1.2.1. LSR curve fit

Table 4.1.2.2. Results of uncertainty analysis of Sysser 47 at heeled condition and $Fn = 0.35$.

	$C_t \times 1000$	R_t	Fx_p	Fx_f
p	12.800	14.100	14.900	10.700
P (p/p_{th})	6.400	7.050	7.450	5.350
δ_{RE}	-7.06E-03	-3.66E-03	-1.31E-07	-9.15E-07
δ_{RE}^{02}	-2.74E-01	-2.02E-01	-7.85E-06	-2.09E-05
δ_{RE}^{12}	4.65E+00	3.86E+00	3.35E-04	1.58E-04
$\delta_{\Delta M}$	7.67E-01	5.87E-01	4.00E-05	5.00E-05
U_{SD}	6.57E-02	5.20E-02	7.88E-06	1.32E-06
U_{SD}^{02}	9.05E-02	7.29E-02	8.46E-06	3.28E-06
U_{SD}^{12}	5.03E-02	3.81E-02	6.64E-06	1.80E-06
U_{SN}	9.11E-01	6.78E-01	3.20E-05	6.59E-05
S_1	5.83	4.413	2.490E-04	3.970E-04
$U_{SN}\%S_1$	15.63	15.37	12.85	16.61

Table 4.1.2.3. Results of comparison between different densities of grid of Sysser 47 at heeled condition and $Fn = 0.35$.

Grid	Number of cells [10 ⁶]	CPU time [h]	Uncertainty [%]
G4	2.89	564	25.80
G3	3.73	730	21.62
G2	4.72	920	18.10
G1	6.13	1198	15.63

4.1.3 Discussion

The uncertainty for the heeled case is rather big, largely because only four grids was used due to time limitations. When taking computational time and corresponding uncertainty into account, grid G3 is chosen for the upright condition and grid G2 is chosen for the heeled condition.

4.2 Validation

4.2.1 Upright condition

Table 4.2.1.1. Results from validation of Sysser 46 at upright condition.

Fn	Cf	Cp	Ct	Sw[m2]	Rt_shf[N]	Rt_mea[N]	Difference[%]
0.35	0.00361	0.00208	0.00569	0.76728	4.482	4.705	-4.74
0.4	0.00350	0.00474	0.00823	0.79214	8.735	8.777	-0.48
0.5	0.00338	0.01043	0.01381	0.81933	23.672	24.925	-5.03
0.6	0.00329	0.01137	0.01466	0.82811	36.592	36.638	-0.13
0.7	0.00318	0.00848	0.01166	0.86261	41.278	43.887	-5.94

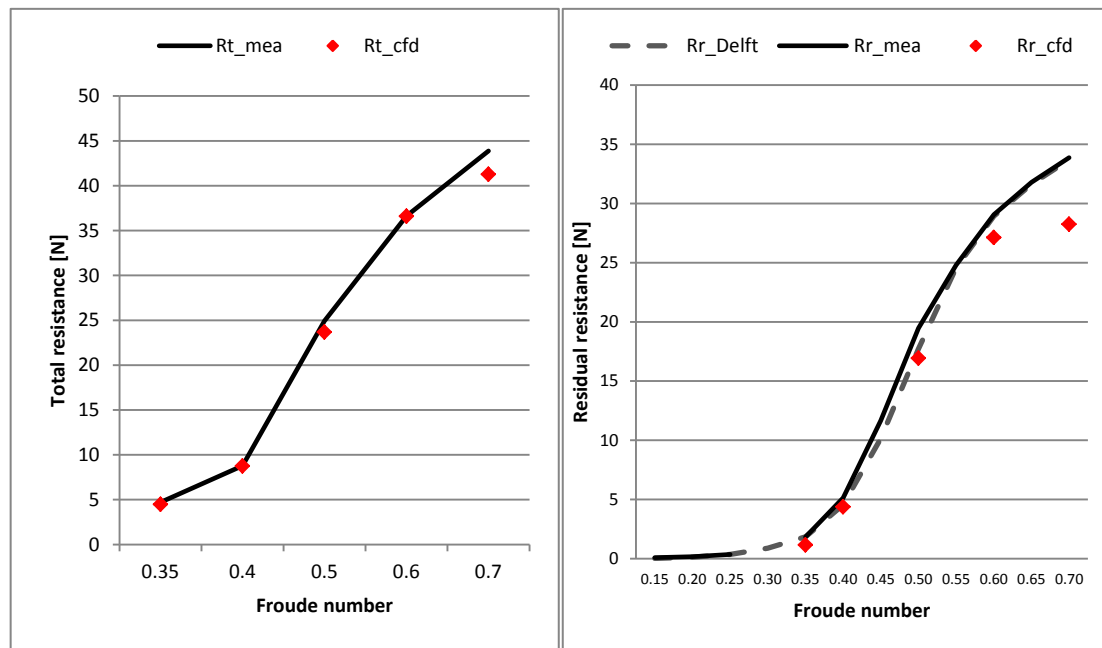


Figure 4.2.1.1. Comparison of the total resistance (left) and the residual resistance (right) between measured results (black line), calculated results from the Delft formulas (dashed line), and computed CFD results for varying Froude number of Sysser 46.

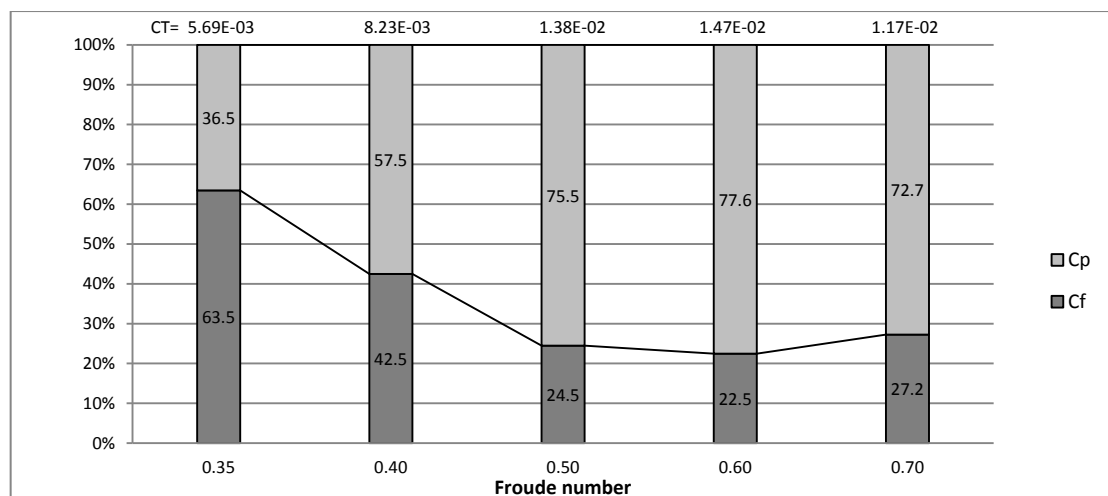


Figure 4.2.1.2. Illustration of the varying influence of frictional and pressure resistance components on the total resistance for increasing Froude number of Sysser 46.

Table 4.2.1.2. Results from validation of Sysser 47 at upright condition.

Fn	Cf	Cp	Ct	Sw[m2]	Rt_shf[N]	Rt_mea[N]	Difference[%]
0.3	0.00371	0.00109	0.00480	0.76670	2.776	2.981	-6.88
0.4	0.00354	0.00393	0.00746	0.81085	8.003	7.725	3.60
0.5	0.00344	0.00824	0.01168	0.80939	19.772	22.302	-11.35
0.6	0.00332	0.00836	0.01168	0.80881	28.465	33.496	-15.02
0.7	0.00319	0.00691	0.01009	0.82109	33.989	40.730	-16.55

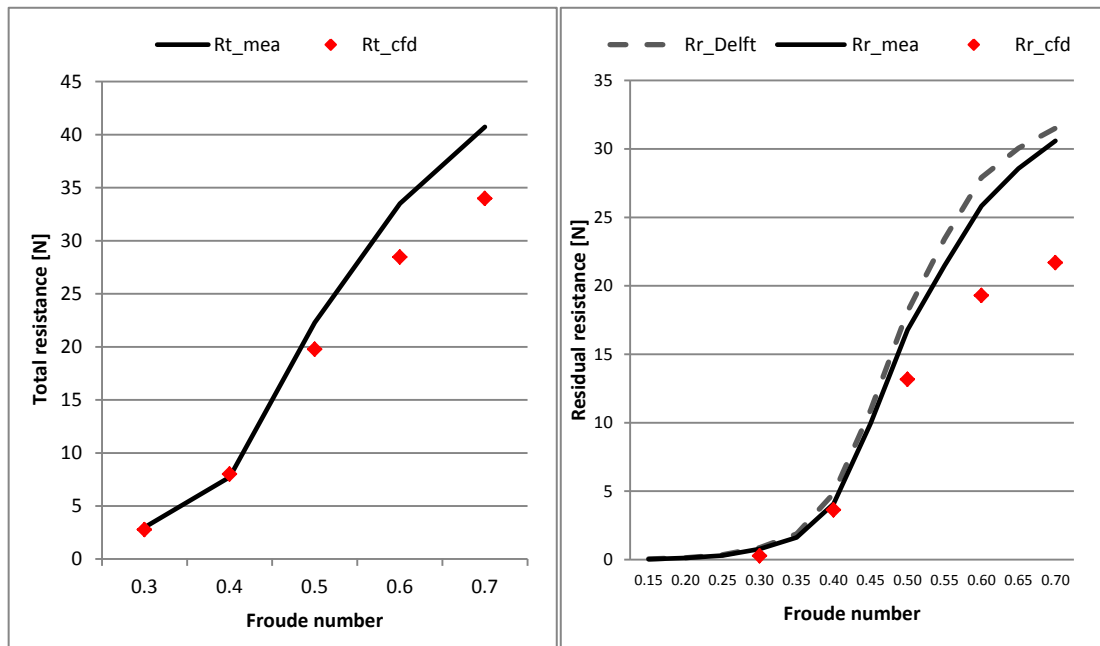


Figure 4.2.1.3. Comparison of the total resistance (left) and the residual resistance (right) between measured results (black line), calculated results from the Delft formulas (dashed line), and computed CFD results for varying Froude number of Sysser 47.

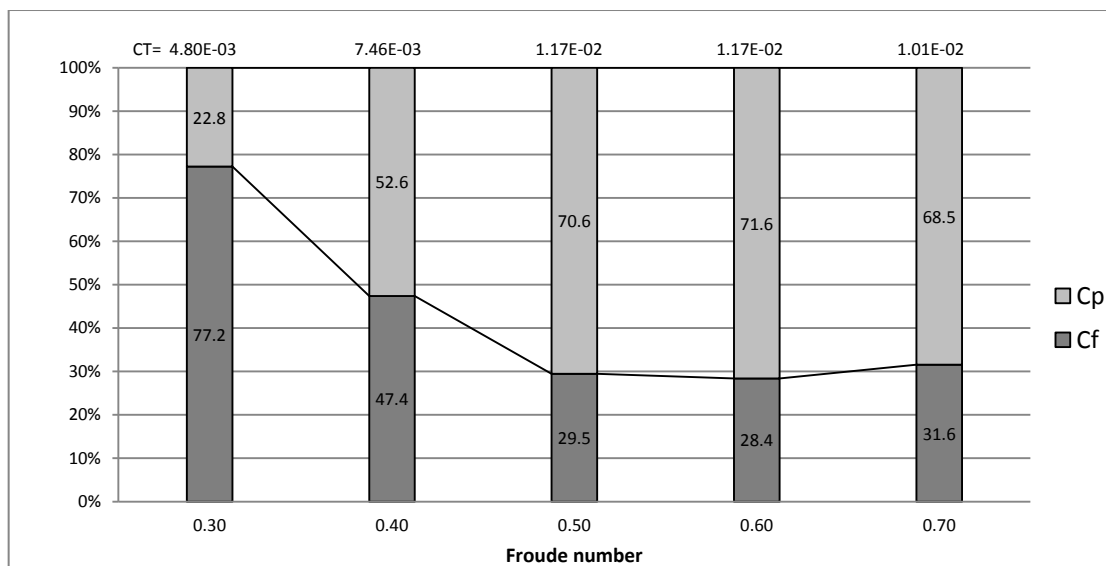


Figure 4.2.1.4. Illustration of the varying influence of frictional and pressure resistance components on the total resistance for increasing Froude number of Sysser 47.

Table 4.2.1.3. Results from validation of Sysser 50 at upright condition.

Fn	Cf	Cp	Ct	Sw[m2]	Rt_shf[N]	Rt_mea[N]	Difference[%]
0.3	0.00357	0.00095	0.00452	1.02280	4.075	4.696	-13.23
0.4	0.00347	0.00420	0.00767	1.06720	12.793	13.062	-2.06
0.5	0.00337	0.01001	0.01338	1.08040	35.559	37.323	-4.73
0.6	0.00322	0.01076	0.01398	1.07680	53.123	56.902	-6.64
0.7	0.00309	0.00783	0.01093	1.10840	58.086	67.686	-14.18

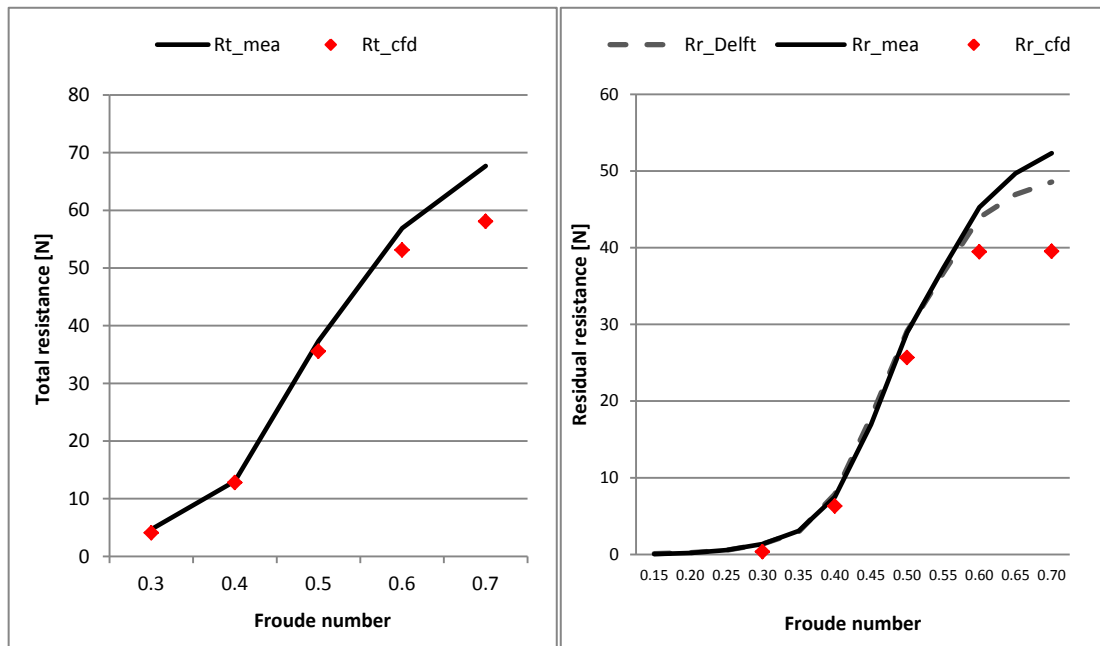


Figure 4.2.1.5. Comparison of the total resistance (left) and the residual resistance (right) between measured results (black line), calculated results from the Delft formulas (dashed line), and computed CFD results for varying Froude number of Sysser 50.

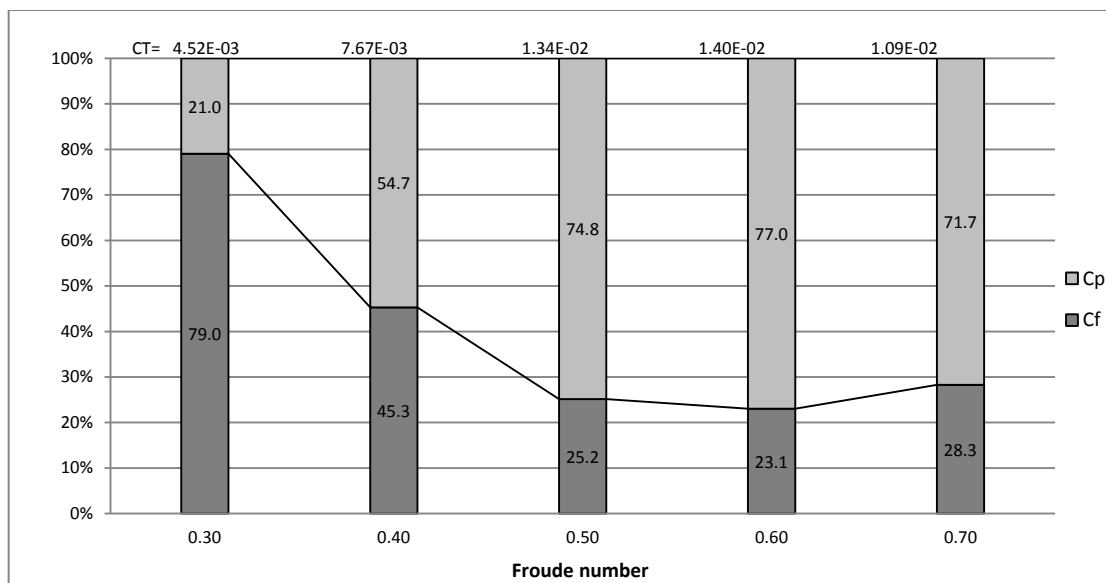


Figure 4.2.1.6. Illustration of the varying influence of frictional and pressure resistance components on the total resistance for increasing Froude number of Sysser 50.

4.2.2 Heeled condition

Table 4.2.2.1. Results from validation of Sysser 47 at heeled condition.

Fn	Cf	Cp	Ct	Sw [m2]	Rt_shf [N]	Rt_mea [N]	Difference [%]
0.25	0.00377	0.00057	0.00434	0.71242	1.613	1.786	-9.69
0.30	0.00368	0.00136	0.00504	0.72774	2.765	2.890	-4.32
0.35	0.00353	0.00226	0.00579	0.73907	4.393	4.272	2.83
0.40	0.00340	0.00465	0.00805	0.77004	8.199	7.298	12.35
0.45	0.00337	0.00766	0.01103	0.76405	14.287	13.838	3.25

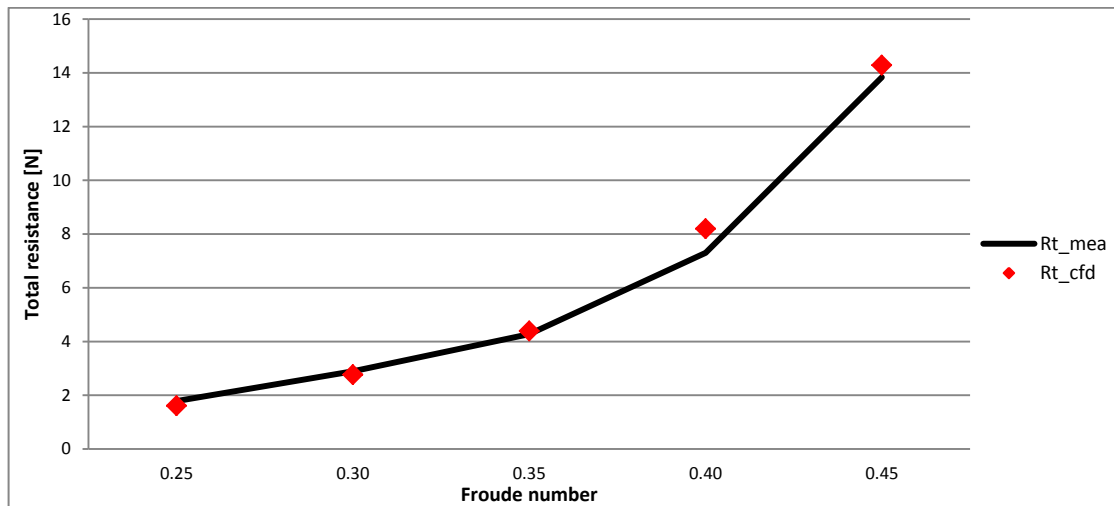


Figure 4.2.2.1. Comparison between measured results and computed CFD results for varying Froude number of Sysser 47 in heeled condition.

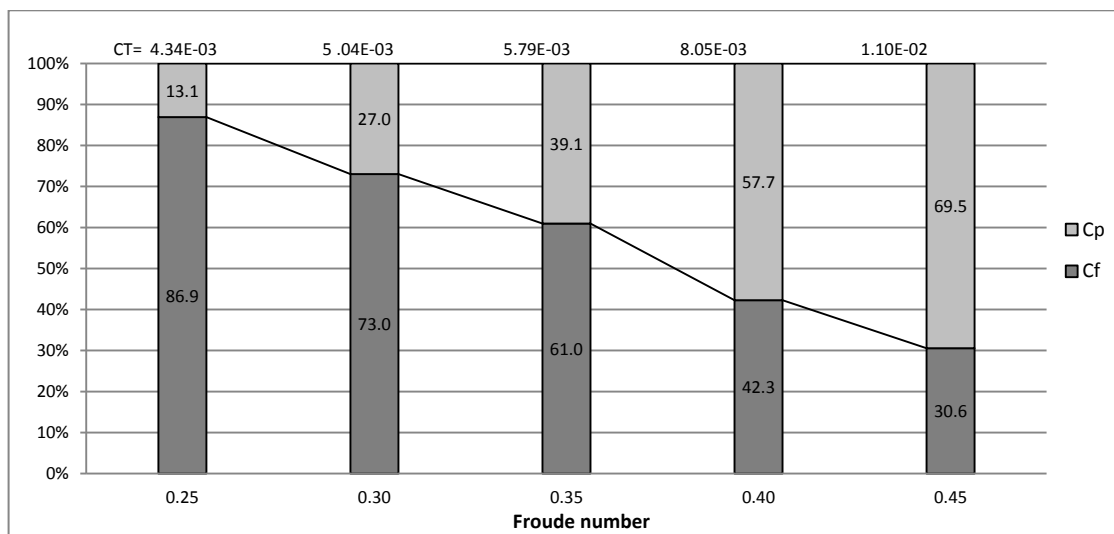


Figure 4.2.2.2. Illustration of the varying influence of frictional and pressure resistance components on the total resistance for increasing Froude number of Sysser 47 in heeled condition.

Table 4.2.2.2. Results from validation of Sysser 48 at heeled condition.

Fn	Cf	Cp	Ct	Sw [m ²]	Rt_shf [N]	Rt_mea [N]	Difference [%]
0.25	0.00382	0.00087	0.00469	0.68777	1.686	1.899	-11.22
0.30	0.00359	0.00197	0.00557	0.70443	2.955	3.127	-5.49
0.35	0.00348	0.00346	0.00694	0.72874	5.191	4.989	4.05
0.40	0.00334	0.00644	0.00977	0.75605	9.896	9.382	5.47
0.45	0.00327	0.00975	0.01307	0.77037	17.070	17.098	-0.16

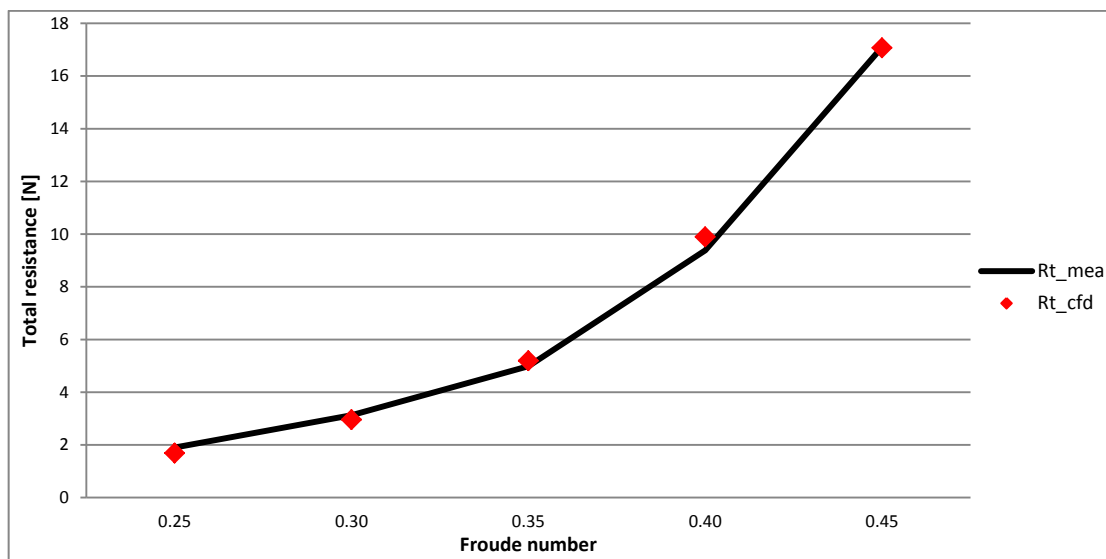


Figure 4.2.2.3. Comparison between measured results and computed CFD results for varying Froude number of Sysser 48 in heeled condition.

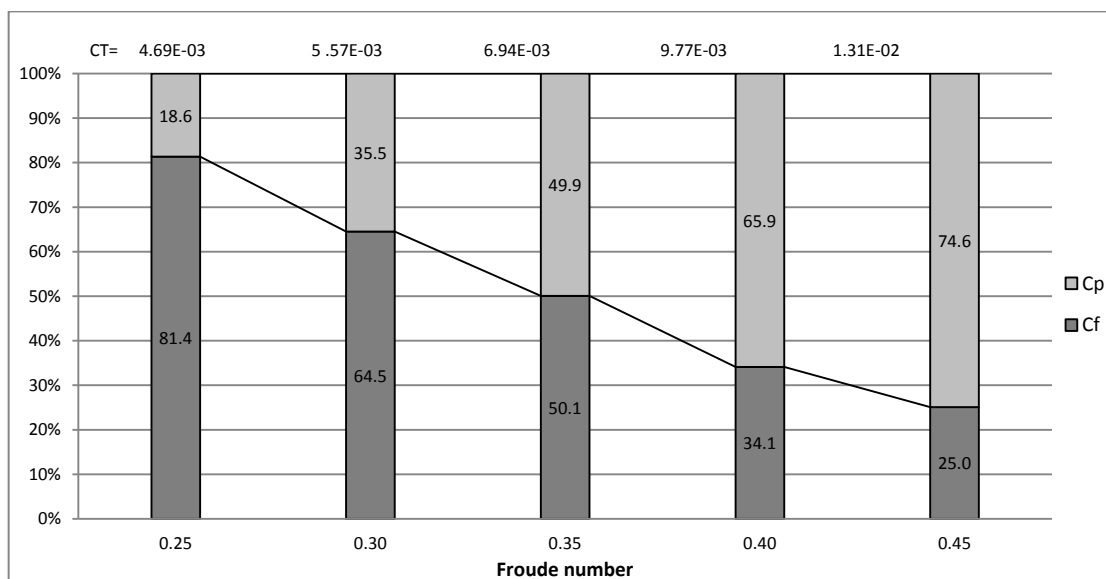


Figure 4.2.2.4. Illustration of the varying influence of frictional and pressure resistance components on the total resistance for increasing Froude number of Sysser 48 in heeled condition.

4.2.3 Discussion

The plots below shows the predicted results from the CFD computations compared to the towing tank experimental results, at Froude numbers 0.4 and 0.6 in upright condition and at Froude number 0.35 in heeled condition. To be able to trust the solver in the optimization phase, it is important that the difference in resistance between the hulls is reflected on the results.

Considering the plots, it is clear that the solver gives satisfactory results at low and medium Froude numbers, but there is an under prediction for high Froude numbers. For the high Froude numbers where the accuracy is less good, the error is fairly consistent and is under predicting equally for four out of five cases. The differences are however well predicted and thus the solver can be trusted to produce credible results for the optimization phase.

For the heeled case validation on some more hulls would have been desirable, but due to time limitations this could not be done. The results from the two hulls are however very satisfactory.

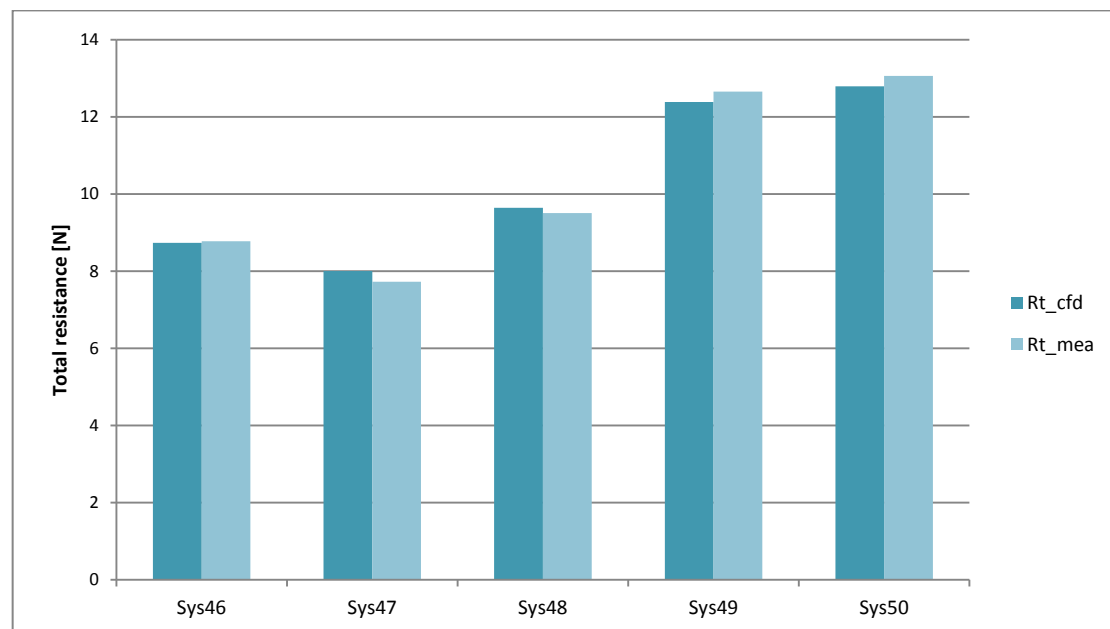


Table 4.3.3.1. Validation results comparison for Froude number 0.4 and upright condition.

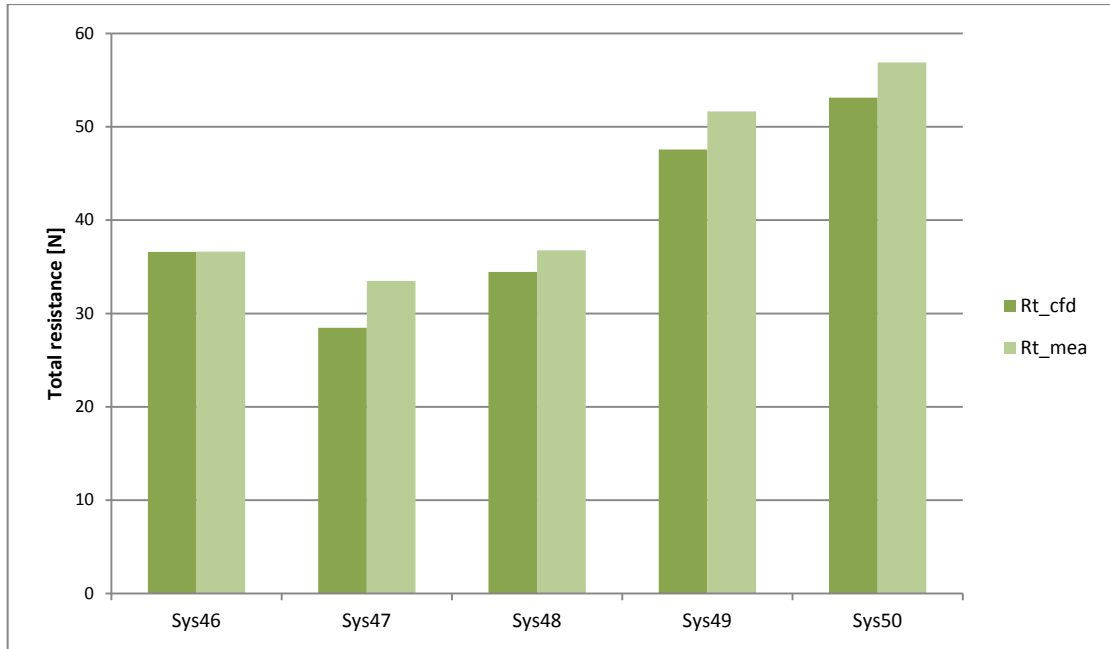


Table 4.3.3.2. Validation results comparison for Froude number 0.6 and upright condition.

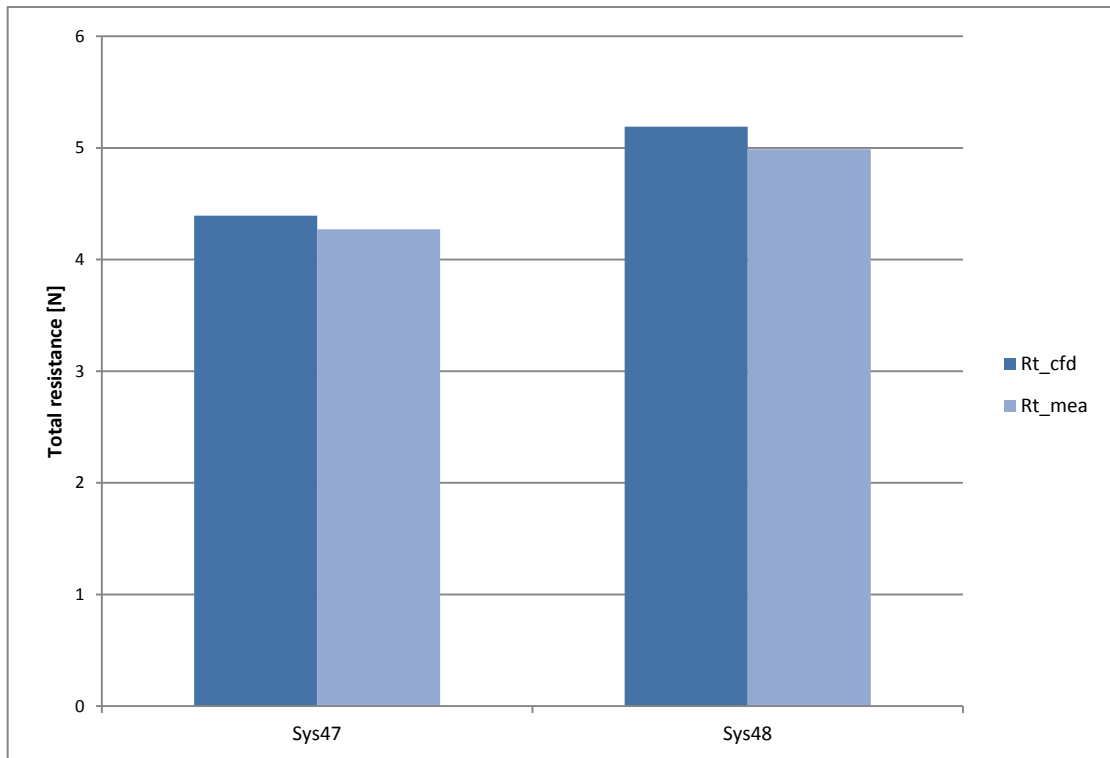


Table 4.3.3.3. Validation results comparison for Froude number 0.35 and heeled condition.

4.3 Optimization

The results for the intermediately rounded transom hulls are not presented in the report. Some of the results from these calculations could not be explained and did not follow the rather stable trends of the other transom shapes. Unfortunately, there was not enough time to further investigate the reasons for this. Since these results do not significantly contribute to the conclusions the decision was taken to leave these results out of the report.

Figure 4.3.1 and 4.3.2 shows summaries of the performance of the hulls in upright and heeled condition. The waterlines at the transom are presented at the different Froude numbers, and the total resistance of the hulls are compared to the baseline hulls in upright and 20° heeled condition.

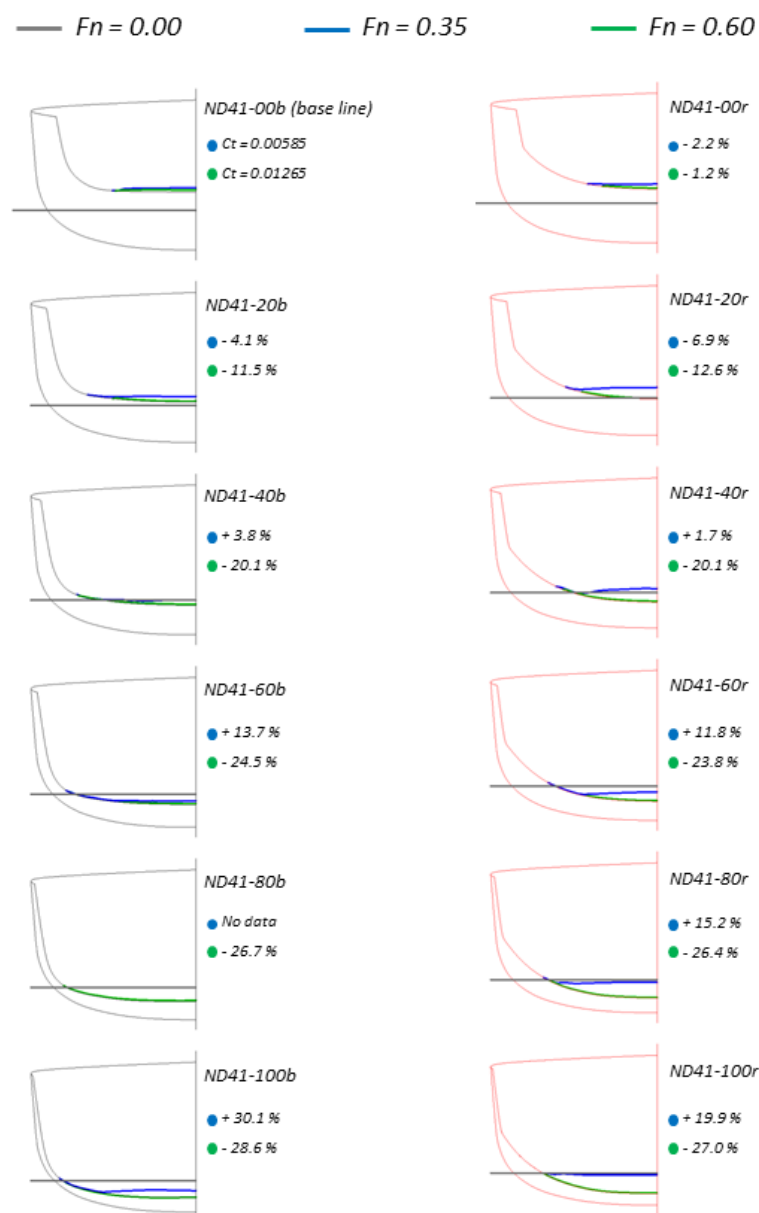


Figure 4.3.1. Differences in resistance between the hulls in upright condition at both Froude numbers. The transom waterlines at Froude numbers 0, 0.35 and 0.6 are also indicated in the figure.

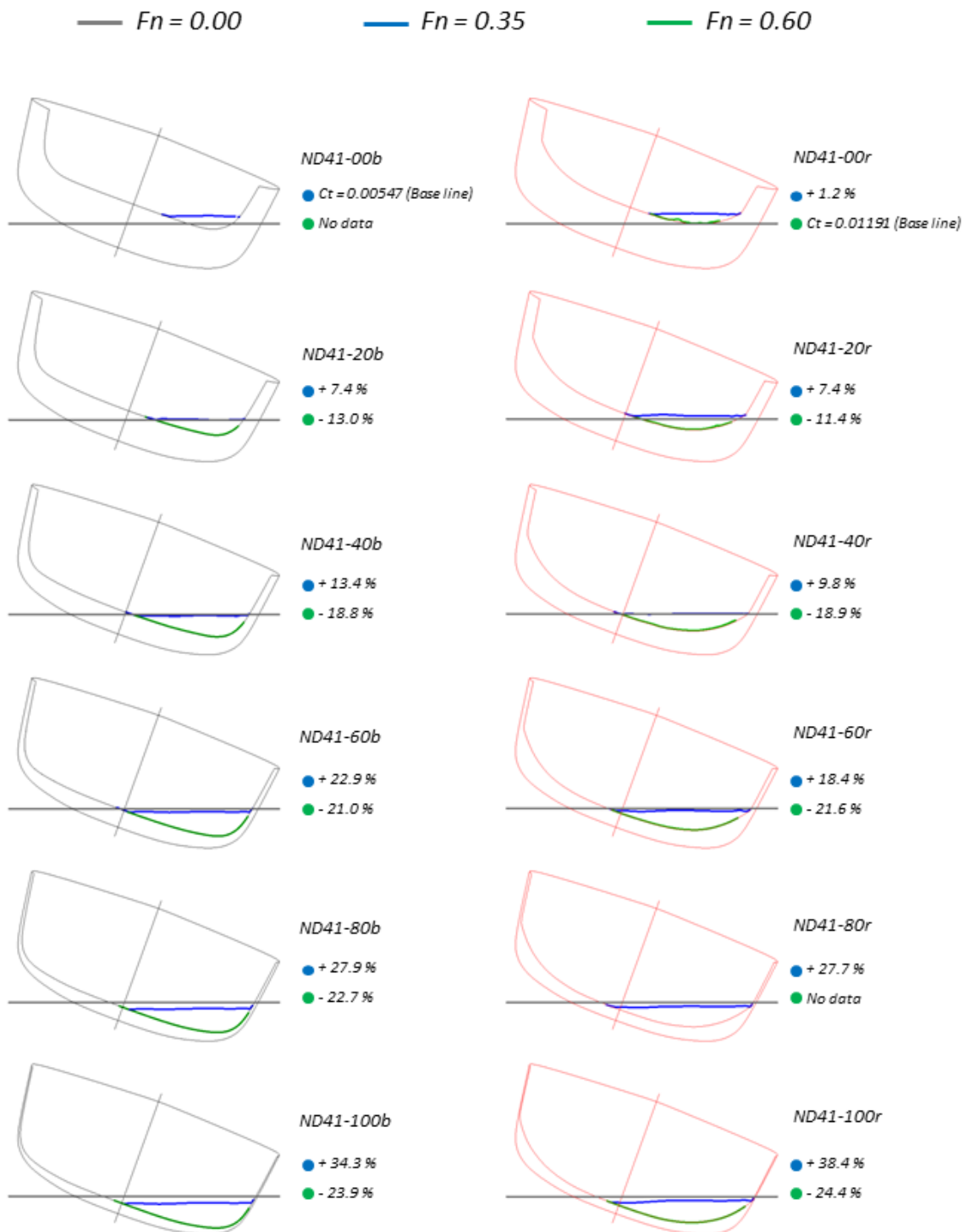


Figure 4.3.2. Differences in resistance between the hulls in heeled condition at both Froude numbers. The transom waterlines at Froude numbers 0, 0.35 and 0.6 are also indicated in the figure.

4.3.1 Upright at Froude number 0.35

4.3.1.1 Results

In Table 4.3.1.1.1. the resistance coefficients from the potential flow (XPAN) and RANS flow (XCHAP) computations are presented. As seen in Figure 4.3.1.1.1, there is quite good compliance between the models, but the prediction for which transom shape that is most beneficial is switched for the XPAN results. In the same figure C_t is plotted against; L_{cb} , transom immersion and immersed transom area. Since not all transom sizes are immersed at zero speed, there are no data points for these hulls in the plots. Figure 4.3.1.1.2 shows a wave patterns comparison between the round and boxy transoms with varying transom size. Finally Figure 4.3.1.1.3 illustrates the wave profile of the stern wave at the centre plane. The profiles are shown with varying transom shape for all transom sizes.

Table 4.3.1.1.1. XCHAP and XPAN results for ND41 variations at upright condition and $Fn = 0.35$.

Hull	XPAN (+XBOUND)				XCHAP			
	Sw [m2]	Cw	Cf	Ct	Sw [m2]	Cf	Cp	Ct
ND41-00b	No data				0.79384	0.00367	0.00218	0.00585
ND41-20b	0.76978	0.00168	0.00396	0.00564	0.80955	0.00367	0.00182	0.00560
ND41-40b	0.76800	0.00191	0.00392	0.00582	0.81408	0.00370	0.00222	0.00607
ND41-60b	0.77523	0.00250	0.00390	0.00644	0.81653	0.00373	0.00273	0.00665
ND41-80b	0.77651	0.00313	0.00387	0.00706	No data			
ND41-100b	0.77527	0.00369	0.00385	0.00759	0.81862	0.00372	0.00366	0.00761
ND41-00r	0.74280	0.00238	0.00402	0.00618	0.78198	0.00368	0.00213	0.00572
ND41-20r	0.75042	0.00198	0.00398	0.00581	0.79245	0.00363	0.00182	0.00544
ND41-40r	0.74930	0.00241	0.00394	0.00618	0.79943	0.00366	0.00224	0.00594
ND41-60r	0.75621	0.00298	0.00390	0.00676	0.80187	0.00369	0.00278	0.00654
ND41-80r	0.75654	0.00350	0.00388	0.00725	0.80641	0.00368	0.00295	0.00673
ND41-100r	0.77527	0.00369	0.00388	0.00762	0.80990	0.00368	0.00320	0.00701

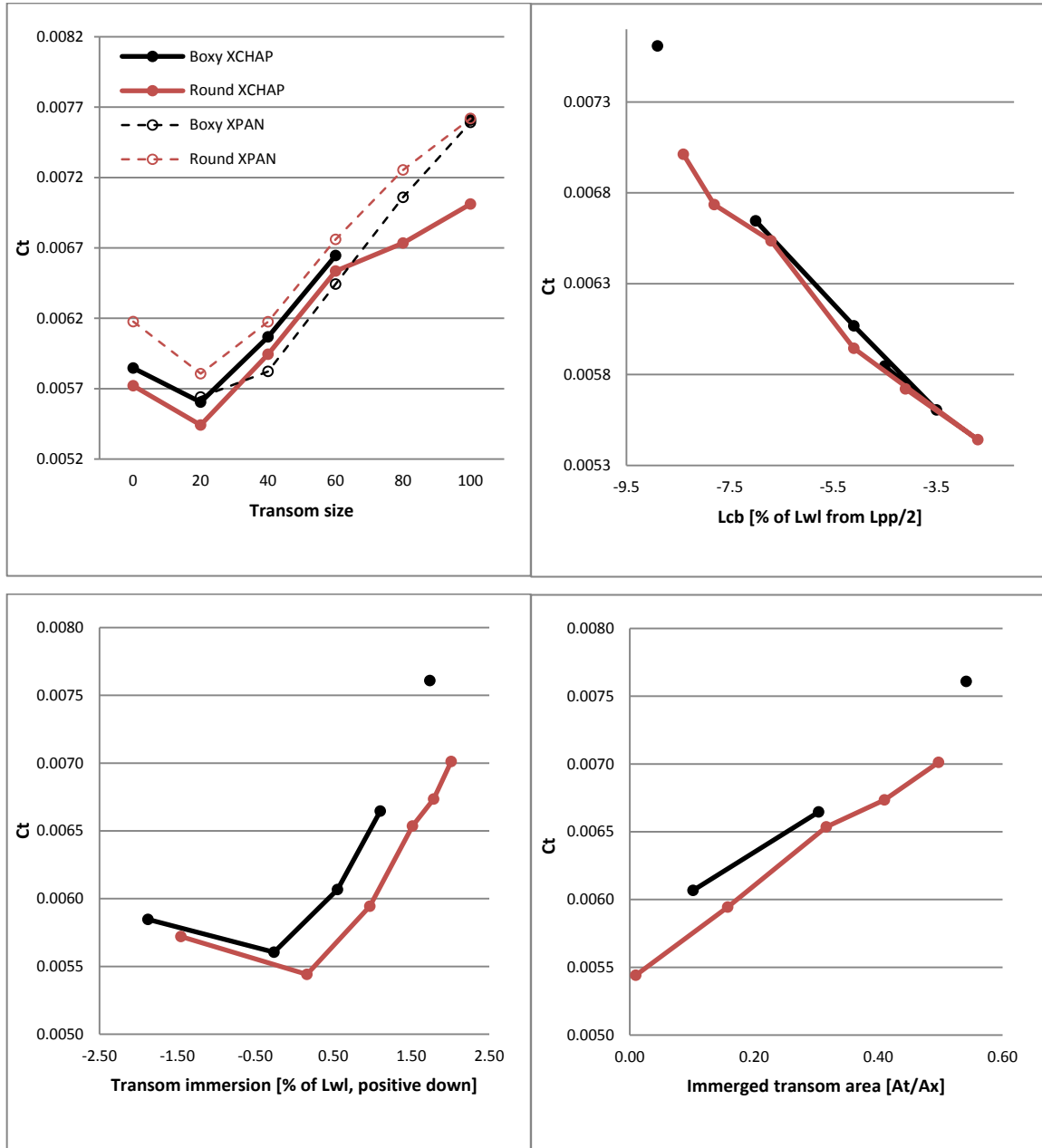
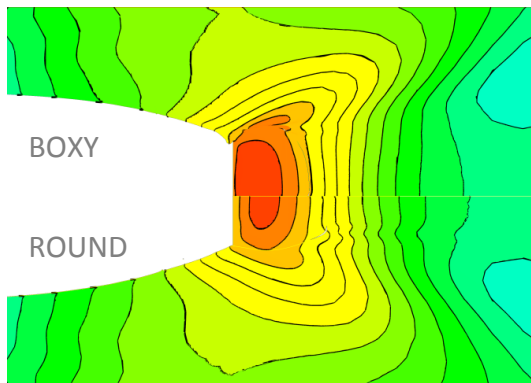
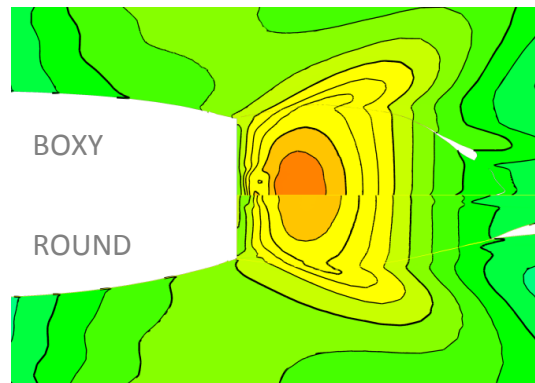


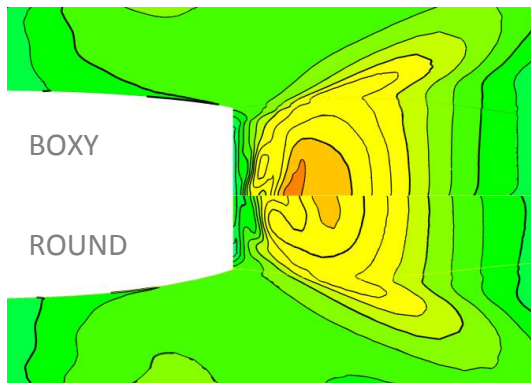
Figure 4.3.1.1.1. C_t plotted against (clockwise, starting top left) Transom size, L_{cb} , Transom immersion and Immersed transom area. Black lines corresponds to boxy transom and red lines corresponds to round transom. Dashed lines are XPAN results.



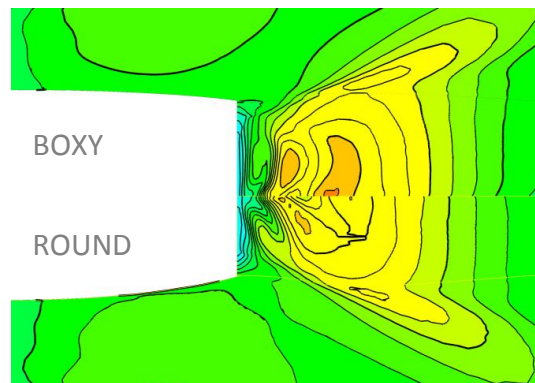
ND41-00



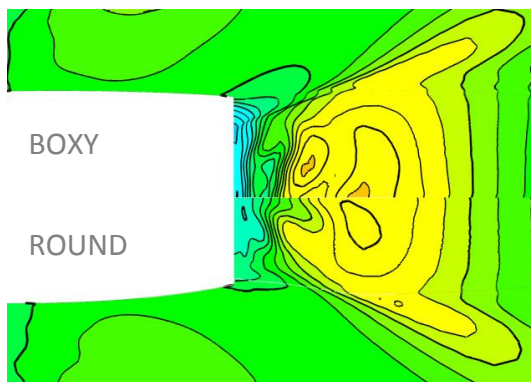
ND41-20



ND41-40



ND41-60



ND41-100

Figure 4.3.1.1.2. Wave pattern comparisons between boxy transoms (top half of pictures) and round transoms (bottom half) with increasing transom size at Froude number 0.35.

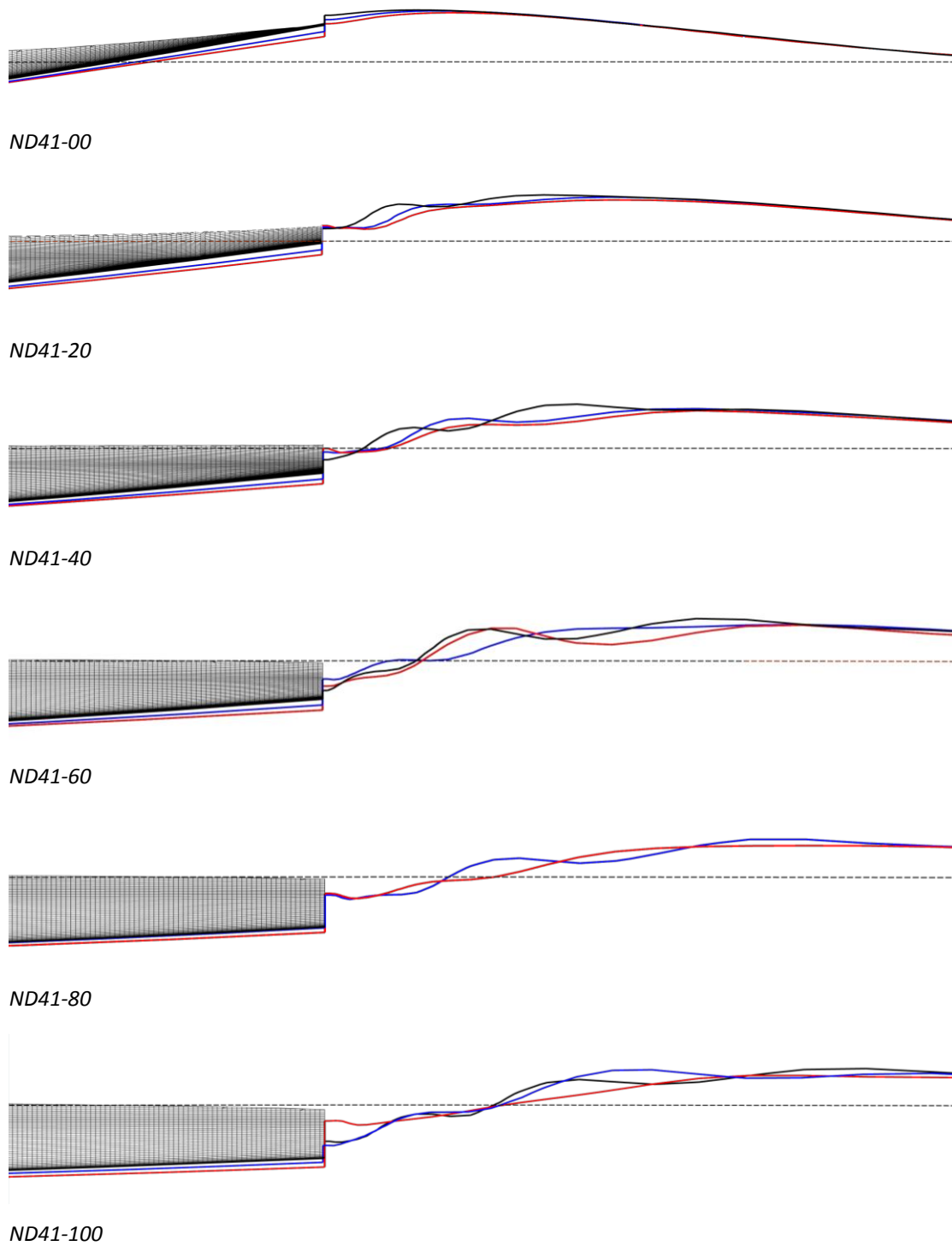


Figure 4.3.1.1.3. Wave profile plots at the stern along the center plane of the ND41 with varying transom size. Black line corresponds to boxy transom, blue line to intermediate, and red line corresponds to round transom. Dashed line is the undisturbed free water surface.

4.3.1.2 Discussion

In this condition the transom is wetted for all hulls, even for the 00 hulls with such large overhang (see Figure 4.1). The wave patterns (Figure 4.3.1.1.2) show that the bow wave decreases with growing transom size. Same tendency is seen for the stern wave system of hulls 00-20-40. From the 60 hulls and upwards the trend is less clear, their stern waves seem rather equal. So, from just looking at the wave patterns and wave profiles, one could expect that the hulls with larger transoms should have less total resistance.

This is, however, not the case. Instead the total resistance has a minimum for the 20 hulls. The explanation to this is likely to be a rapid growth of the viscous pressure resistance for larger transoms. It is caused by separation of the viscous boundary layer at the transom. In the car and aero industry this is known as base drag and occurs in the wake after a blunt cut off geometry. The ratio of area of this blunt cut off edge compared to the maximum cross section area of the body has great impact on the base drag, Hoerner (1965). For high ratios the base drag is dramatically increased, and this is likely to be the case for the hulls with big immersed transom area (see Figure 4.3.1.2.1).

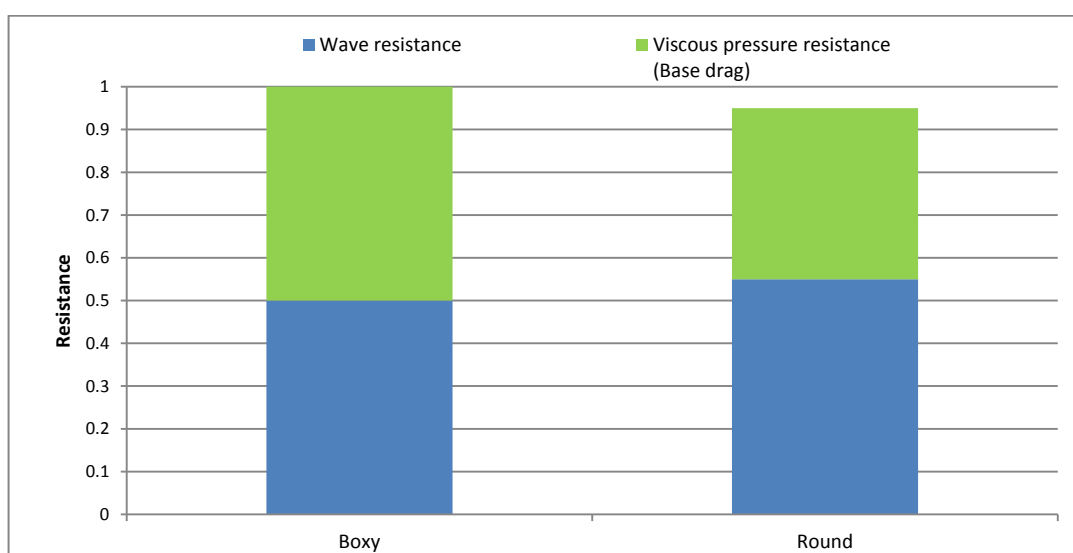


Figure 4.3.1.2.1. Schematic diagram of what the relation between base drag and wave resistance looks like. Note that the split is schematic; it has not been computed.

Thus there are two large resistance components that seem to have different optima. The wave resistance that has a minimum amongst the hulls with bigger transoms, and the viscous pressure resistance, the base drag, that has a minimum for the transom with smallest wetted transom area. The combined optimum of the two components is the 20 hulls.

Worth noticing is that the round transom is a lot better than the boxy one for the large transom sizes. The same tendency is seen for the smaller transoms but it is much less significant. The stern wave patterns are smaller for the round transoms, and it is probably explained by the smaller buttock angle.

4.3.2 Upright at Froude number 0.60

4.3.2.1 Results

In Table 4.3.2.1.1. the resistance coefficients from the potential flow (XPAN) and RANS flow (XCHAP) computations are presented. As seen in Figure 4.3.2.1.1, the compliance between the models is less good at this Froude number when compared to the lower one. In the same figure C_t is plotted against; L_{cb} , transom immersion and immersed transom area. Since not all transom sizes are immersed at zero speed, there are no data points for these hulls in the plots. Figure 4.3.2.1.2 shows a wave patterns comparison between the round and boxy transoms with varying transom size. Finally Figure 4.3.2.1.3 illustrates the wave profile of the stern wave at the centre plane. The profiles are shown with varying transom shape for all transom sizes.

Table 4.3.2.1.1. XCHAP and XPAN results for ND41 variations at upright condition and $Fn = 0.60$.

Hull	XPAN (+XBOUND)				XCHAP			
	Sw [m2]	Cw	Cf	Ct	Sw [m2]	Cf	Cp	Ct
ND41-00b	No data				0.81094	0.00322	0.00944	0.01265
ND41-20b	0.76976	0.00617	0.00376	0.00994	0.82909	0.00322	0.00773	0.01119
ND41-40b	No data				0.84095	0.00323	0.00652	0.01011
ND41-60b	0.77521	0.00495	0.00319	0.00821	0.84723	0.00324	0.00590	0.00955
ND41-80b	0.77649	0.00473	0.00293	0.00773	0.85037	0.00325	0.00560	0.00928
ND41-100b	0.77525	0.00459	0.00290	0.00754	0.85037	0.00325	0.00537	0.00903
ND41-00r	No data				0.80850	0.00322	0.00931	0.01249
ND41-20r	0.75043	0.00632	0.00374	0.00980	0.81827	0.00322	0.00774	0.01106
ND41-40r	0.74930	0.00556	0.00363	0.00895	0.82595	0.00323	0.00669	0.01010
ND41-60r	0.75620	0.00519	0.00329	0.00833	0.82944	0.00324	0.00619	0.00964
ND41-80r	0.75653	0.00501	0.00347	0.00833	0.82874	0.00325	0.00586	0.00931
ND41-100r	0.75740	0.00511	0.00297	0.00795	0.83048	0.00326	0.00576	0.00924

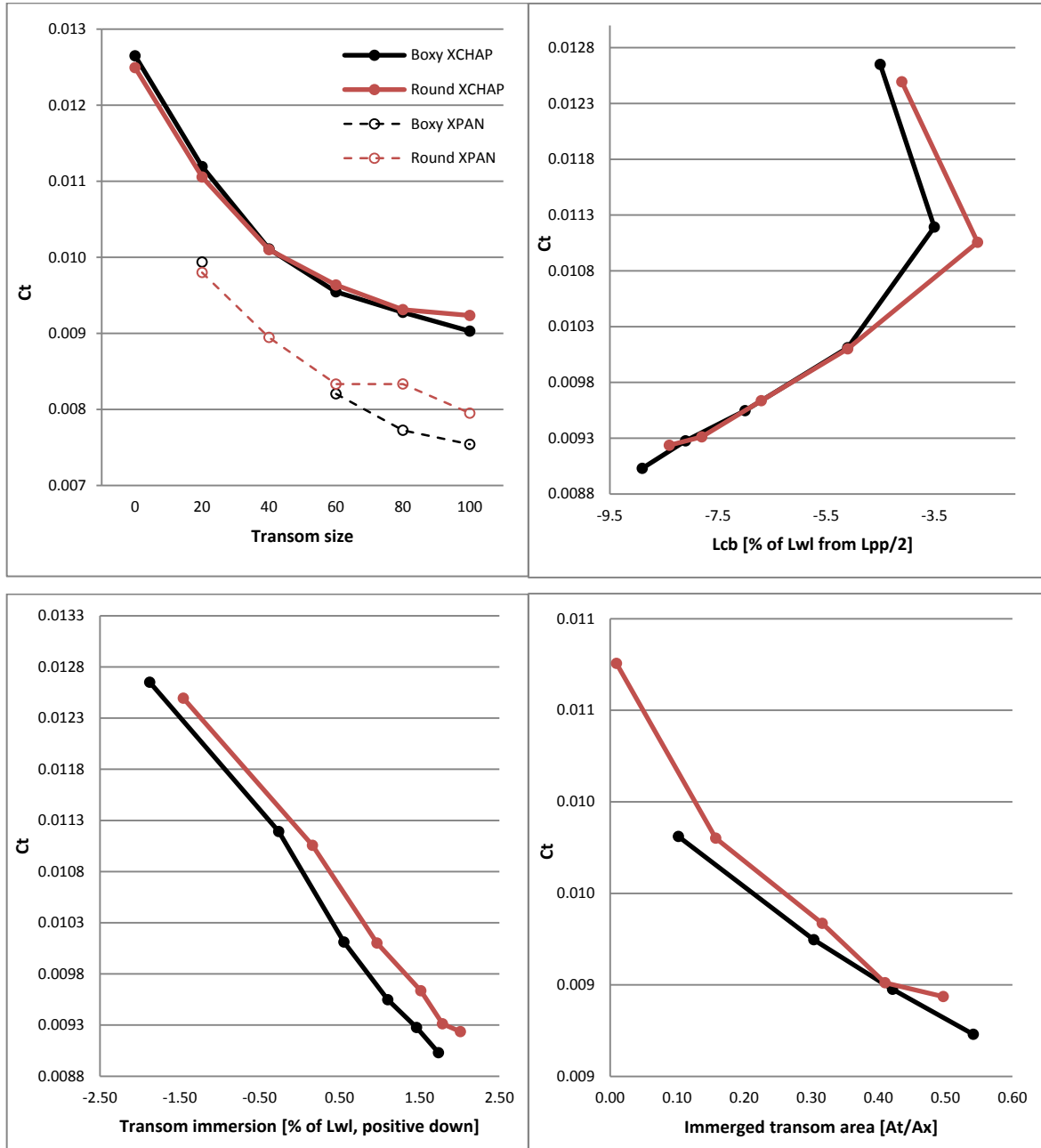


Figure 4.3.2.1.1. C_t plotted against (clockwise, starting top left) Transom size, Lcb, Transom immersion and Immersed transom area. Black lines corresponds to boxy transom and red lines corresponds to round transom. Dasched lines are XPAN results.

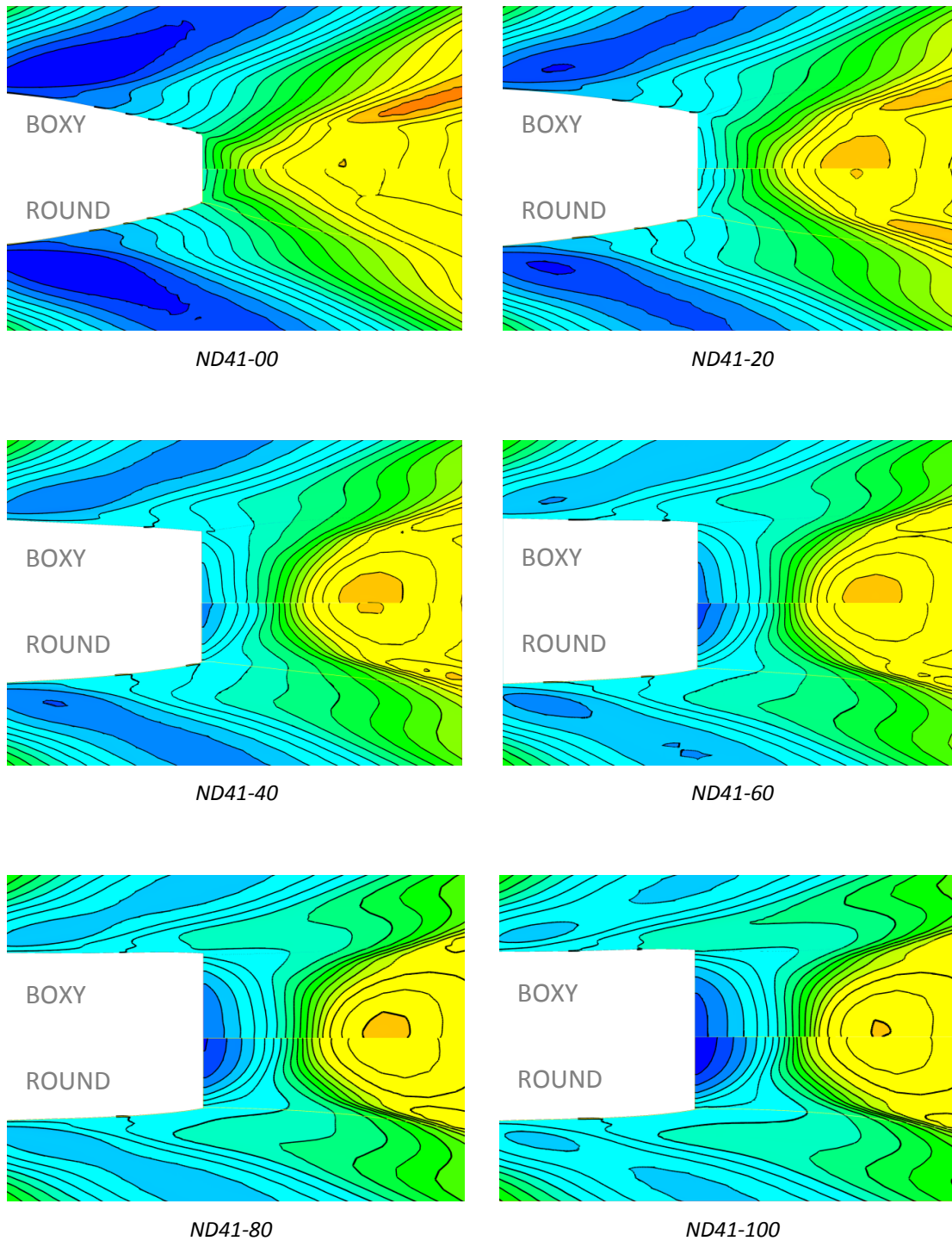


Figure 4.3.2.1.2. Wave pattern comparisons between boxy transoms (top half of pictures) and round transoms (bottom half) with increasing transom size at Froude number 0.35.

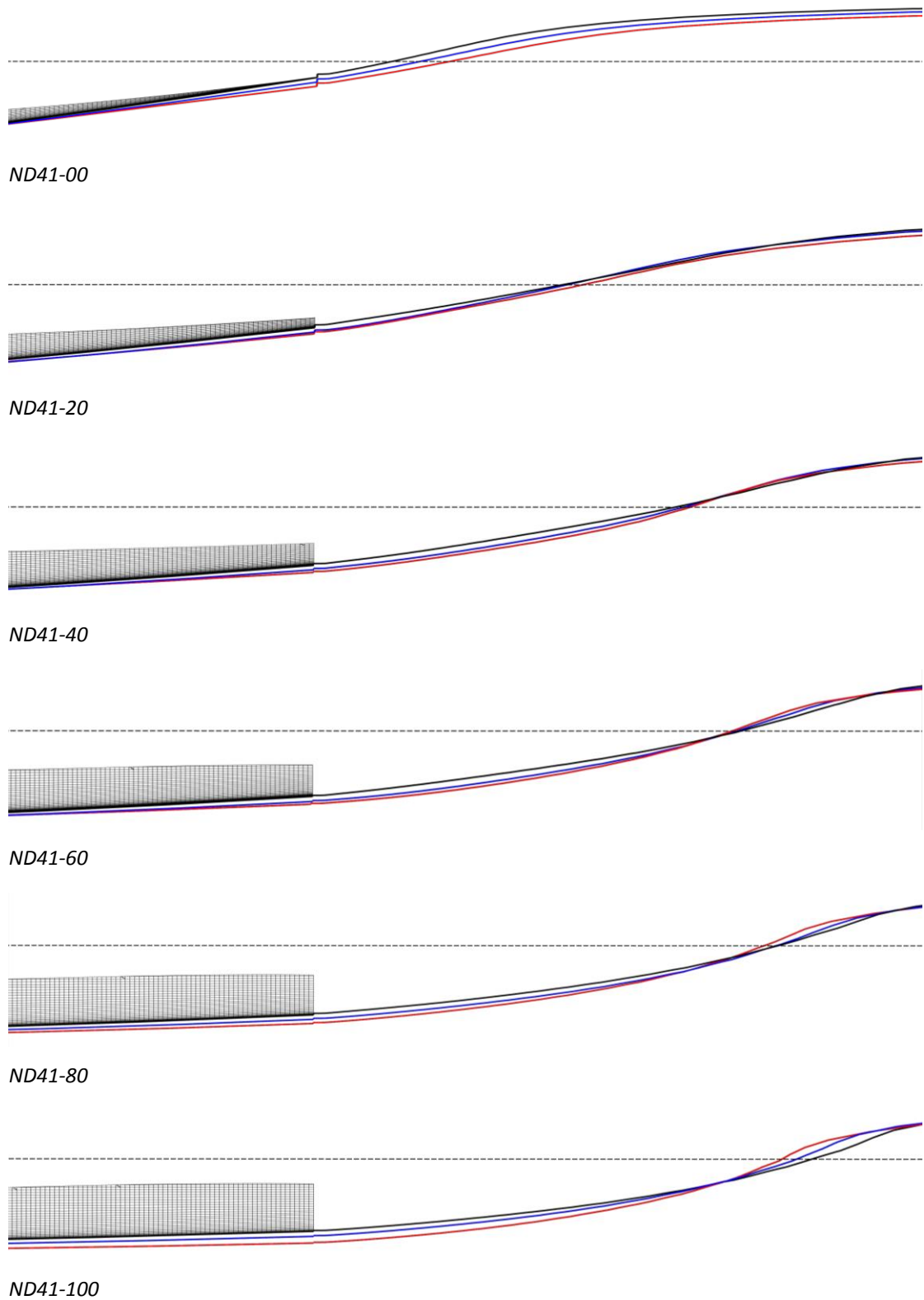


Figure 4.3.2.1.3. Wave profile plots at the stern along the center plane of the ND41 with varying transom size. Black line corresponds to boxy transom, blue line to intermediate, and red line corresponds to round transom. Dashed line is the undisturbed free water surface.

4.3.2.2 Discussion

At this Froude number no optimum in transom size is found, although the total resistance curve seems to be converging near the largest transoms. In contrast to the upright Froude number 0.35 condition, all transoms are now cleared. The base drag is thus replaced by the transom resistance. It increases with the immersed transom area, but decreases with the Froude number squared. At this rather high Froude number the upsides of larger transom (straighter waterline, smaller buttock angle) weighs heavier than the downside from increased transom drag (more on this in Chapter 4.3.6).

The fact that no optimum transom immersion is found despite very large A_t/A_x ratio is rather unexpected. Larsson & Raven (2010) proposes a maximum ratio of 0.18 at Froude number 0.60, while the ratio for the fastest hull at the same speed is as much as 0.67. But this ratio from Larsson and Raven is not intended for sailing yachts. It is thereby not applicable without some rethinking, since the trimming moment from the sails in reality trims the yacht bow down and thus the immersed transom area, which is measured at zero speed, is significantly reduced when sailing.

The boxy transom has a slight edge over the round one. The bow wave system is slightly smaller for the boxy transom thanks to the straighter waterlines. This is seen at the wave trough near the stern. At this Froude number the bow wave system seems to have more influence on resistance than the stern wave system, since the stern wave actually is smaller for the round transom (due to smaller buttock angle). The transverse wave is dampened rather quickly by the solver so the impact of the buttock angle and thereby the stern wave system at this speed may be questioned.

One should mention that the differences here are rather small, and that the boxy transom may benefit from a more box shaped mid-section. A hull originally designed for a round transom would be likely to have straighter waterlines near the stern and thus the differences may have been even less.

4.3.3 Heeled 20° at Froude number 0.35

4.3.3.1 Results

In Table 4.3.3.1.1 the resistance coefficients from the potential flow (XPAN) and RANS flow (XCHAP) computations are presented. XBOUND was not used for any heeled cases and thus no frictional resistance is computed in the potential flow model. In Figure 4.3.3.1.1 C_t from XCHAP is plotted against transom size for boxy and round transoms. In Figures 4.3.3.1.2 and 4.3.3.1.3 C_t is plotted against transom immersion and immersed transom area with hydrostatic data from both upright and heeled condition. Since not all transom sizes are immersed at zero speed, there are no data points for these hulls in the plots. Figure 4.3.3.1.4 is a plot of C_t against L_{cb} . Figure 4.3.3.1.5 is a comparison between the wave patterns with varying transom shape and size.

Table 4.3.3.1.1. XCHAP and XPAN results for ND41 variations at heeled condition and $Fn = 0.35$.

Hull	XPAN		XCHAP			
	C_w	C_t	S_w [m ²]	C_f	C_p	C_t
ND41-00b	0.00180	0.00180	0.68986	0.00360	0.00187	0.00547
ND41-20b	0.00221	0.00221	0.69230	0.00363	0.00223	0.00587
ND41-40b	0.00326	0.00326	0.69509	0.00361	0.00254	0.00619
ND41-60b	0.00446	0.00446	0.69719	0.00359	0.00306	0.00671
ND41-80b	0.00538	0.00538	0.69754	0.00357	0.00334	0.00699
ND41-100b	0.00618	0.00618	0.69788	0.00357	0.00368	0.00734
ND41-00r	0.00172	0.00172	0.69195	0.00358	0.00194	0.00553
ND41-20r	0.00181	0.00181	0.69893	0.00358	0.00221	0.00587
ND41-40r	0.00265	0.00265	0.69788	0.00360	0.00233	0.00600
ND41-60r	0.00363	0.00363	0.69893	0.00360	0.00279	0.00647
ND41-80r	0.00438	0.00438	0.69684	0.00362	0.00329	0.00698
ND41-100r	5.04E-03	0.00504	0.69788	0.00362	0.00386	0.00757

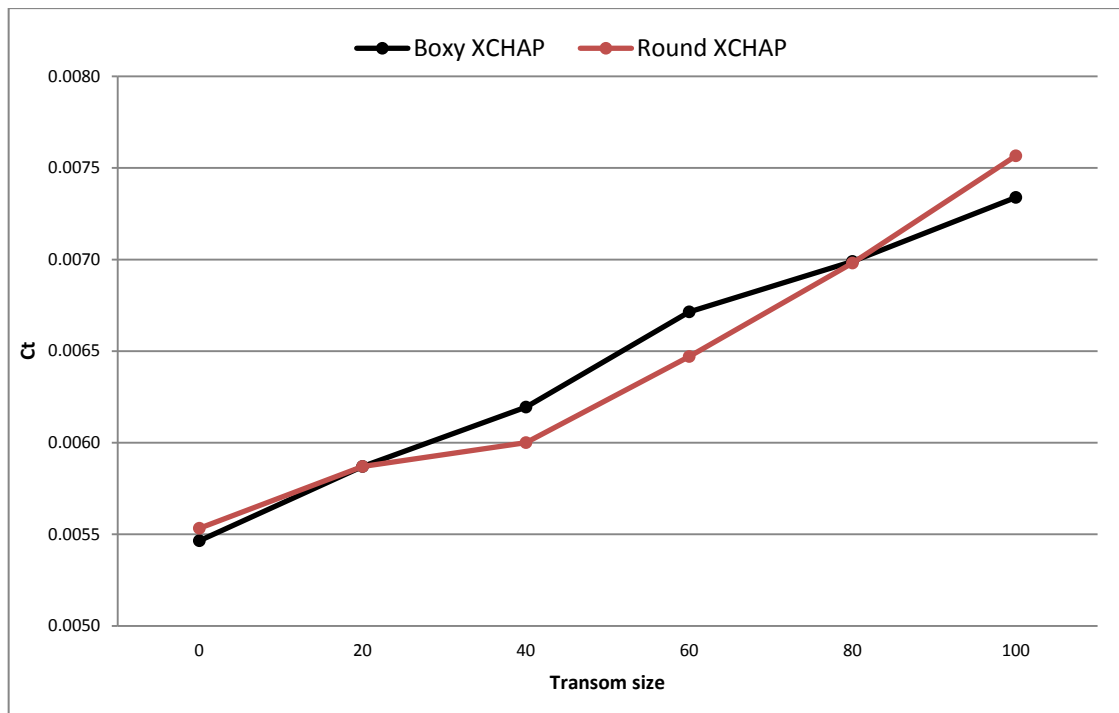


Figure 4.3.3.1.1. C_t plotted against transom size.

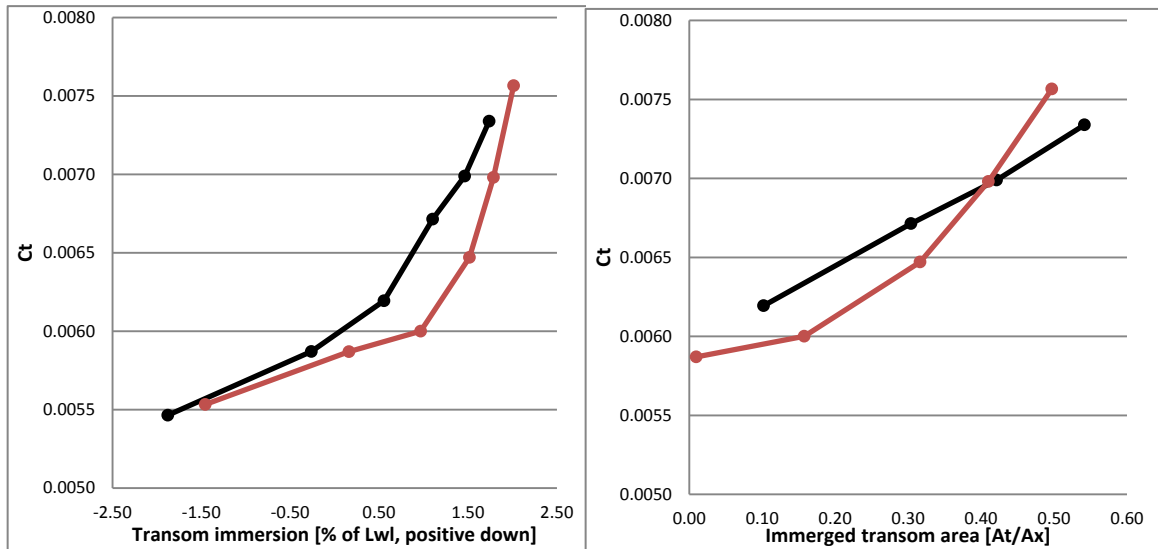


Figure 4.3.3.1.2. C_t plotted against *upright* transom immersion and *upright* immersed transom area.

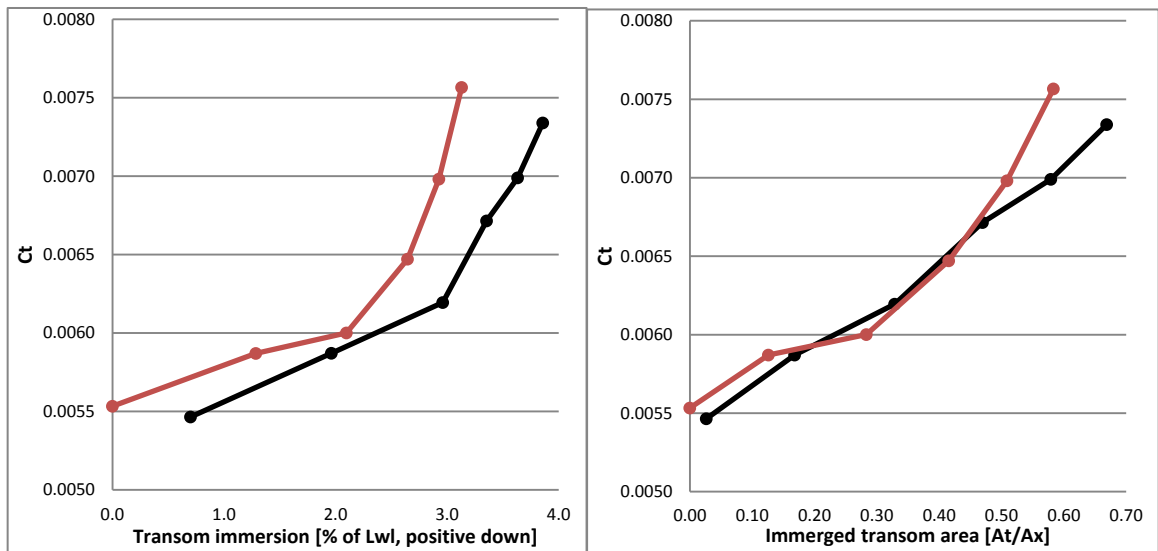


Figure 4.3.3.1.3. C_t plotted against *heeled* transom immersion and *heeled* immersed transom area.

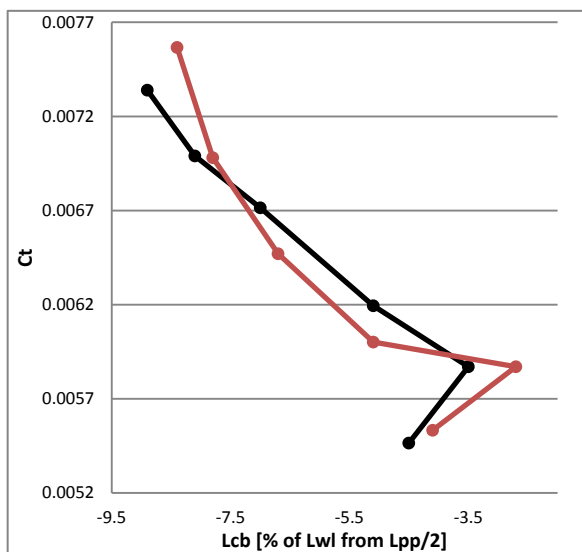
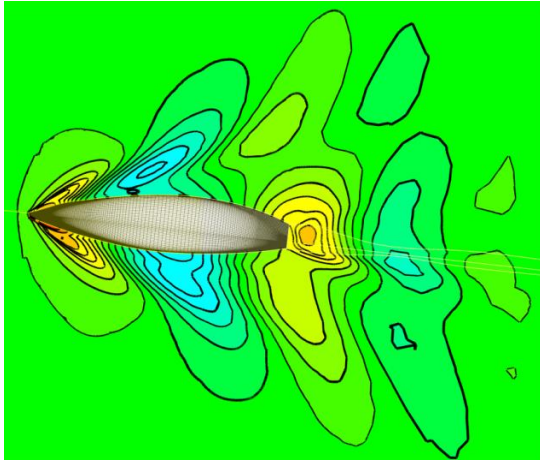
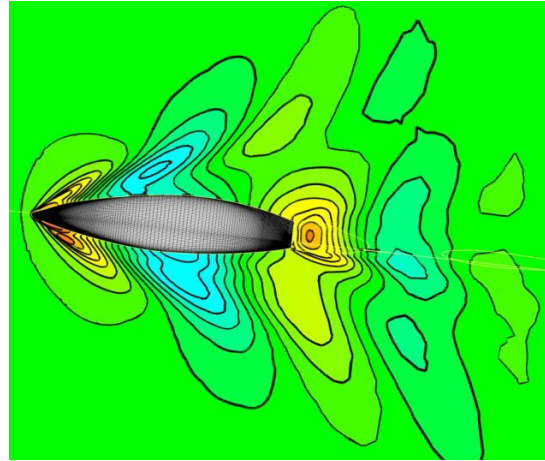


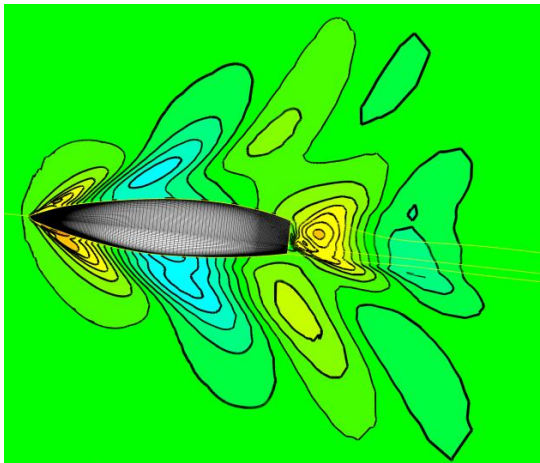
Figure 4.3.3.1.4. C_t plotted against L_{cb} .



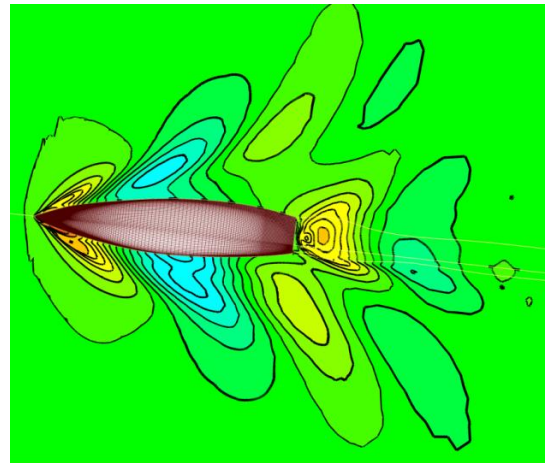
ND41-00b



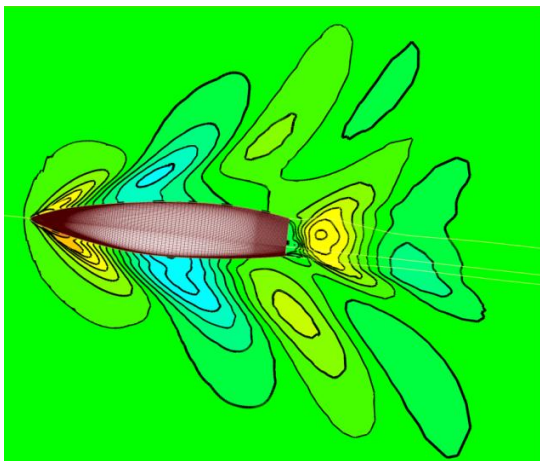
ND41-00r



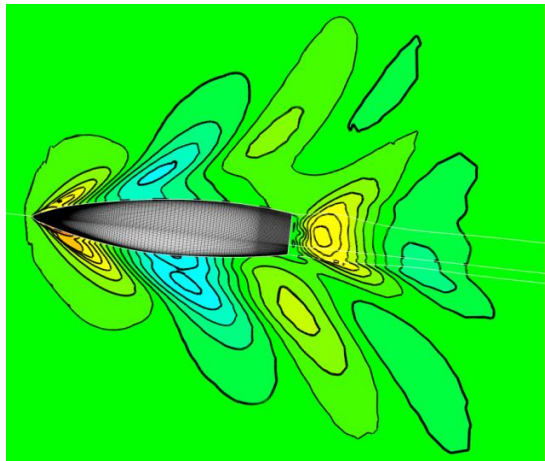
ND41-20b



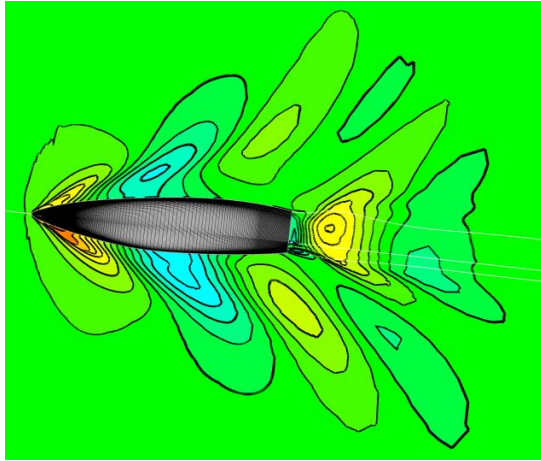
ND41-20r



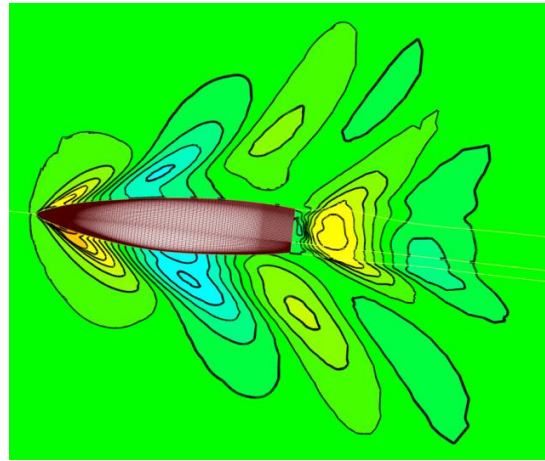
ND41-40b



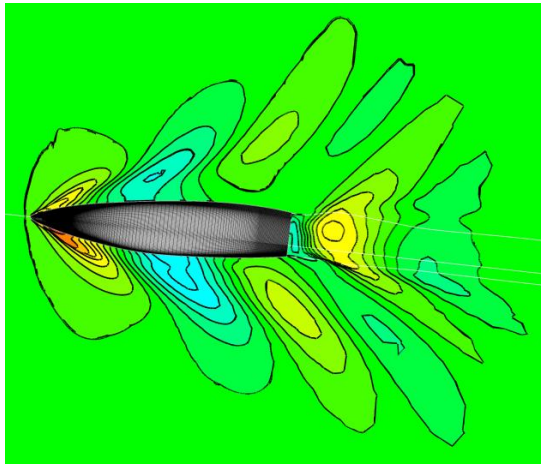
ND41-40r



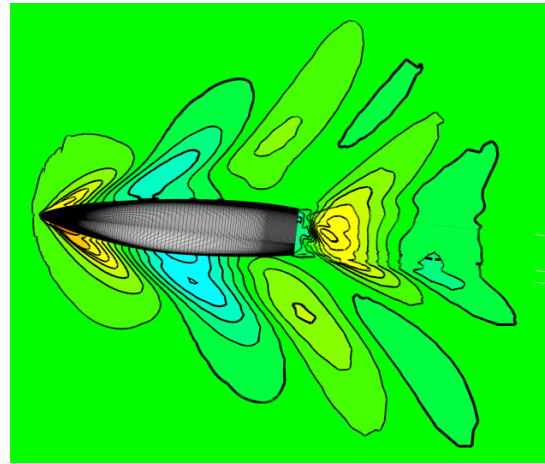
ND41-60b



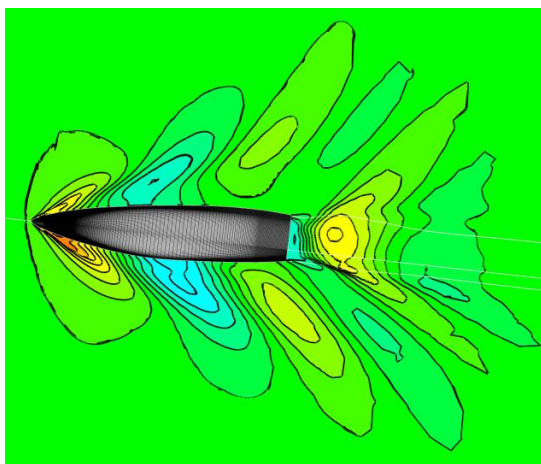
ND41-60r



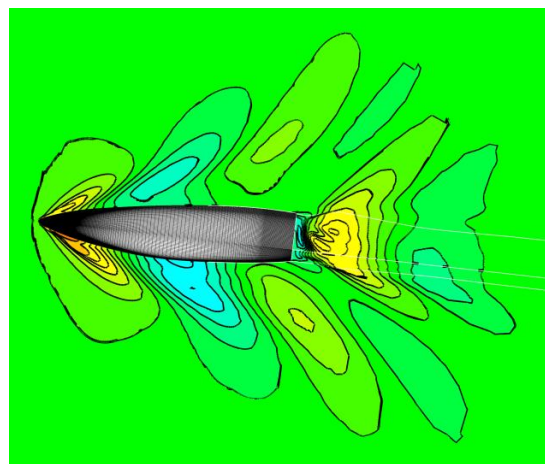
ND41-80b



ND41-80r



ND41-100b



ND41-100r

Figure 4.3.3.1.5. Wave pattern comparisons between boxy transoms (left column) and round transoms (right column) with increasing transom size at Froude number 0.35.

4.3.3.2 Discussion

There is no optimum transom size found for this condition. The tendency is that the transom should be even smaller than for the 00 hulls before any optimum is found. The transom is immersed and wetted for all hulls, and thus the base drag described in Chapter 4.3.1.2 is again relevant.

There is no transom shape that is best for all transom sizes, but the round one is better for all but two transom sizes and in those cases it is just slightly worse than the boxy one. From the wave pattern it is hard to see any significant differences between the bow wave systems, but at the stern the round transom displays a somewhat larger wave. This is probably due to the differences in the buttock angle when heeled. The round one has a much larger angle. As seen in Figure 4.3.3.2.1 below, the appearance of the stern waves is rather different. So despite the round transom generates a larger stern wave, and seemingly a similar bow wave, the base drag of the boxy transom must give such an addition in resistance so that the boxy transom still performs worse in this condition. The base drag is reduced when the immersed transom area is reduced, and thus the differences between the boxy and round transoms are smaller for the 00 and 20 hulls.

Again, it should be taken into account that the boxy transom has an advantage from a more suitable midship-section, as discussed in Chapter 5.2.

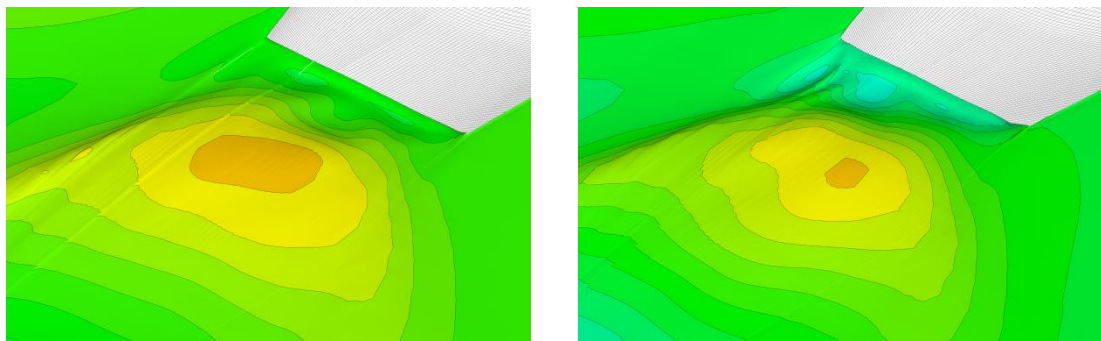


Figure 4.3.3.2.1. The stern waves of the round (left) and boxy (right) transoms from the ND41-40. Despite a smaller stern wave and seemingly similar bow wave the base drag of the boxy transom results in higher total resistance.

4.3.4 Heeled 20° at Froude number 0.60

4.3.4.1 Results

In Table 4.3.4.1.1 the resistance coefficients from the potential flow (XPAN) and RANS flow (XCHAP) computations are presented. XBOUND was not used for any heeled cases and thus no frictional resistance is computed in the potential flow model. In Figure 4.3.4.1.1 C_t from XCHAP is plotted against transom size for boxy and round transoms. In Figures 4.3.4.1.2 and 4.3.4.1.3 C_t is plotted against transom immersion and immersed transom area with hydrostatic data from both upright and heeled condition. Since not all transom sizes are immersed at zero speed, there are no data points for these hulls in the plots. Figure 4.3.3.1.4 is a plot of C_t against L_{cb} . Figure 4.3.4.1.5 is a comparison between the wave patterns with varying transom shape and size.

Table 4.3.3.1.1. XCHAP and XPAN results for ND41 variations at heeled condition and $Fn = 0.60$.

Hull	XPAN		XCHAP			
	C_w	C_t	S_w [m ²]	C_f	C_p	C_t
ND41-00b	0.00640	0.00640	No data			
ND41-20b	0.00523	0.00523	0.72510	0.00322	0.00727	0.01036
ND41-40b	0.00480	0.00480	0.72406	0.00321	0.00660	0.00967
ND41-60b	0.00471	0.00471	0.72406	0.00323	0.00631	0.00941
ND41-80b	0.00469	0.00469	0.72196	0.00323	0.00613	0.00921
ND41-100b	0.00472	0.00472	0.71987	0.00323	0.00600	0.00906
ND41-00r	0.00668	0.00668	0.73417	0.00319	0.00872	0.01191
ND41-20r	0.00523	0.00523	0.72999	0.00318	0.00743	0.01055
ND41-40r	0.00476	0.00476	0.72475	0.00321	0.00658	0.00966
ND41-60r	0.00463	0.00463	0.72301	0.00321	0.00627	0.00933
ND41-80r	0.00461	0.00461	No data			
ND41-100r	0.00463	0.00463	0.71882	0.00322	0.00598	0.00900

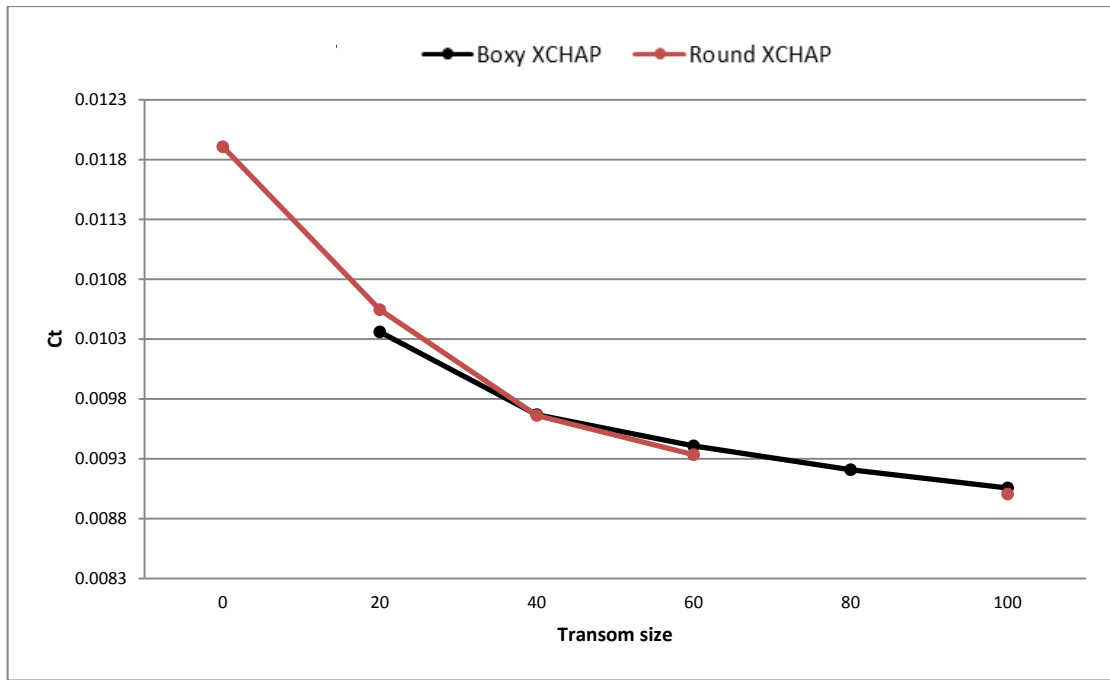


Figure 4.3.4.1.1. C_t plotted against transom size. Black line corresponds to boxy transom and red to round transom.

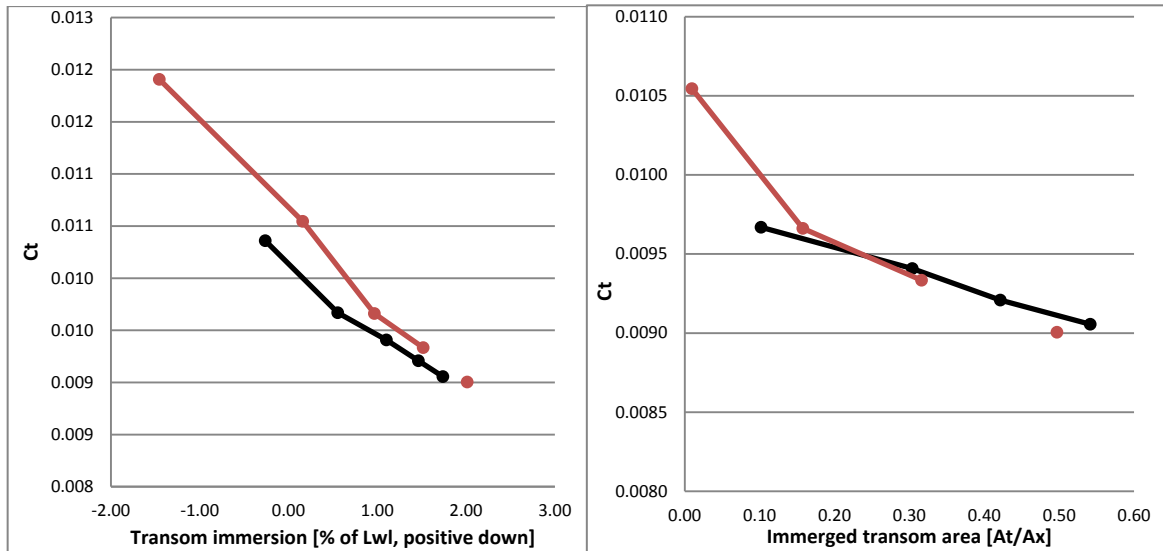


Figure 4.3.4.1.2. C_t plotted against *upright* transom immersion and *upright* immersed transom area.

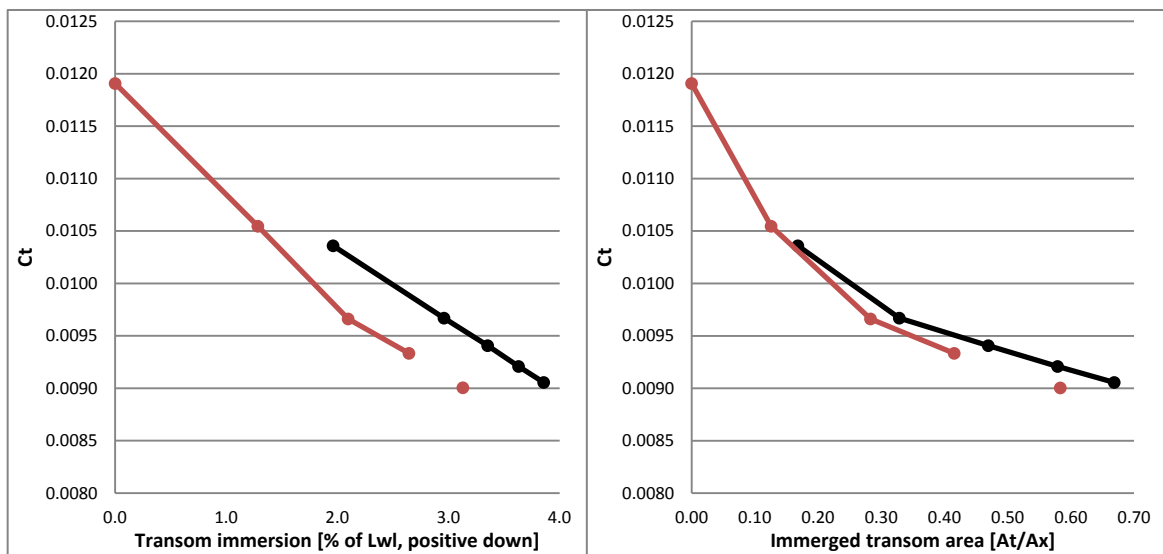


Figure 4.3.4.1.3. C_t plotted against *heeled* transom immersion and *heeled* immersed transom area.

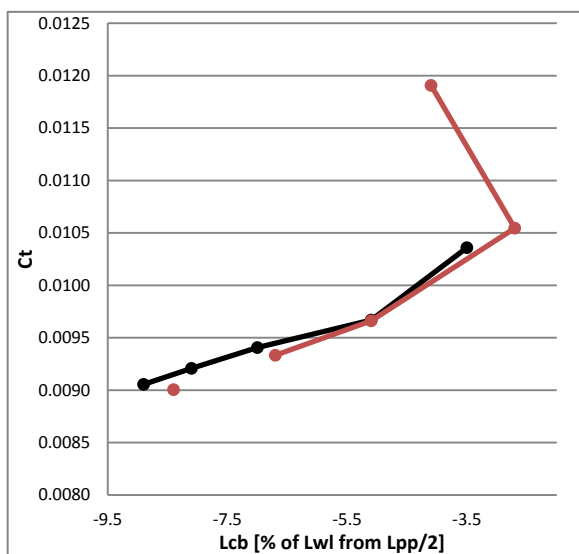
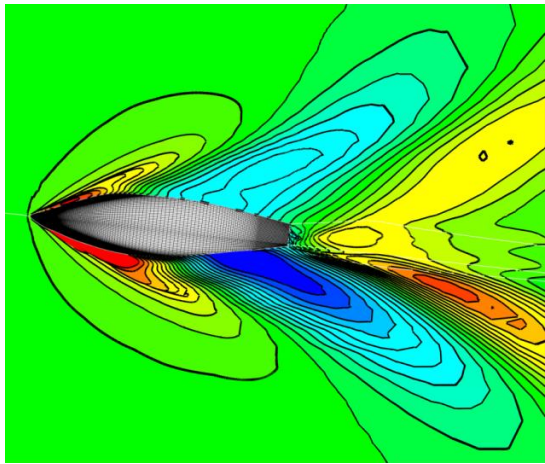


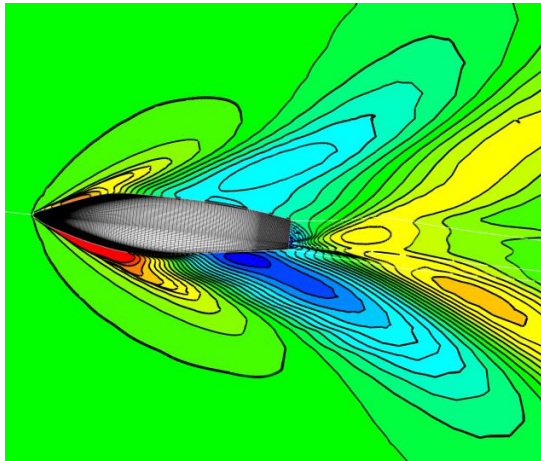
Figure 4.3.4.1.4. C_t plotted against L_{cb} .



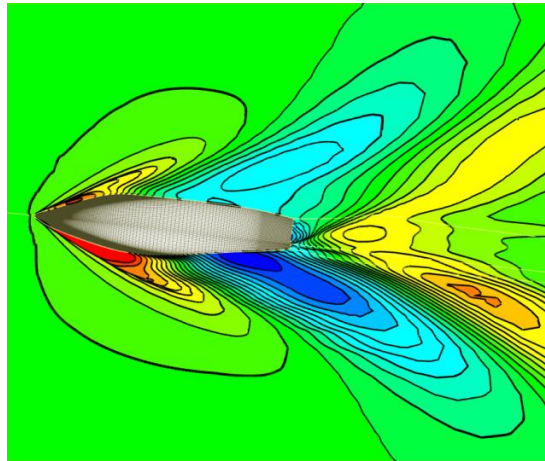
ND41-00b



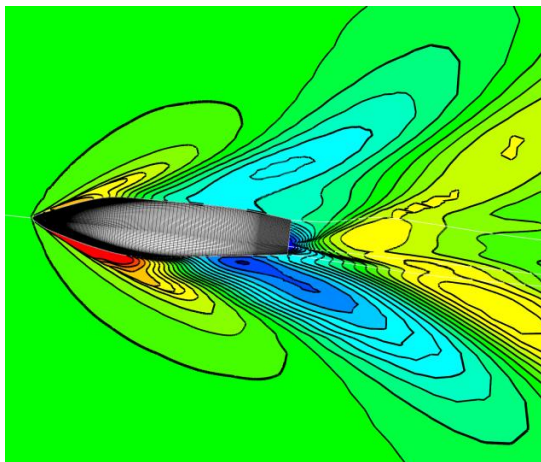
ND41-00r



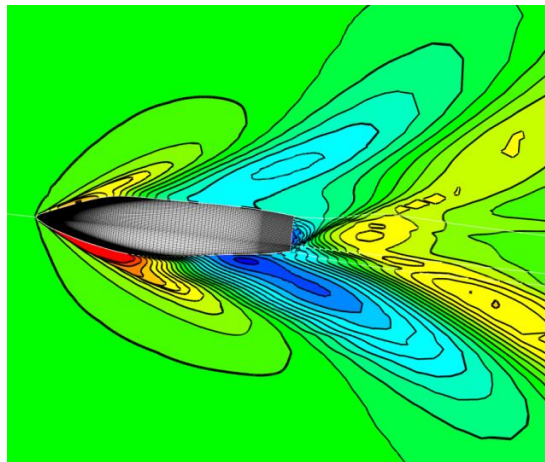
ND41-20b



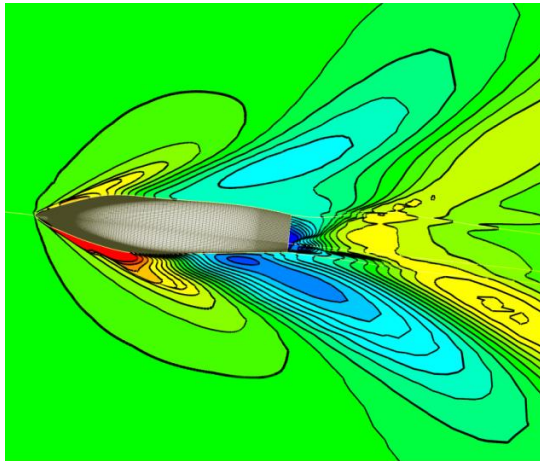
ND41-20r



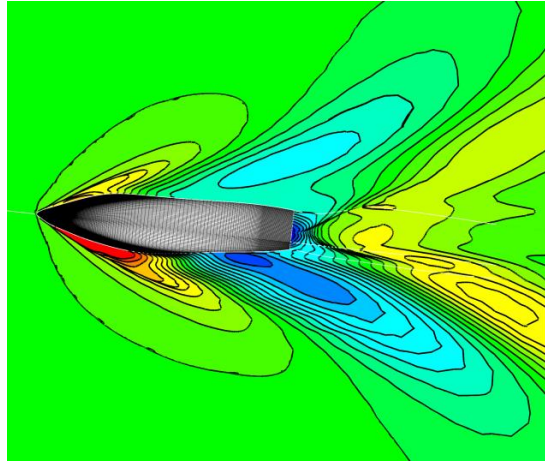
ND41-40b



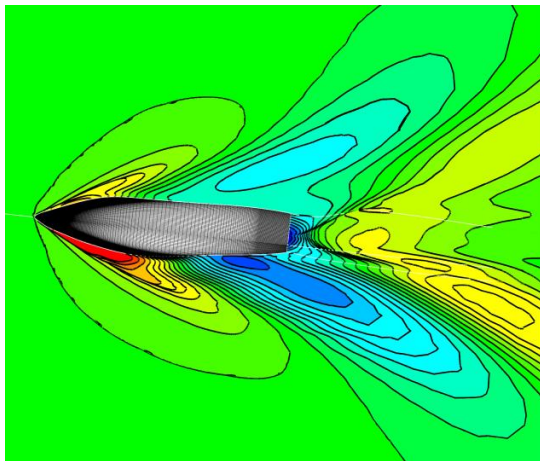
ND41-40r



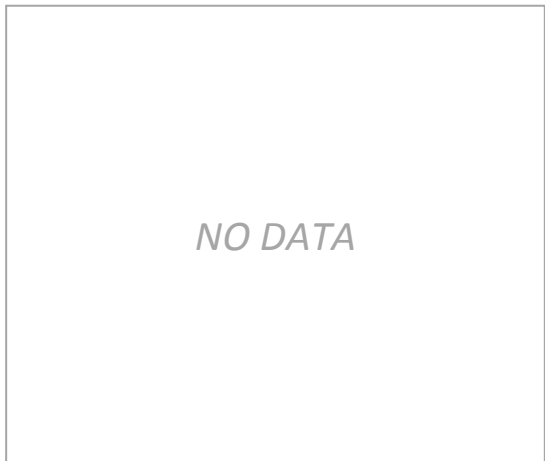
ND41-60b



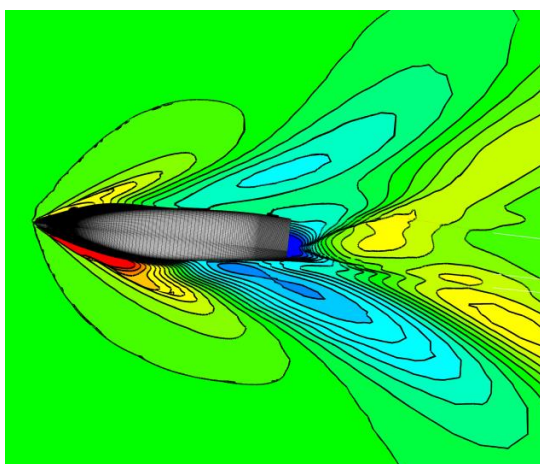
ND41-60r



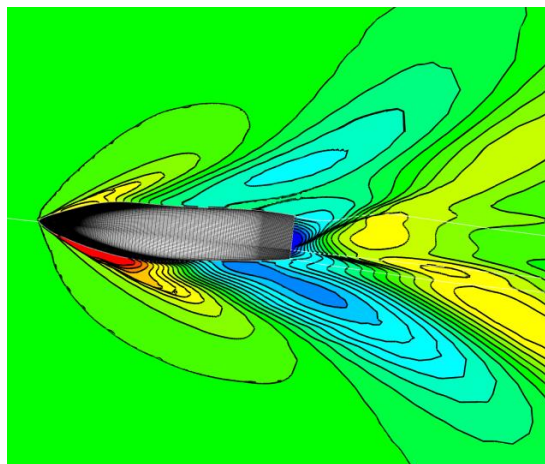
ND41-80b



NO DATA



ND41-100b



ND41-100r

Figure 4.3.4.1.5. Wave pattern comparisons between boxy transoms (left column) and round transoms (right column) with increasing transom size at Froude number 0.60.

4.3.4.2 Discussion

There is no optimum found at this condition but the trend that a big transom is more beneficial than a small one is very clear. The transoms are cleared for all hulls.

The hulls with round transom shows slightly lower resistance than the ones with boxy. The waterlines when heeled are no longer symmetric, as seen in Figure 4.3.4.2.1 where the waterlines of ND41-40 are presented. There is practically no difference between the leeward waterlines of the boxy and round transom hulls. Despite this the wave through from the bow wave system is slightly larger for the rounded transom (see Figure 4.3.4.1.5). This is explained by the different buttock lines of the hulls when heeled. The round transoms buttock lines are a little more curved than the buttock lines for the boxy transom hulls, and thus it generates lower pressure. The low pressure at the bottom of the hull is spread to the sides and the trough is increased. To windward the waterline is more curved for the boxy transoms, but it is hard to distinguish any trend with a deeper through to windward for the boxy transom hulls. Again, this could be due to the effects of the different buttock lines.

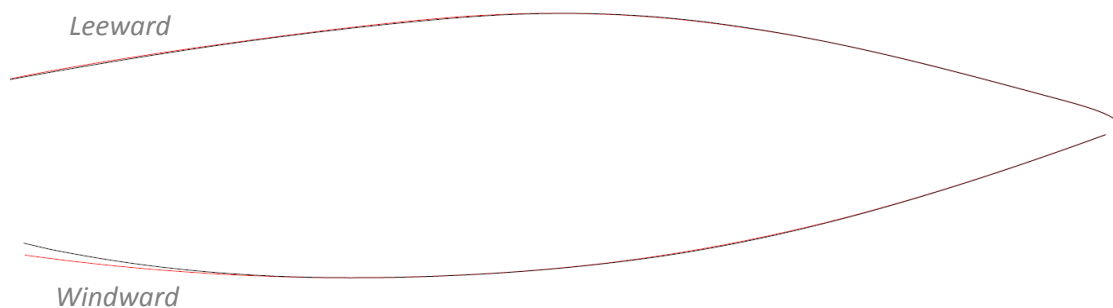


Figure 4.3.4.2.1. Waterlines of the heeled ND41-40. The black line is the one of the hull with boxy transom while the red is for round transom. Note the increased curvature on the windward side for the round transom.

Thus, from the reasoning above the wave patterns indicate that the boxy transom should be better, which is not the case according to the results. Left to consider is the transom resistance. In Chapter 2.2, equation (2.3) defines the transom resistance and it is seen that it is dependent on immersed transom area, and the distance between the z-coordinate of the centroid of the area and the waterline. In Figure 4.3.4.2.2 one can see that the shape of the immersed transom area of the boxy transom results in an increase in both of these variables. The other variables in the formula are more or less constant. Thus it is likely that it is the decreased transom resistance that makes the rounded transoms more beneficial.

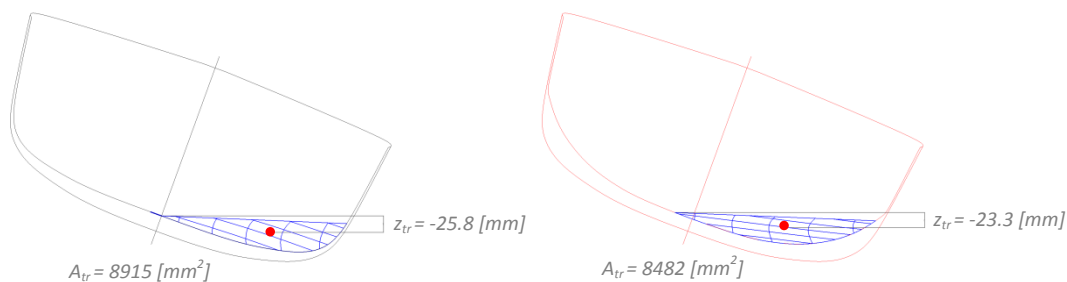


Figure 4.3.4.2.2. The immersed transom areas of the ND41-100 with boxy (left) and rounded (right) transom shapes. The red dots are the area centroids.

4.3.5 Upwind-Downwind race

Table 4.3.5.1 is an assembly of the performance of the different hulls if they were to sail an upwind – downwind race course. The effective speed towards the top of the race course (upwind) is slower for two reasons. First, it is not possible to sail straight into the wind and therefore one must zigzag up the race course and thereby sail a longer way. Secondly, it is not as efficient sailing upwind as downwind and thus the speed through the water is slower than going downwind when the yacht is sailing faster.

Therefore the resistance coefficients have been weighted correspondingly in order to account for these inevitable conditions. Upwind the resistance coefficient for heeled condition at Froude number 0.35 is used, and downwind the one for upright condition at Froude number 0.60 is used.

In the table, the fastest hull is on top, and then the second, third and so on follows in order. This is a rough estimation of the performance of the different hulls on a rather windy day. The Froude numbers corresponds to a speed through the water of 12.17 knots downwind and 7.10 knots upwind. Of course some more speeds would have been desirable to be able to present a wider spectrum of each hulls performance, but at the same time it gives a hint.

The round transoms outperform the boxy ones with corresponding transom size for all hulls at the top half of the scoreboard. In the lower half, the boxy transoms are equally good for hulls 00 and 80. It is not until the last pair of hulls, the 100 hulls, that the boxy transom is actually faster around the course.

Table 4.3.5.1 Upwind-downwind race results

Hull	Difference time sailed [%]	Cp	At/Ax upright	Lcb [% of Lwl]
ND41-40r	0.0	0.593	0.16	-5.1
ND41-40b	+1.9	0.598	0.10	-5.1
ND41-20r	+2.6	0.551	0.01	-2.7
ND41-60r	+2.7	0.616	0.32	-6.7
ND41-20b	+3.1	0.568	0.00	-3.5
ND41-60b	+4.8	0.631	0.30	-7.0
ND41-00b	+5.1	0.562	0.00	-4.5
ND41-00r	+5.1	0.559	0.00	-4.1
ND41-80b	+6.4	0.633	0.42	-8.1
ND41-80r	+6.4	0.628	0.41	-7.8
ND41-100b	+8.8	0.652	0.51	-8.9
ND41-100r	+11.9	0.640	0.50	-8.4

4.3.6 The waterline effect on the wave creation

The plots in this chapter shows how the wave height along the hull varies with the waterline curvature. The waterlines of two different hulls are shown underneath the graph which displays the wave height, H , (solid line) and the submerged section area, A_s , (dashed line) for each hull.

At Froude number 0.6 the bow wave length is longer than one boat length. From the plots below, and from the wave patterns earlier in this chapter, it can be seen that the waterline curvature has very large impact on the wave resistance. A waterline with a lot of curvature that coincides with the trough of the bow wave system significantly enhances the trough. As seen in the plots and tables of the upright condition at Froude number 0.6 in the results chapter, the best hulls are the ones with the box shaped transoms, and thus the straighter waterlines. This is despite the fact that the round transom with the same transom size have straighter buttock lines and deeper transom immersion, which is also desirable. So, in a sense straighter waterlines seem to compensate for the drawbacks of rounder buttock lines and less transom immersion. The immersed transom area is however rather similar which indicates that the waterline curvature would be more important than the mere transom immersion.

Basically, where the curvature of the waterline is placed, and how curved it is, could decide which Froude number the yacht will be optimized for in the upright condition since it determines the non-favourable interaction between the low pressure and the bow wave trough.

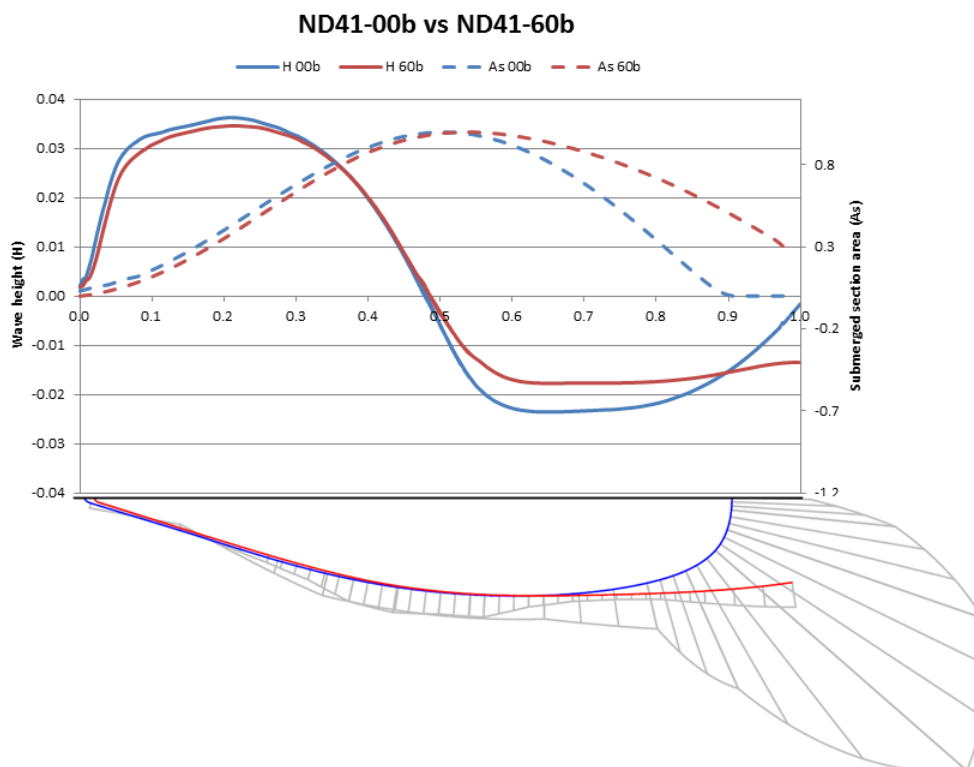


Figure 4.3.6.1. Illustration of how the wave height along the hull (solid lines) and submerged section area (dashed lines) varies with the waterline shape (seen below the x-axis) at Froude number 0.60. Note how the wave height increases with the curvature of the waterline of ND41-00b with smaller transom.

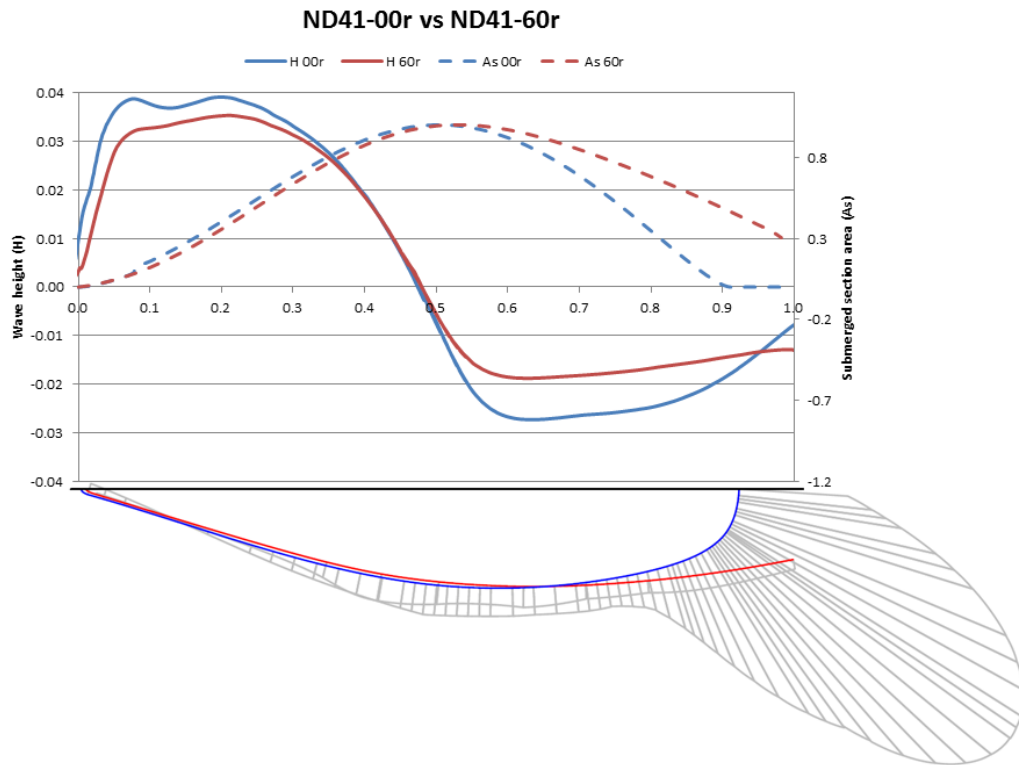


Figure 4.3.6.2. Illustration of how the wave height along the hull (solid lines) and submerged section area (dashed lines) varies with the waterline shape (seen below the x-axis) at Froude number 0.60. Note how the wave height increases with the curvature of the waterline of ND41-00r with smaller transom.

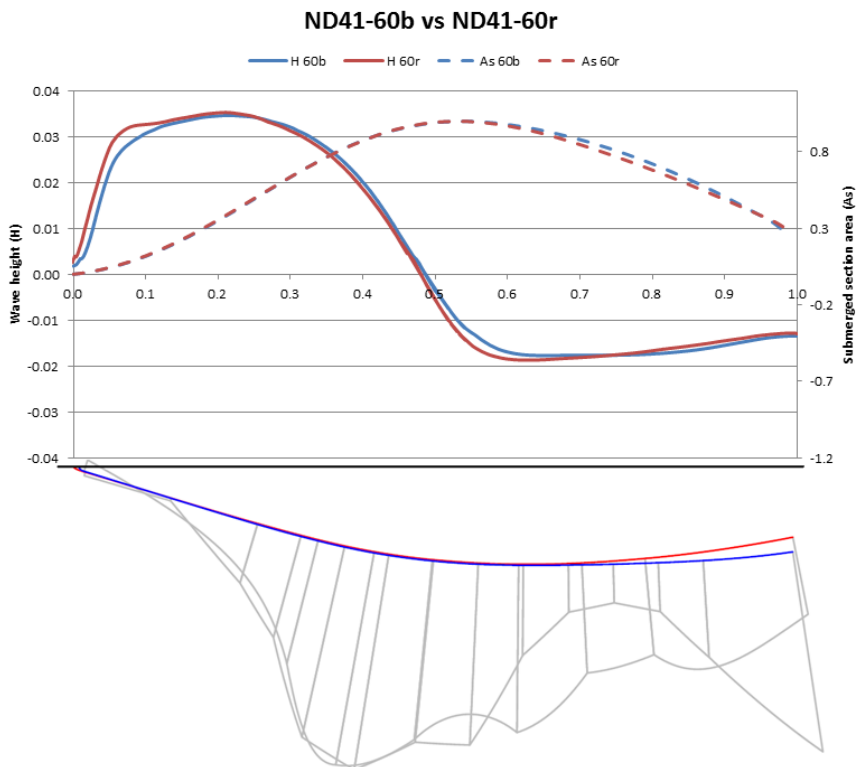


Figure 4.3.6.3. Illustration of how the wave height along the hull (solid lines) and submerged section area (dashed lines) varies with the waterline shape (seen below the x-axis) at Froude number 0.60

4.3.7 The rocker curve effect on the hydrodynamic pressure resistance

In Figures 4.3.7.1-4 the hydrodynamic pressure along the centreline of the hull at Froude number 0.6 is plotted for different hulls. This line is referred to as the rocker curve. In the figures the centreline of the yacht bottom surface is also plotted to illustrate how the hydrodynamic pressure contributes to the resistance of the yacht. A negative pressure forward of the deepest point will contribute in such a way that it pulls the hull forward. Consequently, a negative pressure behind the deepest point of the hull will suck the yacht backward and increase the resistance. From the plots below, it is rather clear that a high curvature rocker line as the ones on the 00 hulls have a very negative effect on pressure resistance at high Froude numbers. There are also other effects from the rocker line. The low pressure on the bottom may spread to the sides and cooperate with that from the curved waterlines and further deepen the wave trough. The same low pressure will also cause the yacht to trim more on the stern and increase the sinkage.

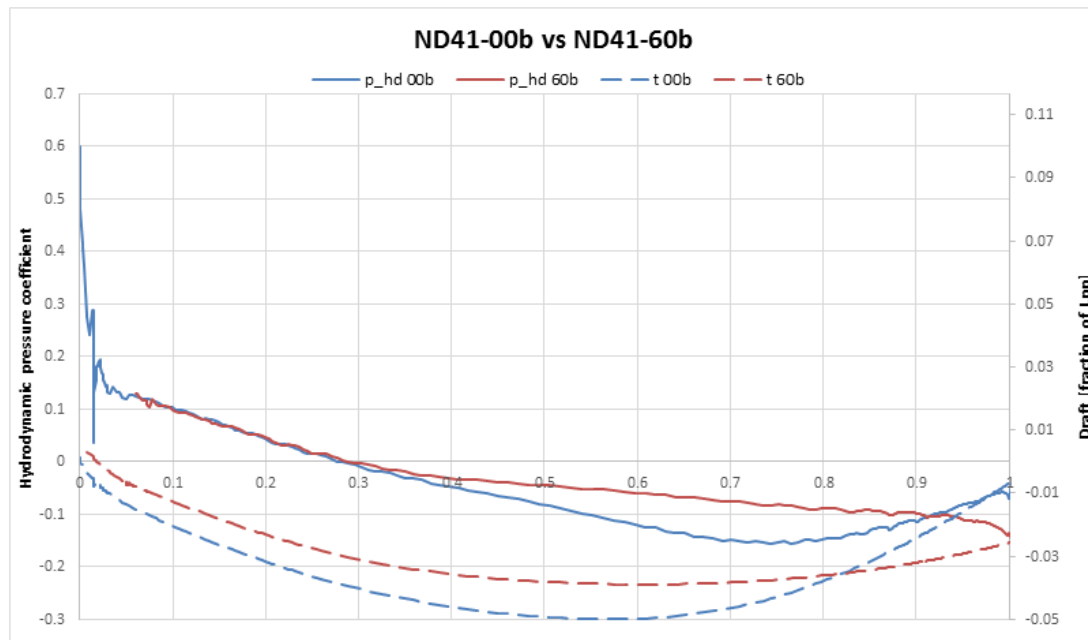


Figure 4.3.7.1. Illustration of how the hydrodynamic pressure coefficient varies along the centreline of hulls with different transom size and rocker lines at Froude number 0.6.

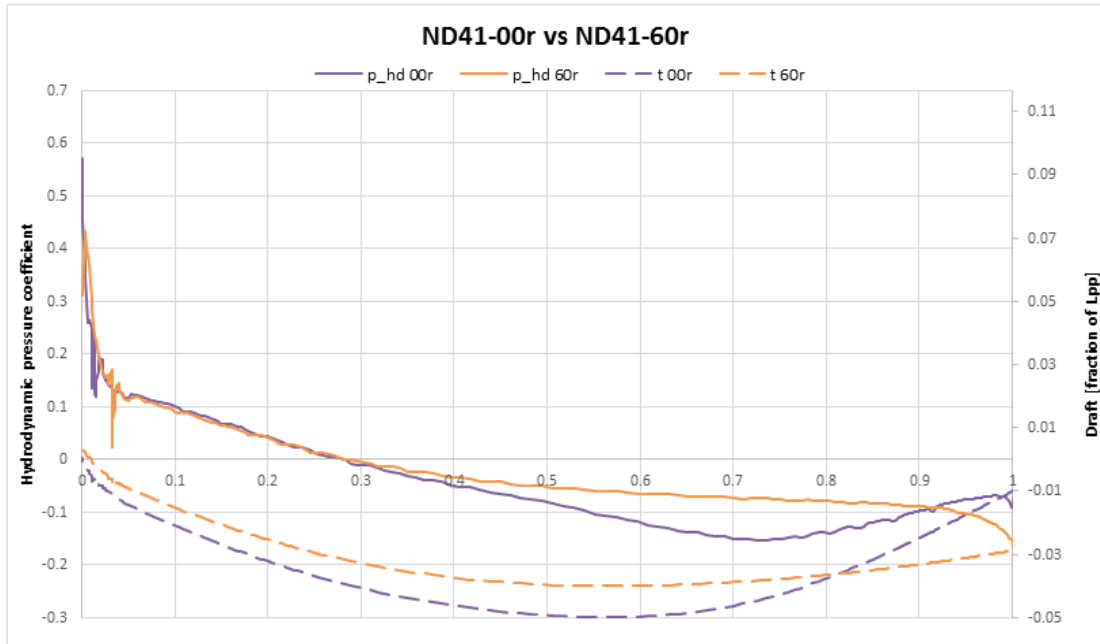


Figure 4.3.7.2. Illustration of how the hydrostatic pressure coefficient varies along the centreline of hulls with different transom size and rocker lines at Froude number 0.6.

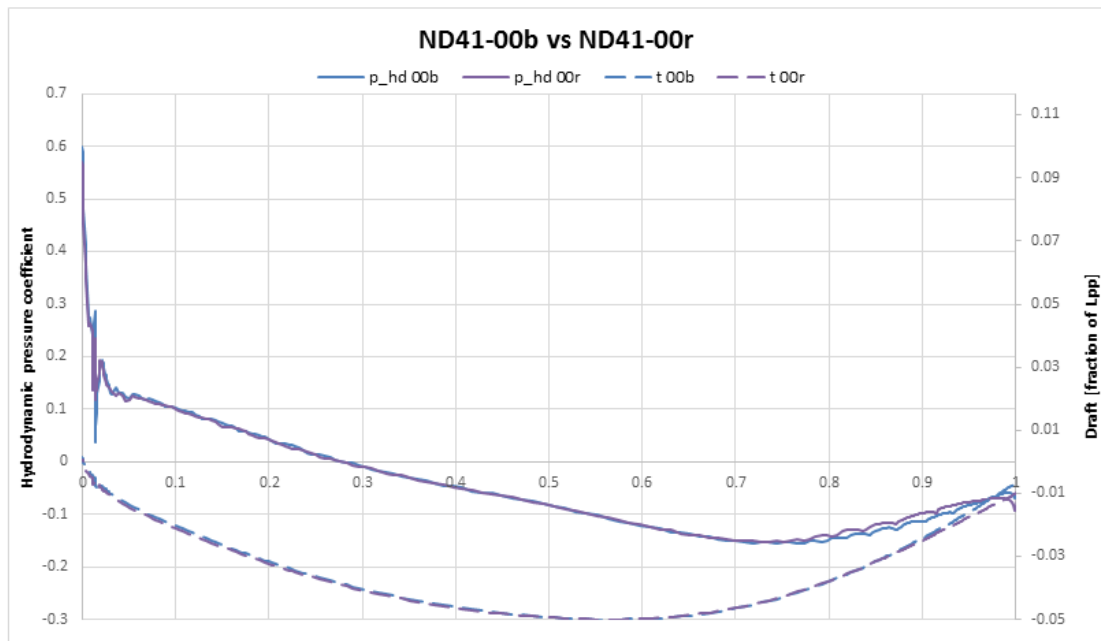


Figure 4.3.7.3. Illustration of how the hydrostatic pressure coefficient varies along the centreline of hulls with same transom size but different rocker lines at Froude number 0.6.

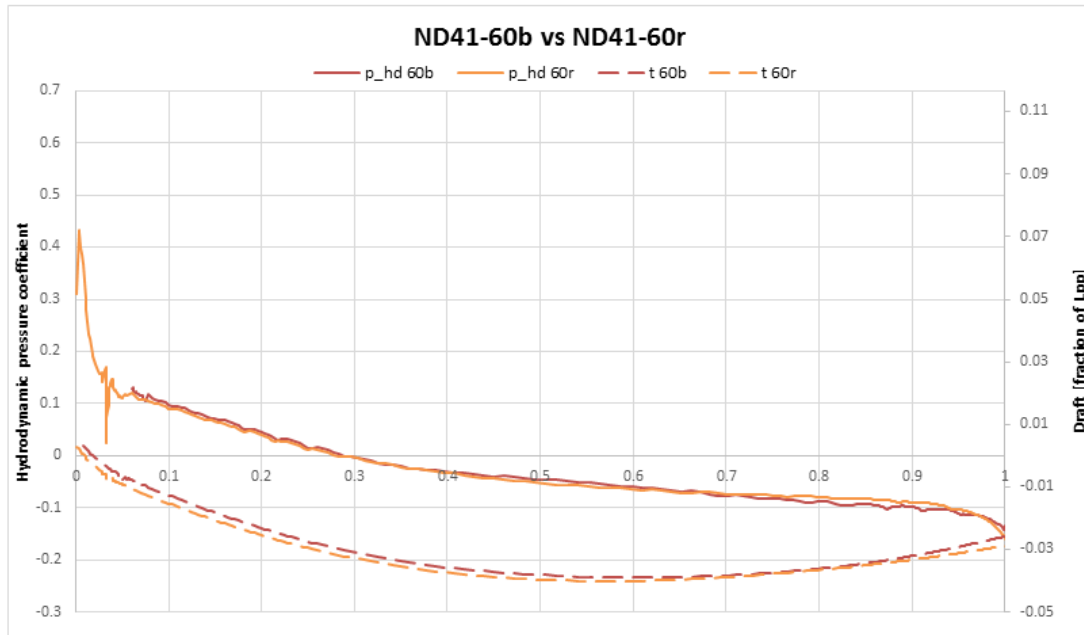


Figure 4.3.7.4. Illustration of how the hydrostatic pressure coefficient varies along the centreline of hulls with same transom size but different rocker lines at Froude number 0.6.

4 Summary

In this study, a systematic transom geometry variation study has been performed on a modern 41 ft performance cruiser using the latest computational hydrodynamic RANS software to compute the resistance of the hulls. Several hulls have been tested in upright and heeled condition at various speeds. The objective is to investigate whether the modern hull lines with wide, box-shaped transoms that seem to originate from extreme racing machines also are beneficial for modern performance cruisers, from a hydrodynamic performance point of view.

The study consists of three parts. In the first part a verification of the numerical CFD software SHIPFLOW 5.0 is conducted using the Least Square Root method. The software proved to perform well for the upright condition where the uncertainty was calculated to 3.1 % for the total resistance coefficient. For the heeled condition the uncertainty was larger, 15.6 %, but only 4 different grid densities were tested which is few.

The second part is a validation of the software. Experimental resistance data from towing tank tests of several different sailing yacht hulls is compared to the results from the CFD computations that are conducted on the same hulls. For the upright condition the results from the computations are consistent with the experimental data at low and medium Froude numbers, but under predicts with up to 16.5 % at higher speeds. The trend of the under predicted resistance is however constant for all investigated hulls. In heeled condition the results are mainly within 6 % from the experimental results. In spite of the absolute differences between the computed and measured results the relative differences between the hulls are well predicted, which is sufficient for the subsequent optimisation.

In the third step of the project a modern 41 ft performance cruiser (the ND41) was designed. It was intended to be somewhat of an average design of yachts in the segment that are presently on the market. The aft ship of the ND41 was then stretched stepwise and cut at constant length overall in order to systematically increase the transom size. Six hull variations with box shaped transoms were created in this way. To investigate the influence of the transom shape, the six hull variants were also equipped with a more rounded transom. The resistance was calculated for all twelve hulls in upright and heeled condition at Froude numbers 0.35 and 0.60.

At Froude number 0.60 no optimum was found and the largest transoms proved to cause least resistance in both upright and heeled condition. The difference in resistance between the transom shapes were small but the boxy one is marginally better for the upright condition, while the round is better for the heeled condition. At the same speed, it was discovered that it is beneficial to have the longitudinal centre of buoyancy very far aft. The fastest hull has its LCB about 9% of Lwl behind the midship section, and yet no optimum was found.

At the low speed and heeled condition no optimum was found but the smallest transoms performed best, with boxy transoms marginally better. In the upright condition at the same speed an optimum transom was found in the second smallest transom size with round shape.

In an upwind-downwind race the round transoms performed best for the three fastest transom sizes. The fastest hull around the course has an immersed transom ratio (A_t/A_x) of 0.16 and it is 1.9 % faster with round transom than with boxy. Overall the round transoms are faster around the race course.

It is highly likely that the hulls with boxy transoms are favoured in the study since the original hull is designed with a boxy transom and thus the mid-ship section fits this transom shape better. With that in mind there is reason to question whether there is any actual gain in performance with the modern box shaped transoms. From a hydrodynamic point of view there does not seem to be, but there could be other gains that are not considered in this study (e.g. improved righting moment).

The study has led to better understanding of the relation between hydrostatic and hydrodynamic resistance at high Froude numbers where the gain from a big immersed transom area is larger than the loss from increased transom resistance. Also, the influence on wave resistance from the curvature of the water and buttock lines has been clearly illustrated. For low Froude numbers where the transom is wetted the effect from viscous pressure resistance, base drag, has been pinpointed.

5 Future work

Due to the time limitations for the study, each hull could only be tested in four conditions. To give a better understanding of each hulls spectrum of performance, they could for example be run at Froude numbers 0.25 and 0.45, and at all speeds with heel angle 10° . The Froude numbers they are run at in this study corresponds to rather strong winds, at least for Froude number 0.60 in heeled and upright conditions, which might not be the conditions one would like to optimize the yacht for.

Since no minimums are found for three out of four conditions, it could be interesting to add some transom sizes that are both smaller and larger than the existing ones. Adding some speeds should, however, generate some new optimums.

The hulls with boxy transoms might benefit from having a mid-ship section that fit their transom shape better. If a hull was created with a midsection that fitted a rounded transom better, the variation could be done in the same way with two transom shapes, but with reversed relationship. That could also give some answers concerning the importance of the mid-section shape contrary to the transom shape.

The displacement to length ratio for the ND41 is rather high and it could be questioned how much the "performance" in performance cruiser really applies. The same fashion of the transom size and shape is however seen in most lighter yachts as well and maybe the trends found in this study is different for those yachts. A similar study on a series of hulls with decreased displacement to length ratio could therefore be interesting.

No yacht can be optimized for all conditions. Therefore it would be interesting to know what conditions a yacht that is racing in our waters encounters during a season. With that data known, a more sophisticated judgement on the most beneficial hull from the series could be done. That, in combination with a VPP program could be a very efficient tool when evaluating the hulls (or, of course, when designing new ones).

Although verification and validation was made very thoroughly in this study, a validation with towing tank tests with some of the hulls from the ND41 series would be appropriate, but most likely very far out of reach.

6 References

Eça, L., Hoekstra, M., (2006a): *Discretization Uncertainty Estimation Based on a Least Squares Version of the Grid Convergence Index*. Proceedings of the 2nd Workshop on CFD Uncertainty Analysis, Lisbon, Portugal, 27 pp.

Eça, L., Hoekstra, M. (2009): Evaluation of Numerical Error Estimation Based on Grid Refinement Studies with the Method of the Manufactured Solutions. *Computers & Fluids*, Vol. 38, Issue 8, September 2009, pp. 1580-1591

Eça, L., Vaz, G., Hoekstra, M. (2010): *Code Verification, Solution Verification and Validation in RANS solvers*. OMAE2010-20338. The American Society of Mechanical Engineers, New York, USA, 9 pp.

Eça, L., Vaz, G., Hoekstra, M., (2010b): *A Verification and Validation Exercise for the Flow over a Backward Facing Step*. Proceedings of the V European Conference on Computational Fluid Dynamics, ECCOMAS CFD 2010, Eds. Pereira J.C.F., Sequeira A., Lisbon, Portugal, 18 pp.

FLOWTECH International AB. (2007): *XCHAP Theoretical Manual*. FLOWTECH International AB. Gothenburg, Sweden, 22 pp.

Hoerner, S.F. (1965): *Fluid-Dynamic Drag*. Hoener Fluid Dynamics, Bricktown New Jersey, pp. 18-20.

Keuning, J.A., Sonnenberg U.B. (1999): *Approximation of the Calm Water Resistance on a Sailing Yacht Based on the Delft Systematic Yacht Hull Series*. Report 1177-P. Ship Hydromechanics Laboratory, Department of Marine Technology, Delft University of Technology, Delft, The Netherlands, 21 pp.

Kuening, J.A., Katgert, M. (2008): *A Bare Hull Resistance Prediction Method Derived from the Results of the Delft Systematic Yacht Hull Series Extended to Higher Speeds*. The Royal Institution of Naval Architects, London, 2008, 9 pp.

Larsson, L., Eliasson, R.E. (2000): *Principles of Yacht Design, 2nd edition*. Adlard Coles Nautical, London, 334 pp.

Larsson, L., Eliasson, R.E., Orych M (2014): *Principles of Yacht Design, 4th edition*. Adlard Coles Nautical, London.

Larsson, L., Raven, H.C. (2010): *Ship Resistance and Flow*. The Society of Naval Architects and Marine Engineers, Jersey City, New Jersey, 230 pp.

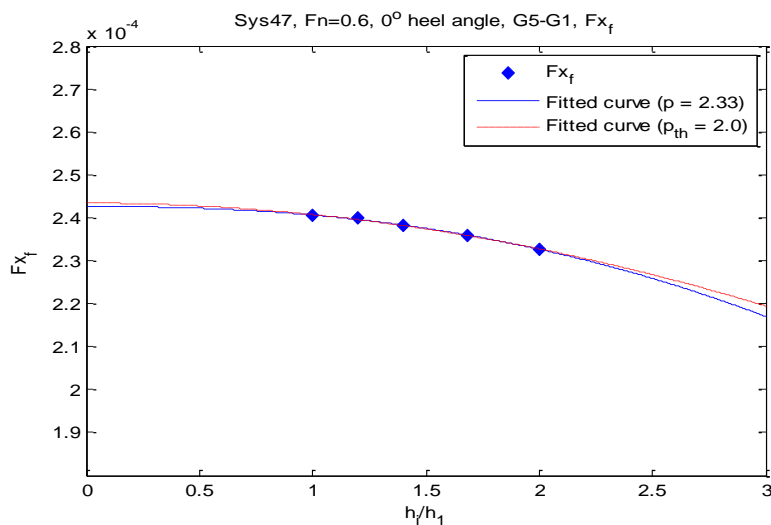
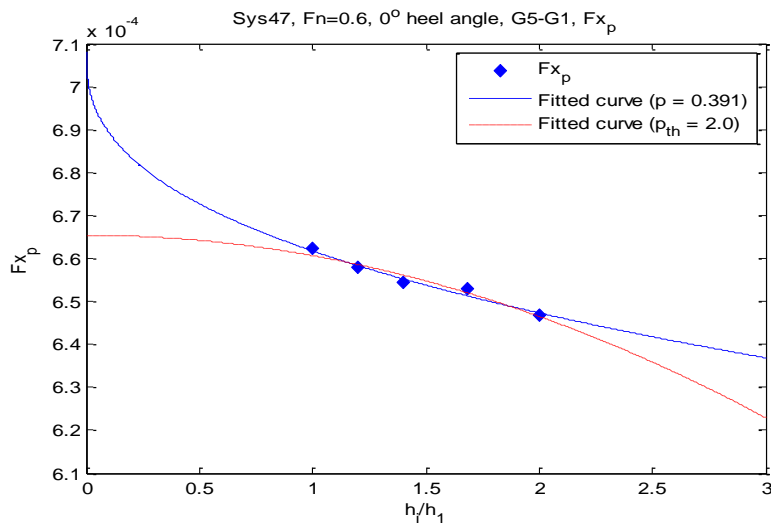
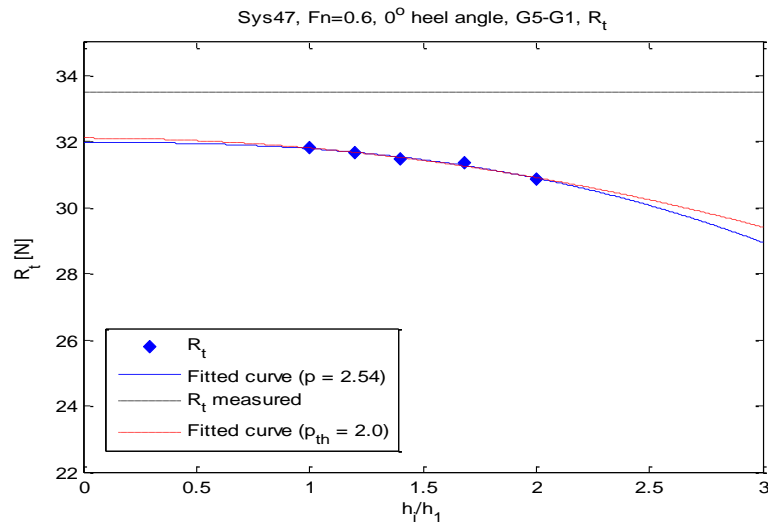
Roache, P. J. (1998): *Verification and Validation in Computational Science and Engineering*. Hermosa Publishers, Albuquerque, New Mexico, USA.

The American Society of Mechanical Engineers (2009): *Standard for Verification and Validation in Computational Fluid Dynamics and Heat Transfer*, The American Society of Mechanical Engineers, New York, USA, 102 pp.

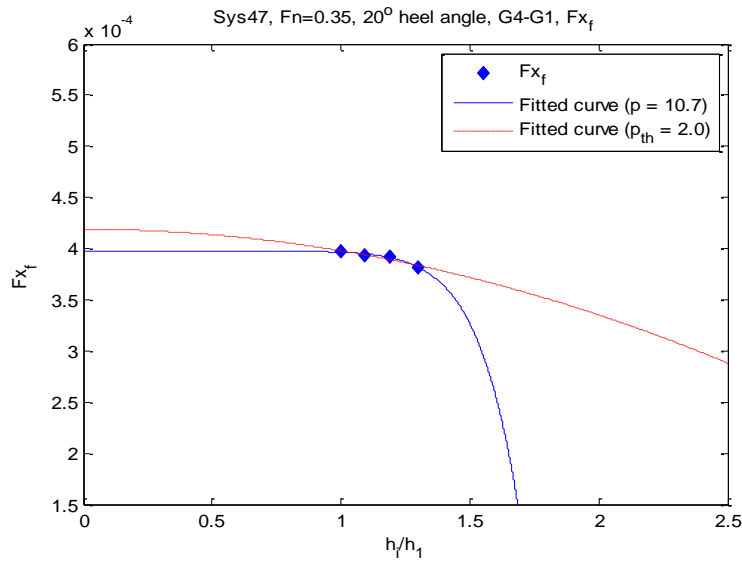
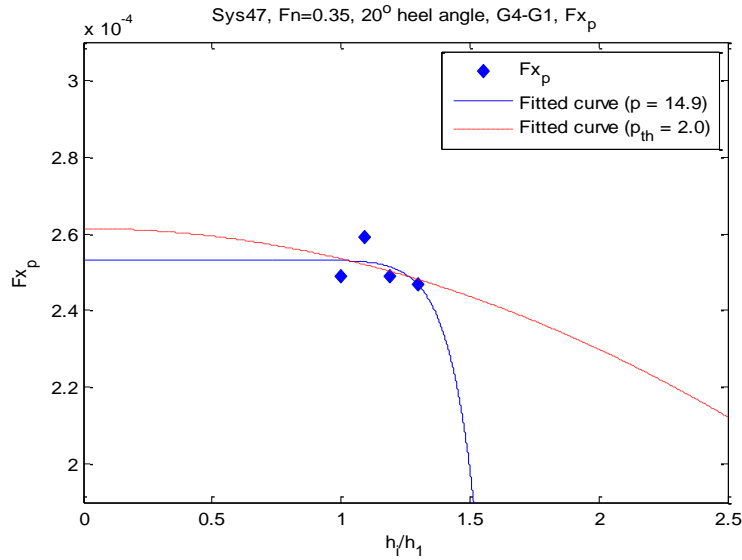
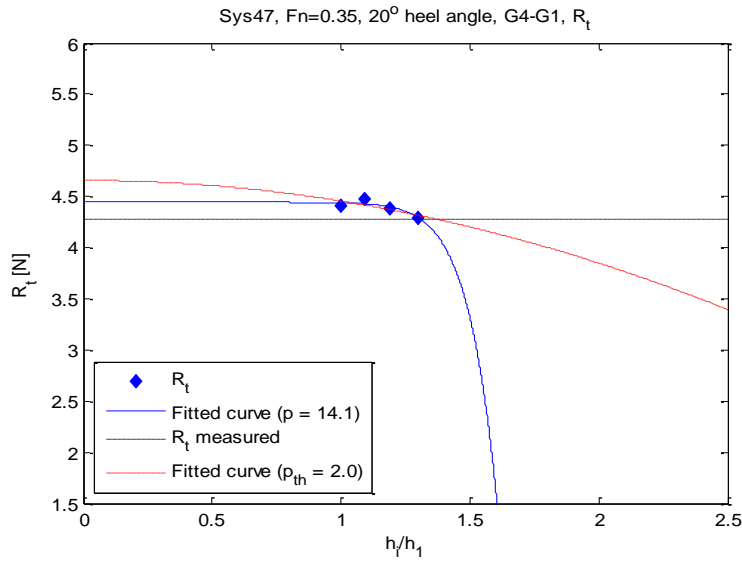
Zou, L. (2012): *CFD Predictions Including Verification and Validation of Hydrodynamics Forces and Moments on Ships in Restricted Waters*. Ph. D Thesis. Department of Shipping and Marine Technology, Chalmers University of Technology, Publication no. 3407, Gothenburg, Sweden, 2012, 182 pp.

Appendix I - Verification

I.1 Upright condition



I.2 Heeled condition



Appendix II – Validation

II.1 Hydrostatics Sysser hulls

	Sysser 46	Sysser 47	Sysser 48	Sysser 49	Sysser 50
lwl [m]	1.71	1.71	1.71	2	2
t [m]	0.093	0.085	0.088407	0.0946	0.095
lcb [m]	0.799	0.752	0.843885	0.8732	0.842
lcf [m]	0.748	0.711	0.768987	0.8314	0.817

II.2 Sysser 46 upright measurement data

V [m/s]	Fn	Rt [N]	z [mm]	θ [deg]
0.409	0.10	0.341	-0.886	0.010
0.614	0.15	0.713	-1.606	0.032
0.819	0.20	1.219	-2.695	0.070
1.023	0.25	1.926	-4.213	0.130
1.434	0.35	4.705	-9.415	0.245
1.638	0.40	8.777	-13.789	0.001
1.843	0.45	16.175	-17.995	-0.799
2.047	0.50	24.925	-21.024	-1.813
2.253	0.55	31.280	-23.008	-2.439
2.457	0.60	36.638	-18.693	-3.354
2.662	0.65	40.557	-15.570	-3.843
2.867	0.70	43.887	-13.441	-3.980
3.072	0.75	46.778	-10.892	-3.942

II.3 Sysser 47 upright measurement data

V [m/s]	Fn	Rt [N]	z [mm]	θ [deg]
0.409	0.10	0.315	-0.664	-0.007
0.512	0.13	0.491	-0.843	0.010
0.614	0.15	0.673	-1.195	-0.003
0.716	0.17	0.908	-1.698	0.023
0.819	0.20	1.194	-2.196	0.022
1.023	0.25	1.887	-3.548	0.042
1.229	0.30	2.981	-5.429	0.060
1.434	0.35	4.523	-8.024	0.052
1.628	0.40	7.725	-11.035	-0.132
1.843	0.45	14.509	-13.244	-0.991
2.047	0.50	22.302	-12.882	-2.113
2.253	0.55	28.026	-10.825	-2.846
2.457	0.60	33.496	-7.954	-3.499
2.662	0.65	37.427	-4.876	-3.875
2.867	0.70	40.730	-1.952	-4.077

II.4 Sysser 50 upright measurement data

V [m/s]	Fn	Rt [N]	z [mm]	θ [deg]
0.441	0.10	0.460	-0.465	-0.009
0.664	0.15	1.011	-1.495	-0.019
0.886	0.20	1.798	-2.676	-0.032
1.109	0.25	2.966	-4.492	-0.046
1.330	0.30	4.696	-6.697	-0.086
1.550	0.35	7.454	-10.187	-0.189
1.770	0.40	13.062	-14.782	-0.470
1.990	0.45	23.843	-19.584	-1.196
2.220	0.50	37.323	-21.874	-2.112
2.439	0.55	47.277	-20.958	-2.670
2.659	0.60	56.902	-18.968	-3.118
2.880	0.65	63.140	-16.209	-3.344
3.099	0.70	67.686	-13.202	-3.481

II.5 Sysser 47 heeled measurement data

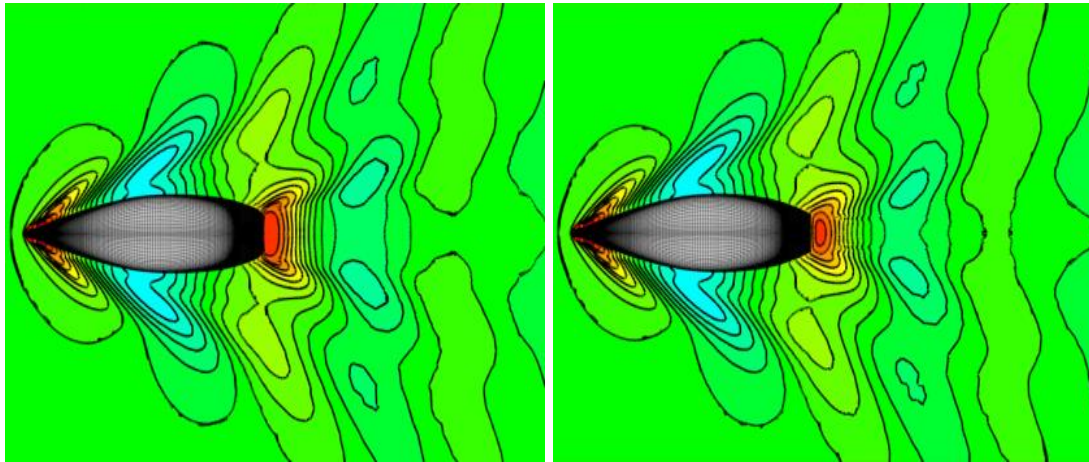
V [m/s]	Fn	Rt [N]	z [mm]	θ [deg]
0.409	0.10	0.275	-5.005	0.818
0.614	0.15	0.631	-5.520	0.843
0.819	0.20	1.091	-6.620	0.867
1.023	0.25	1.786	-8.395	0.923
1.229	0.30	2.890	-10.195	0.937
1.434	0.35	4.272	-13.120	0.984
1.628	0.40	7.298	-16.220	0.787
1.843	0.45	13.838	-18.035	-0.172
2.047	0.50	21.542	-18.585	-1.098

II.6 Sysser 48 heeled measurement data

V [m/s]	Fn	Rt [N]	z [mm]	θ [deg]
0.409	0.10	0.276	-3.660	0.791
0.614	0.15	0.625	-4.585	0.837
0.819	0.20	1.148	-5.790	0.888
1.023	0.25	1.899	-7.320	0.950
1.229	0.30	3.127	-9.490	1.054
1.434	0.35	4.989	-12.490	1.182
1.638	0.40	9.382	-16.420	1.025
1.843	0.45	17.098	-20.310	0.243
2.047	0.50	25.370	-21.895	-0.916

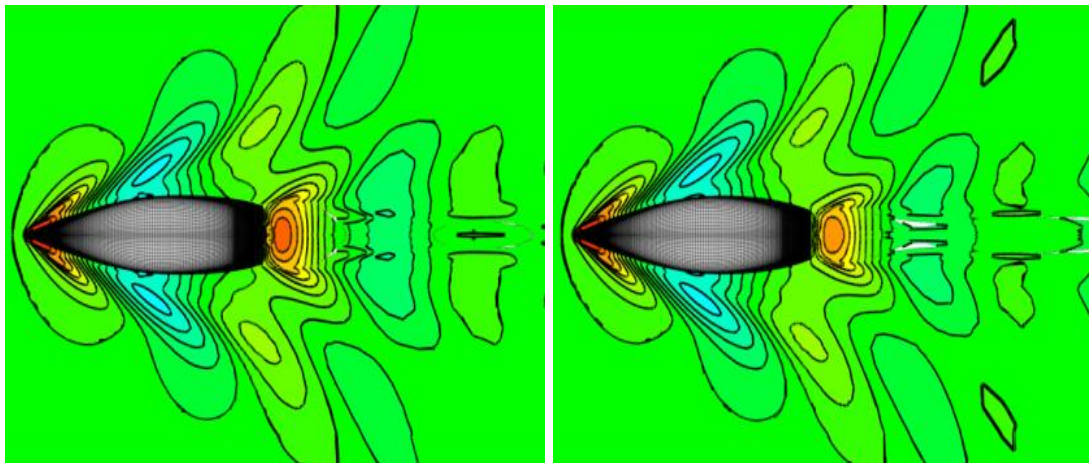
Appendix III - Optimization

III.1 Upright, $F_n = 0.35$



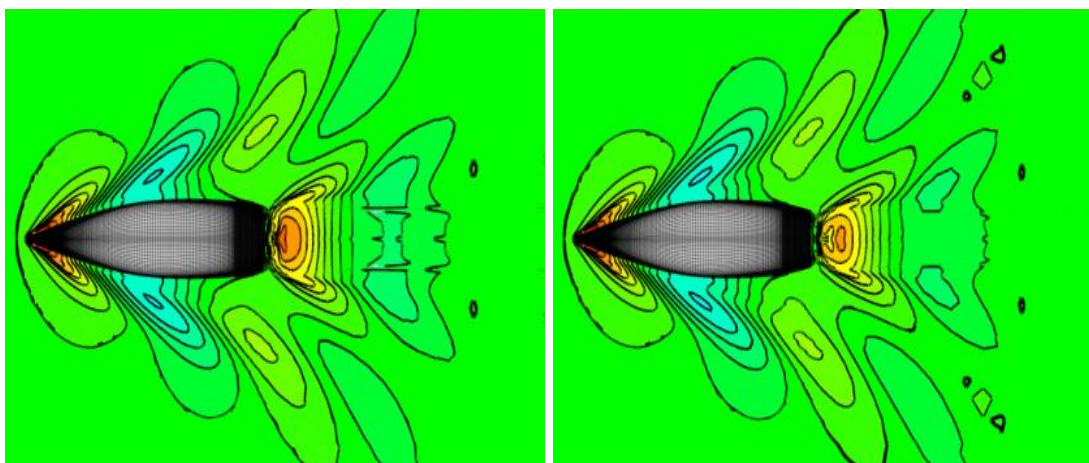
ND41-00b

ND41-00r



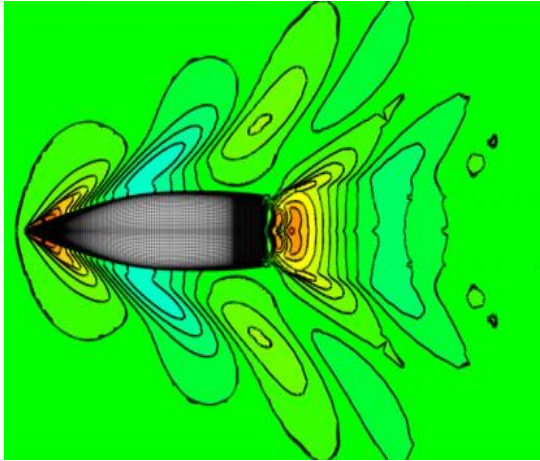
ND41-20b

ND41-20r

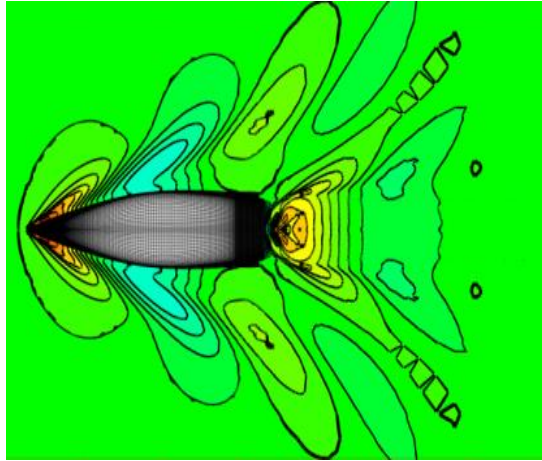


ND41-40b

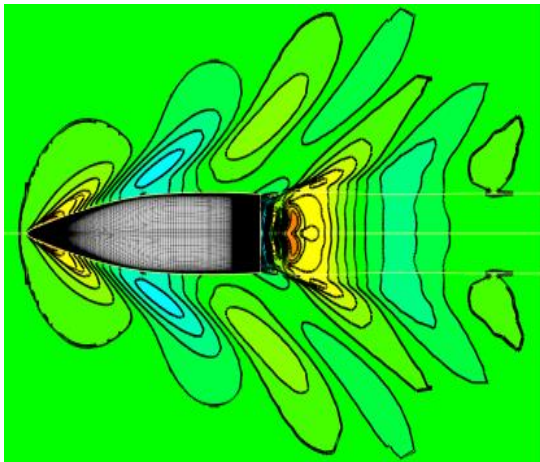
ND41-40r



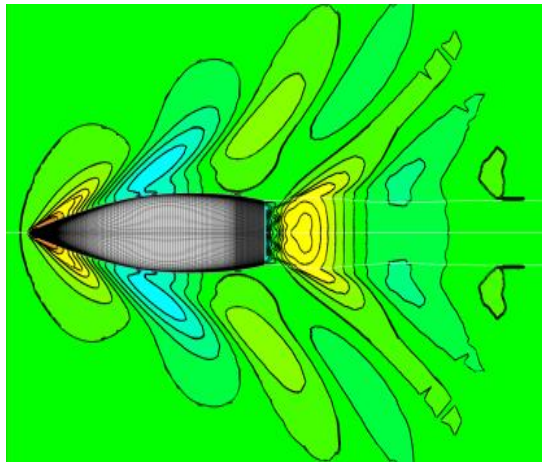
ND41-60b



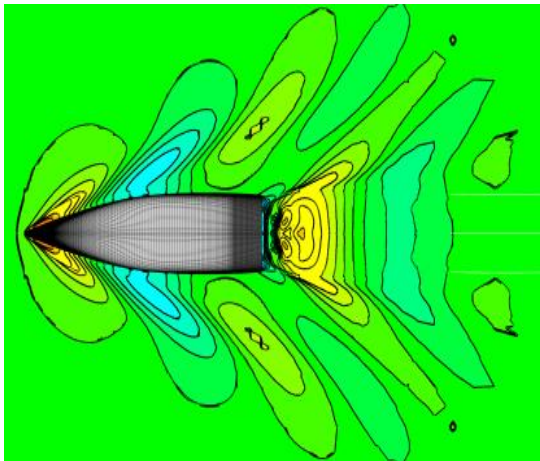
ND41-60r



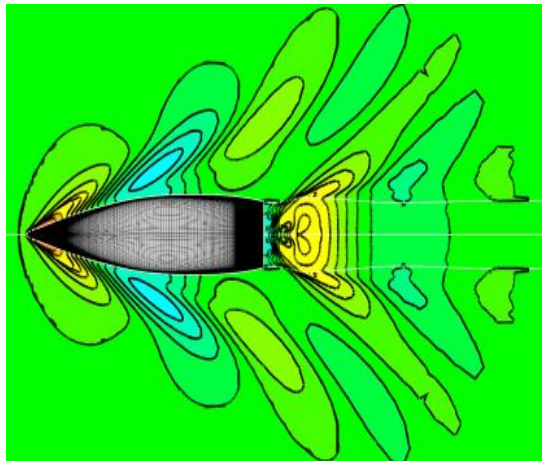
ND41-80b



ND41-80r

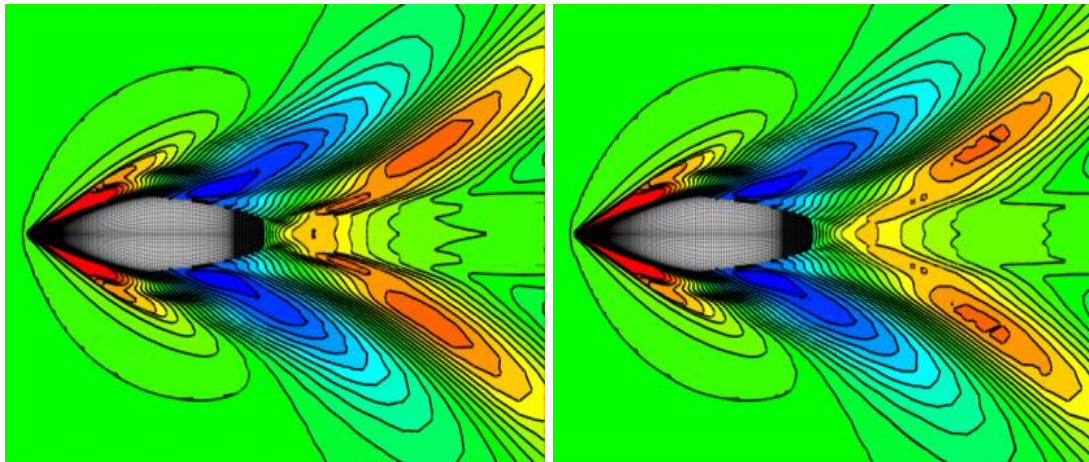


Nd41-100b



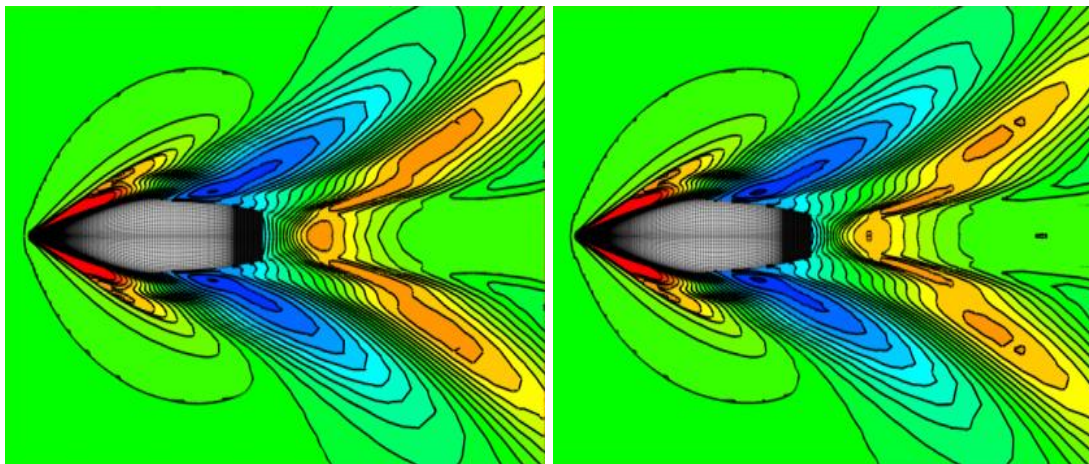
ND41-100r

III.2 Upright, $F_n = 0.60$



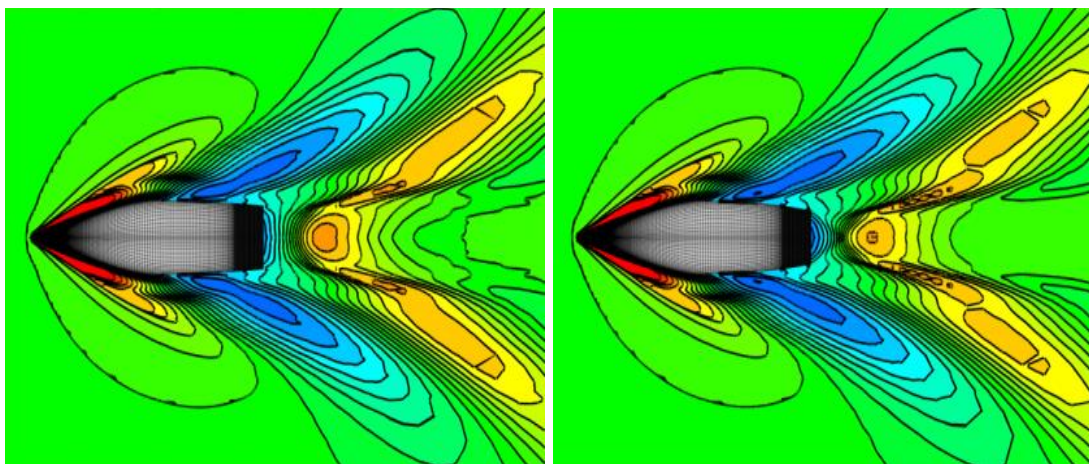
Nd41-00b

ND41-00r



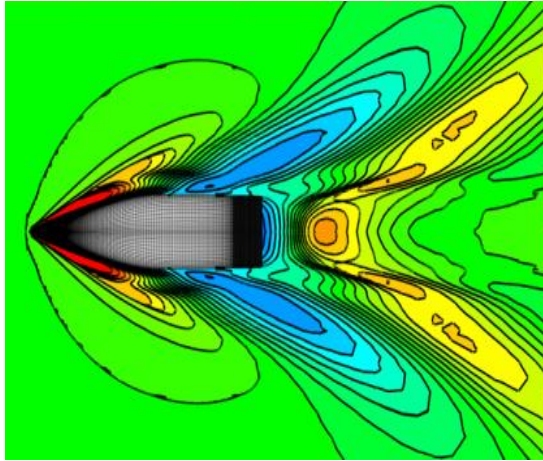
Nd41-20b

ND41-20r

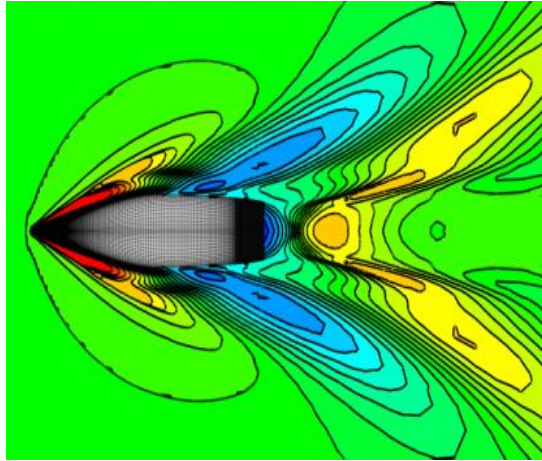


ND41-40b

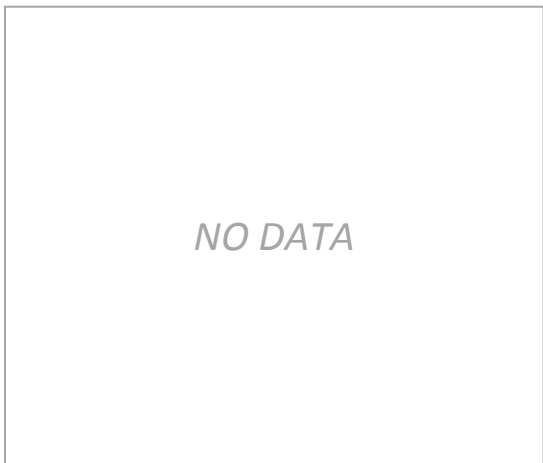
ND41-40r



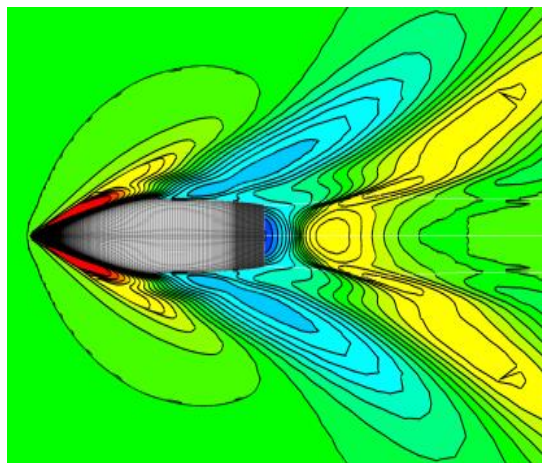
ND41-60b



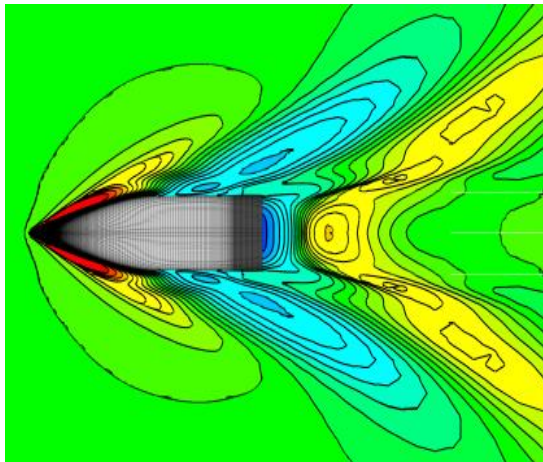
Nd41-60r



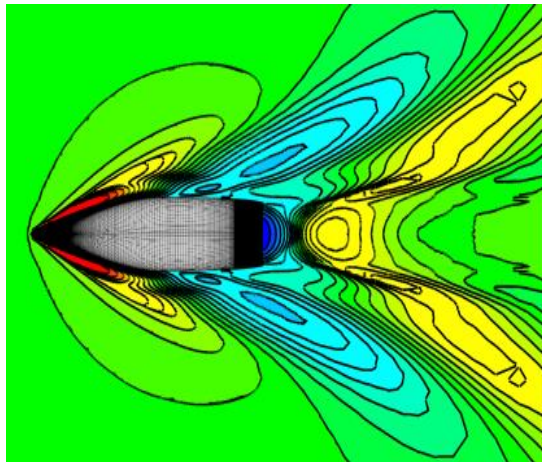
ND41-80b



Nd41-80r



ND41-100b



ND41-100r

Appendix IV – SHIPFLOW configuration files

IV.1 XPAN

IV.1.1 Upright

```
xflo
  titl(titl="ND41b_80_035")
  prog(xpan,xboun)
  vshi(fn=[0.35],rn=[2.66347e+006])
  hull(mono,h1gr="main",fsfl,tran,coar,bdens=0.5, fdens=0.5)
  offs(file="off_ND41_80b.shf",lpp=1.868,xaxd=-1,ysig=-1,zori=0.0589)
  control(exepath="C:\FLOWTECH\SHIPFLOW4.7.06-
x86_64\bin\..\bin/",runid="ND41b_80_035_RUN_DIR")
  ipos(trim=0)
end

xmes
  free(grno=2, df1=0.045)
end

xpan
  exforce(cvbody=0.00383)
  exmomen(towz=1.171)
  iter(maxi=60)
  para(nthr=4)
end
```

IV.1.2 Heeled

```
xflo
  titl(titl="h00b_035_xpan")
  prog(xpan)
  hull(mono,fsfl,coar,tran)
  offs(file="../off_h40b.shf",xaxd=-1,ysig=-1,lpp=1.868,xori=1.892,zori=0.092)
  vshi(fn=[0.35],rn=[2.66347e+006])
  symm(nosy)
  osfl(numb=1,flow=[6.39])
  control(exepath="C:\FLOWTECH\SHIPFLOW5.0.b3-
x86_64\bin\..\bin/",runid="C:\Users\Jens Allroth\Documents\_MsC\New
design\Heeled\_XPAN\h40b_035_xpan_RUN_DIR")
end

xmes
  body(grno=1,offs="lw",expa=0,stat=83,poin=14)
  body(grno=2,offs="ww",expa=0,stat=83,poin=21,ymir)
  free(grno=3,y2si=1.29998,xups= -0.634845,xdow=2.65454,nbd4=1,ibd4=[2],poin=21,str1=1,
    dl1=0.045,STRU=1,dfu=0,dlu=0.0454545,STRD=1,dfd=0.045454,dld=0,xd4=1.2,yd4=0.0
    4,stau=10,stam=23,stad=26)
  free(grno=4,nbd2=1,ibd2=[1],y4si=-1.29998,xups=-0.634845,xdow=2.65454,poin=21,
    str1=1,df1=0.045,STRU=1,dfu=0,dlu=0.0454545,STRD=1,dfd=0.045454,dld=0,xd1=1.2,yd1=0.04,
    stau=10,stam=23,stad=26)
```

```
end
```

```
xpan  
cont(free,nonl)  
iter(maxi=51)  
para(nthr=4)  
exmo(towz=1.1)  
exfo(cvbo=0.00383)  
end
```

IV.2 XCHAP

IV.2.1 Upright

```
xflow  
title( title = "ND41b_80_035" )  
program( xcha )  
vship( fn = [0.35], rn = [2.66347e+006] )  
hull( mono, vof, fsflow, coarse, wtran, h1gr = "main" )  
offset( file = "off_ND41_80b_035.shf", lpp = 1.868, ysign = -1, zori = 0.0657 )  
ipos(trim=-0.08)  
end
```

```
xgrid  
size( etamax = 104 , aetamax = 86 , uetamax = 42 , zetamax = 71 )  
xdistr( xsta = -1 , xfpu = -5.00000E-02 , xfpd = 2.25000E-01 ,  
        xapu = 8.80000E-01 , xapd = 9.90000E-01 , xend = 4.00000E+00 ,  
        NU = 32 , NF = 77 , NM = 92 , NA = 78 , NW = 53 ,habo = 0.025 , hund = -0.006 )  
yplus( ytar = 0.987 )  
singul( bow, xyzfwd = [ 1.759 , 0 , 0.0402 ] )  
end
```

```
xchap  
vof( lvcdist = 0.001 )  
control( start, maxit = 10000 )  
parall( nthread = 8 )  
end
```

IV.2.2 Heeled

Grid generation leeward

```
xflo  
titl(titl="ND41_h80b_035_lw")  
prog(xcha)  
vshi(fn=[0.35],rn=[2633907])  
hull(mono, vof, fsflow, coarse, wtran, h1gr = "main")  
offs(file = "off_ND41_h20_80b_lw.shf" , lpp = 1.868 , ysig = -1 , zori = 0.0923 )  
ipos(trim = -0.394)  
end
```

```
xgri
```

```

size(etam=96,aeta=71,ueta=42,zeta=55)
xdis(xsta=-1 , nu=25 , xfpu=-0.05 , nf=65 , xfpd=0.225 , nm=71 ,
      xapu=0.88 , na=59 , xapd=0.99 , nw=40 , xend=4 , hund=-0.0063 , habo=0.024)
yplu(ytar=1.280)
sing(bow,xyzf=[1.668, 0, 0.0690])
cont(twis=6.39)
end

```

```

xcha
  cont(start,maxit=000)
  para(nthr=8)
  vof(lvcdist=0.001)
end

```

Grid generation windward

```

xflo
  titl(titl="ND41_80b_035_ww")
  prog(xcha)
  vshi(fn=[0.35],rn=[2633907])
  hull(mono, vof, fsflow, coarse, wtran, h1gr = "main")
  offs(file = "off_ND41_h20_80b_ww.shf" , lpp = 1.868 , ysig = -1 , zori = 0.0923 )
  ipos(trim = -0.394)
end

```

```

xgri
  size( etamax = 128 , aetamax = 101 , uetamax = 42 , zetamax = 55 )
  xdistr( xsta = -1 , NU = 25 , xfpu = -5.0E-02 , NF = 65 , xfpd = 2.25E-01 , NM = 71 ,
  xapu = 8.80E-01 , NA = 59 , xapd = 9.9E-01 , NW = 40 , xend = 4 , hund = -0.0085 , habo =
  0.032)
  yplus( ytar = 1.280 )
  sing(bow,xyzf=[1.668, 0, 0.0690])
  cont(twis=-6.39)
end

```

```

xcha
  cont(start,maxit=000)
  para(nthr=8)
  vof(lvcdist=0.001)
end

```

Assembled grid for XCHAP calculations

```

xflow
  titl ( titl="20 degree heeled case at Fn = 0.35, both sides assembled" )
  prog ( xcha )
  hull( vof, mono )
  vshi(fn=[0.35],rn=[2633907])
  symmetry( nosym )
end

```

```

xchap
control(import,verb=2, start, maxit=10000)
para(nthr = 8 )
over(noiwe)
vof( lvcdist = 0.001)

import(xchap, grid="Xgrid_1", id="X1",
file="h80b_035_lw.cgns",
    ysign=-1,
        rotate=[0,0,-6.39],
        rotcent=[1.5,0,0],
        bc11="SLIP->INTERIOR",
        bc21="INTERIOR")

import(xchap, grid="Xgrid_transom_1", id="X2",
file="h80b_035_lw.cgns",
    ysign=-1,
        rotate=[0,0,-6.39],
        rotcent=[1.5,0,0],
        bc21="INTERIOR")

import(xchap, grid="Xgrid_1", id="X3",
file="h80b_035_ww.cgns",
    ysign=1,
        rotate=[0,0,6.39],
        rotcent=[1.5,0,0],
        bc11="SLIP->INTERIOR",
        bc21="INTERIOR")

import(xchap, grid="Xgrid_transom_1", id="X4",
file="h80b_035_ww.cgns",
    ysign=1,
        rotate=[0,0,6.39],
        rotcent=[1.5,0,0],
        bc21="INTERIOR")

end

```